1-1-2019

Optimizing the performance of complex engineering systems aided by artificial neural networks

Khalil Qatu

OPTIMIZING THE PERFORMANCE OF COMPLEX ENGINEERING SYSTEMS AIDED BY ARTIFICIAL NEURAL NETWORKS

A Dissertation
presented in partial fulfillment of requirements
for the degree of Doctor of Philosophy
in the Department of Civil Engineering
The University of Mississippi

by

KHALIL M. QATU

December 2019

ABSTRACT

Performance-based approach for material design, risk assessment, and emergency planning is utilized in this research. Artificial Neural Network (ANN) technique is employed to analyze and optimize two engineering problems; characterizing the stress-strain behavior of graphene nanocomposites and predicting earthen embankment failure due to overtopping. In the first application, the optimization is based on experimental data, and in the second application, it is based on numerical data.

In the first problem, Polyetherimide graphene nanoplatelets papers (PEIGNP) were tested with different graphene loadings varying from 0-97 weight percent (WT%). The resulting stress-strain curves were utilized to develop two ANN models. Stress-controlled and strain-controlled models. Both models showed an excellent correlation to the experimental. Several Mechanical properties were calculated from the predicted stress-strain curves, namely; toughness, maximum strength, maximum strain, and maximum tangent modulus. Both models captured the same overall behavior of the PEIGNP composite. However, the strain-controlled model was found to predict lower stress than the stress-controlled model. Finally, a Graphical User Interface (GUI) was developed to aid in future use of the developed material.

In the second problem, a comprehensive investigation is performed to study the behavior of earthen embankments during an overtopping event. Due to experimental limitations, numerical simulations are performed utilizing multi-phase Smoothed Particle Hydrodynamics (SPH) to study the post-failure behavior of the simulated embankments. This technique is validated by modeling different experiments focusing on various aspects of soil behavior, such as; failure mechanism, and seepage flow. Two hundred forty simulations are performed for different soil properties and embankment geometries. Embankment geometry consists of the side slope and

height. The embankment slope range considered between 1.2:1 – 3:1 (H:V). And the height range is between 3-15 m. While the soil is divided into two sections; embankment and foundation soil. Four different soil types were considered for the embankment soil and five for the foundation soil. Many failure parameters were studied, including; failure mode, peak discharge, Breach percent and initiation time, and foundation erosion. Eight ANN models were developed to predict these failure parameters. The developed models showed an excellent correlation to the numerical simulations. Finally, an EXCEL based GUI was designed to simplify the use of the developed models.

DEDICATION

This dissertation is dedicated to my family and friends who helped me and guided me through my times of stress and anxiety. In particular, my mother Asma' Qatu (Om Omar) and my lovely wife Rasha, who supported me during my study. To my brothers and sister: Omar, Khattab, and Ruba. This work would not have been possible without their support.

LIST OF ABBREVIATIONS

ANN - Artificial Neural Network

PEIGNP - Polyetherimide graphene nanoplatelets papers

WT% - Weight Percent

GUI - Graphical User Interface

SPH - Smoothed Particle Hydrodynamics

GNPs – Graphene Nanoplatelets

SEM - Scanning Electron Microscope

PEI - Polyetherimide

DMAc - Dimethylacetamide

ASDSO - Association of State Dam Safety Officials

EAP - Emergency Action Plan

FEM - Finite Element Methods

FVM - Finite Volume Methods

ASE - Averaged Squared Error

DMA - Dynamic Mechanical Analyzer

WCSPH - Weakly Compressible SPHEOS - Equation of State

GEF - General Embankment Failure index

EIF - Embankment Instability Failure index

EEF - Embankment Erosion Failure index

GFF - General Foundation Failure index

FEF - Foundation Erosion Failure index

FPF - Foundation Piping Failure index

FBF - Foundation Bearing capacity slide Failure index

BP - Breach Percent

BIT - Breach Initiation Time

PD - Peak Discharge

FE - Foundation Erosion

ACKNOWLEDGMENTS

I want to express my most profound appreciation to my advisors Dr. Ahmed Al-Ostaz and Dr. Yacoub Najjar. And my committee members, Drs. Hunain Alkhateb, Hakan Yasarer, and Andrew O'Reilly for their guidance and support.

I also acknowledge the collegial support from my fellow doctoral students. Hatem Almasaeid, Hashem Almashaqbeh, Rami Al-sughayar, and Obaydah Sras.

Lastly, I would like to express my genuine gratitude to Dr. Maziar Gholami Korzani for providing his software “PersianSPH” and his help explaining the software as well.

TABLE OF CONTENTS

LIST OF TABLES

LIST OF FIGURES

1. INTRODUCTION

1.1 Optimization aided by Artificial Neural Networks

Performance-based approach for the design, construction, management, assessment, and maintenance of Civil Engineering materials and structures, must satisfy the fundamental requirements of strength, resilience, sustainability, and safety from risks, such as floods, earthquakes, fires, and explosions. This approach requires a comprehensive analysis of the performance indicators. Traditionally, such an analysis relies on classical mathematical techniques which are often limited by the assumptions of trend, distribution, and variable individuality, etc. In the past decades, soft computing techniques have been a low-cost alternative to perform complex analyses in engineering applications.

Artificial Neural Networks (ANN), which is considered a part of the soft computing techniques, is one the most commonly used methods for knowledge discovery. ANN is a computational method that emulates the human neurological network structure. On the contrary of conventional techniques, ANNs capture trends and variable relationships without being conformed to predetermined equations. Recently, ANNs has been a popular method to model various civil engineering problems, such as; structural design (Armaghani et al. 2019), material behavior modeling (Bui et al. 2018), geotechnical problems (Koopialipoor et al. 2019), transportation engineering (Baldo et al. 2018), and Environmental engineering (García-Alba et al. 2019).

(Armaghani et al. 2019) studied the optimization of retaining walls design. In their study, the safety factor against overturning was the objective parameter. While considering the wall height, concrete density, soil density, soil friction angle and the wall base width as input

parameters. The developed prediction model was used alongside the Ant Colony Optimization algorithm to achieve the optimum design for the given problem. The model can efficiently optimize the safety factor for given design parameters ranges.

(Bui et al. 2018) studied the performance of high-performance concrete. The objective parameter of their study was the compressive strength. The mix design parameters were; cement, blast-furnace slag, fly-ash, water, superplasticizer, coarse aggregate, and fine aggregate proportions as well as the age of testing. The authors utilized ANN to develop the prediction model combined with Modified Firefly optimization algorithm. The developed model can predict the compressive strength of high-performance concrete with high accuracy.

(Pham and Hadi 2014) used ANN modeling, with the Purlin function as an activation function, to calculate the compressive strength and strain of fiber reinforced polymer (FRP) confined square columns. The proposed model showed an excellent correlation to the experimental data, performing better than the mechanical models developed before.

(Gangi Setti and Rao 2014) proposed an ANN model to predict the stress-strain curve of titanium alloy as a function of the volume fractions of α and β. They used a combination of activation functions (tan-sigmoid, log-sigmoid, and Purlin) and training algorithms (cascade-forward backpropagation, feedforward backpropagation, and layer recurrent). The best performing network was a combination of the log sigmoidal activation function and the layer recurrent training algorithm.

(Najjar and Huang 2007) implemented the recurrent (dynamic) ANN to predict the stress-strain behavior of soils under various initial confining pressures, densities and compaction states. In their work, the proposed ANN model was used to overcome the complexity, practicality, and accuracy of the available mechanical constitutive models. The final ANN model showed excellent statistical accuracy measures when compared to the experimental data.

In this dissertation, two optimization problems are addressed. **Graphene nanocomposite mechanical behavior** as well as **post-failure behavior of earthen embankments due to overtopping**.

1.2 Graphene Nanocomposites

Graphene has generated enormous research interest in the past decade due to its superior electrical, thermal, and mechanical properties (Chen et al. 2008). These properties offer potential advancements in many areas of research, one of which is manufacturing the graphene nanoplatelets into a macroscopic, paper-like, freestanding sheet form called graphene paper. This graphene paper has a variety of applications, such as lithium battery electrodes (Wang et al. 2009a), freestanding electrodes for flexible supercapacitors (Wang et al. 2009b), and electromagnetic interference shielding sheets (Jiajie et al. 2009). The mechanical, thermal, and electrical properties of graphene nanocomposites have been extensively investigated, and it is reported to be a next-generation multifunctional super-material (Lahiri et al. 2012).

Low price graphene nanoplatelets (GNPs) can be exfoliated from natural graphite, which is essentially a stack of graphene that has layers ~10 nm thick shown in Figure 1, and the size of the platelets can be controlled (Li et al. 2015). These GNPs exhibit properties analogous to those of the graphene sheets.

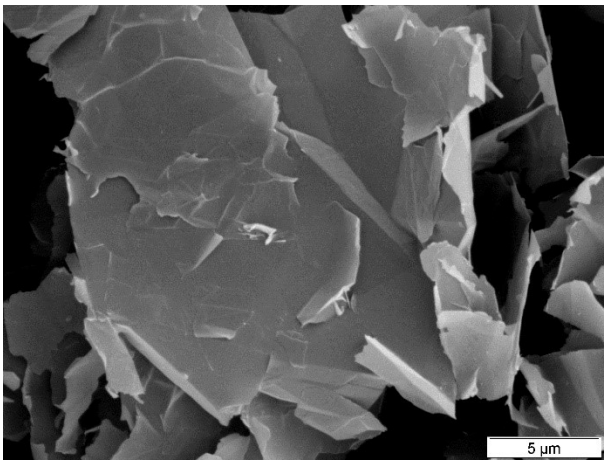

Figure 1: Scanning Electron Microscope (SEM) Image of Graphene Nanoplatelets (GNPs)

However, an issue arises when such highly graphitic platelets are assembled to form graphene papers. GNPs are crystalline and smooth, so the platelets slip past one another due to a lack of defect sites and oxygen groups which would create a strong adhesion between individual GNPs. An obvious solution is to use a binding material to attach individual GNPs to form the macroscopic papers. However, the binder material must be compatible with the graphene sheets that form the GNPs. Polyetherimide (PEI) can be used as a binder material for GNPs and was studied before by (Wu and Drzal 2012). However, Wu et al. used dichloromethane to dilute the PEI, which is very volatile and evaporates very fast to form a PEI skin. This results in difficulty controlling the GNP loading in the final paper. (Li et al. 2015) used dimethylacetamide (DMAc) to dilute the PEI, allowing the GNP papers to be easily fabricated with almost any GNP concentration (0 to nearly 100 wt.%). (Li et al. 2015) studied the behavior PEI-GNP papers he fabricated. A significant increase in the loss and storage moduli was found. Additionally, impedance, glass transition temperature, as well as the damping coefficient, were studied.

1.2.1 Need of Research

Graphene nanocomposites are being used in many applications, such as; aerospace, defense, additive manufacturing, coating, and many others. Each discipline focuses on specific properties of the material, namely; thermal, electrical, or mechanical. Additionally, it is essential to optimize the nanocomposite graphene loading for its intended application while keeping in mind other properties at the same time. While the PEIGNPs were studied by (Li et al. 2015) in terms of electrical, thermal, and mechanical behavior, the static behavior was only considered in terms of the stress and strain at failure. Which does not show the overall material behavior. Moreover, graphene nanocomposites exhibit behavioral variation due to their inhomogeneous structure. Subsequently, it is essential to develop a design tool that can guide engineers to get the optimum graphene content for the desired properties.

1.2.2 Objectives

- Test the developed PEIGNPs with varying graphene content ranging from 0-97% using standard tension test.
- Develop optimization models utilizing artificial neural networks (ANN) to predict the behavior of the PEIGNPs under different graphene loadings
- Study the accuracy of the developed models compared to the experimental results
- Perform a sensitivity analysis of the PEIGNPs to the graphene loading
- Calculate different mechanical properties from the stress-strain curves obtained from the experimental testing as well as the developed ANN models.
- Develop graphical user interface (GUI) utilizing the developed ANN models

1.3 Dam overtopping

Extreme weather events such as hurricanes occur every year. Heavy water runoff coincides with these events. Dams and levees are one of the most crucial protection infrastructures in these occasions. While these structures are designed to withstand a 50 or 100-year storm. Some of these structures fail due to deterioration of the dam soil condition or due to extreme loading the dam wasn't designed to withstand.

The Association of State Dam Safety Officials (ASDSO 2015) reports more than 90,000 dams in the United States. More than 15,000 are considered high-hazard potential dams, that is, failure is projected to result in loss of life or may cause substantial economic damage. Moreover, ASDSO statistics on dam failure incidents between 2010-2015 shows that more than 70% are caused either by an extreme weather event or overtopping.

It is essential to prepare for emergencies like dam failure, especially high-hazard potential dams. As of 2017, 81% of the state-regulated dams have an emergency action plan (EAP) (ASDSO 2015). It is also essential to predict dam failure before the incident itself to provide

time to execute these EAPs. Additionally, post-failure behavior is necessary to predict the extent of the damage caused by these extreme events.

1.3.1 Dam Failure

Many studies were carried to investigate dam failure parameters, such as; failure mode, breach shape, breach height and width, breach formation time, and peak discharge. These studies focus on the empirical formulation of these failure parameters.

(Froehlich 2008) studied 74 embankment failures and formulated a model to predict the final breach width, height, and the time to failure. In their study, a Monte Carlo simulation was used to evaluate the degree of uncertainty for the breach parameters. The authors' database didn't include the soil characteristics for the failed embankments.

(Alhasan et al. 2015) studied four small dam failures in the Czech Republic. In their study, a one-dimensional numerical model was developed to simulate the flow during an overtopping incident. The authors assumed a trapezoidal shape for the failed dam section. The software HEC-RAS was used to simulate the hydraulic flow and erosion of the assumed trapezoidal cross-section channel. The erosion parameters were calibrated using the field measurements observed from the studied dam failures. The peak discharge was calculated for each case and compared with the field measurements.

(Franca and Almeida 2004) developed a numerical model to simulate rockfill dam overtopping failure "RoDaB". The model relies on hydraulic flow simulation and empirical erosion parameters calibrated from laboratory experiments. The model was compared with other breach models that depend on similar parameters. Rockfill dam breach was found to be entirely different than that of earthen fill. The authors suggested a more comprehensive calibration of the erosion parameters.

(Gee 2009) conducted a comparison between different models that simulate the dam overtopping failure. These models rely on the assumption of the initial shape of the eroded

channel at the top of the dam crest and empirical soil erosion parameters. The developed models generated more significant flow estimations than the observed ones.

(Froehlich 2016) collected data from 111 dam failures and formulated empirical formulae to predict the final breach parameters; average width, channel side slope, and formation time. These formulae depend on dam geometry, failure mode, impounded water volume. Soil properties were not considered in this study. Moreover, breach formation time wasn't available for most of the studied datasets.

(Zhong et al. 2018) studied the stability of clay core dams during the overtopping incident. Dam erosion was calculated using empirical erosion parameters. The breach parameters studied in this paper were; the breach width, discharge, and formation time. The dam clay core stability was considered in addition to the erosion of the breach channel. Overturning failure of the clay core was found to be dominating.

1.3.2 Numerical Modeling

Since it is not feasible to perform full-scale lab experiments to build such a wide-ranging database, numerical simulations were utilized in this research. Large deformation and post-failure analyses are generally difficult to achieve in Finite Element Methods (FEM) or Finite Volume Methods (FVM). These methods are grid-based methods, which suffers from grid distortion or even computational instability due to the negative values of Jacobian determinants at nodes of integration (Bui et al. 2008a). This issue can be solved by relying on meshless methods such as; Smoothed Particle Hydrodynamics (SPH).

Smoothed Particle Hydrodynamics (SPH) is a meshless numerical method used to obtain the solution of fluid and continuum dynamics equations by replacing the fluid and/or continuum with particles. Originally, SPH was developed in 1977 for astrophysics applications (Gingold and Monaghan 1977). The Material is discretized into Particles that have material properties such as density, velocity, and stress. These particles move according to their defined governing

equations. Particle interaction is only calculated within a certain radius called smoothing distance (h). The weight of each particle contribution is calculated using a kernel function (W). The Choice of the smoothing distance and kernel function affects the stability, accuracy, and the efficiency of the numerical solution (Monaghan 1994).

In the last decade, SPH has been used for various geomechanical applications, such as; soil stability, soil structures failure, and hydraulically loaded soil embankments. (Bui et al. 2006) used SPH to simulate Soil failure flows using the elastic-perfectly plastic soil constitutive model. In their study, the Drucker-Prager model was used to describe soil plastic behavior (i.e., Failure criteria). SPH results showed good agreement with the experimental results as well as FEM ones.

(Bui and Fukagawa 2013) developed an improved SPH formulation to account for soil-water interaction. In their study, a hydrostatic pore water pressure is assumed. The authors performed multiple validation problems, namely; a case of fully/partially submerged soil sample, as well as slope stability problem. The results of the simulations were consistent with the theoretical solutions of the given problems.

(Korzani et al. 2018a) studied homogeneous embankments under hydraulic and mechanical loading. The saturated soil was modeled as two layers; soil and water layer. Each layer has its governing equations of motion. The interaction between these two layers was implemented in terms of the pore water pressure and seepage forces. Their approach was validated compared with different experiments (porous flow and slope stability).

1.3.3 Need of research

A comprehensive database is necessary to understand the post-failure behavior of the earthen dams. Several studies attempted to develop empirical formulae to predict different parameters of dam failure, such as; failure mode, breach shape, breach height and width, breach formation time, and peak discharge (Froehlich 2016). However, these studies only focus on the hydraulic

failure mechanism. That is by defining an initial shape and size of failure, then study the erosion progress of the channel bed. Dam failure due overtopping of water could also cause a structural failure which hasn't been investigated so far. After examination of the databases acquired from literature, only the geometric properties of dams were recorded. Soil properties such as the angle of friction, cohesion, and grain size distribution are missing. Hence the focus of this study on the overall dam stability as well as surface erosion progression and its effect on dam stability.

1.3.4 Objectives

- Validate the SPH code developed by Dr. Korzani "PersianSPH" (Korzani 2015).
- Identify the numerical simulation input parameters and develop a simulation database to be utilized in developing the ANN models
- Identify the failure parameters such as; failure mode, peak discharge, breach percent, and initiation time.
- Develop ANN models to correlate the models' input parameters to the desired failure parameters.
- Validate the developed ANN models by performing numerical simulations that were never included in the ANN optimization process.
- Develop a graphical user interface (GUI) to predict the behavior of earthen embankments due to overtopping.

1.4 Dissertation structure

The core of this dissertation is comprised of three main chapters*; Optimization aided by Artificial Neural Networks*, followed by two optimization applications; *characterizing the static behavior of graphene nanocomposites* and *Predicting embankment failure during overtopping event*. In the first application, the optimization is based on experimental data, and

in the second application, it is based on numerical simulation data. Each problem is discussed in a separate chapter. The structure of this dissertation is depicted in Figure 2.

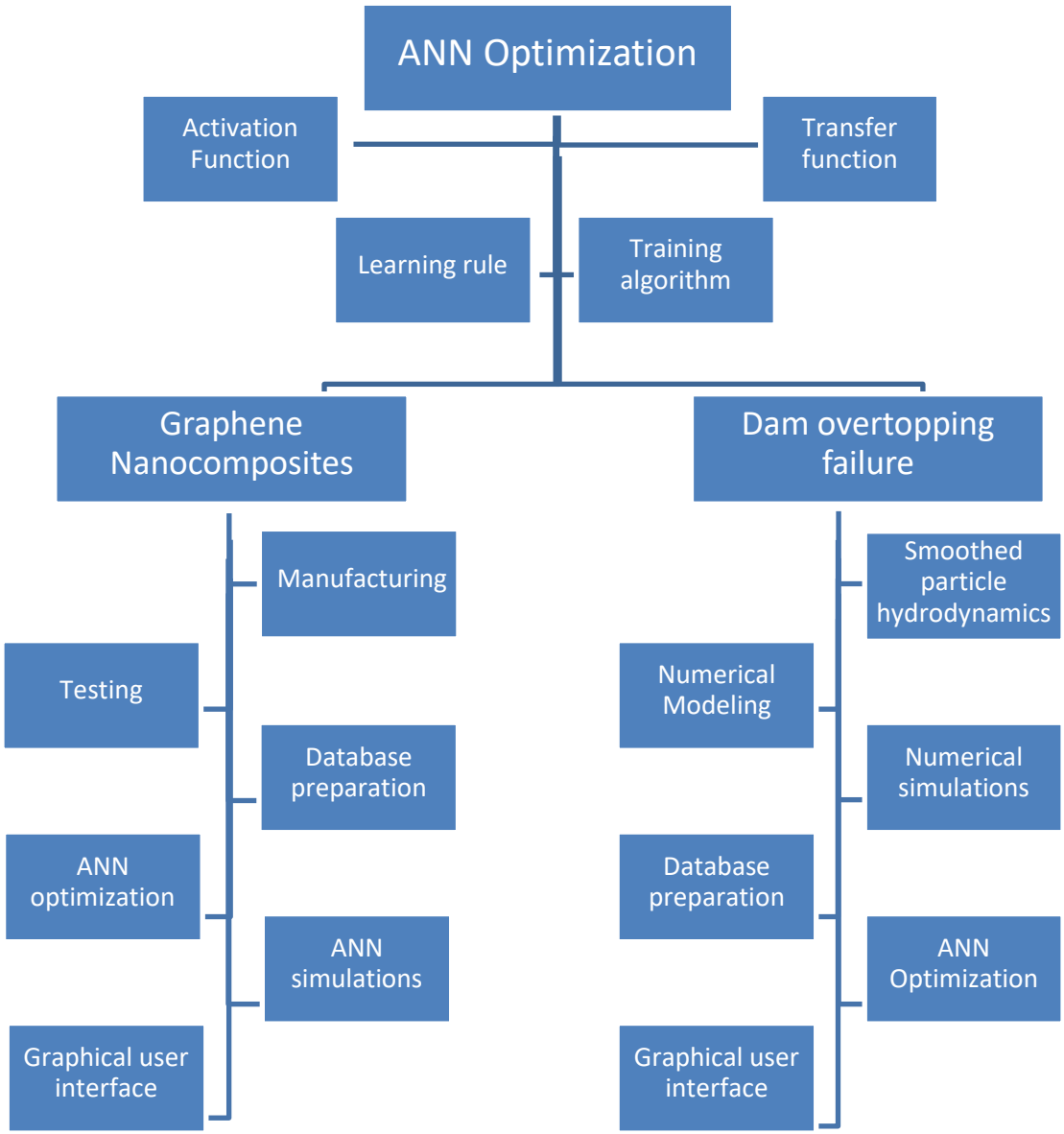

Figure 2: Dissertation structure

2. OPTIMIZATION AIDED BY ARTIFICIAL NEURAL NETWORKS

Neural networks have been attracting increasing attention since the development of the concept of artificial neurons (McCulloch and Pitts 1943). Ever since new and more advanced models have been proposed from decade to decade. Artificial Neural Networks (ANNs) emulates the structure of the human brain. As the ANN model is not conformed to a specific formula, the model is kept free of the assumption of the behavior of the data, unlike the conventional regression techniques.

An ANN model is comprised of different layers; input, hidden, and output layers shown in Figure 3. Each layer consists of *"computational nodes"* (i.e., neurons). An ***"Activation function"*** is assigned at each node to perform the calculation. Neurons are connected among different layers with links. Each link has different *"connection weight"* that is optimized in the training stage.

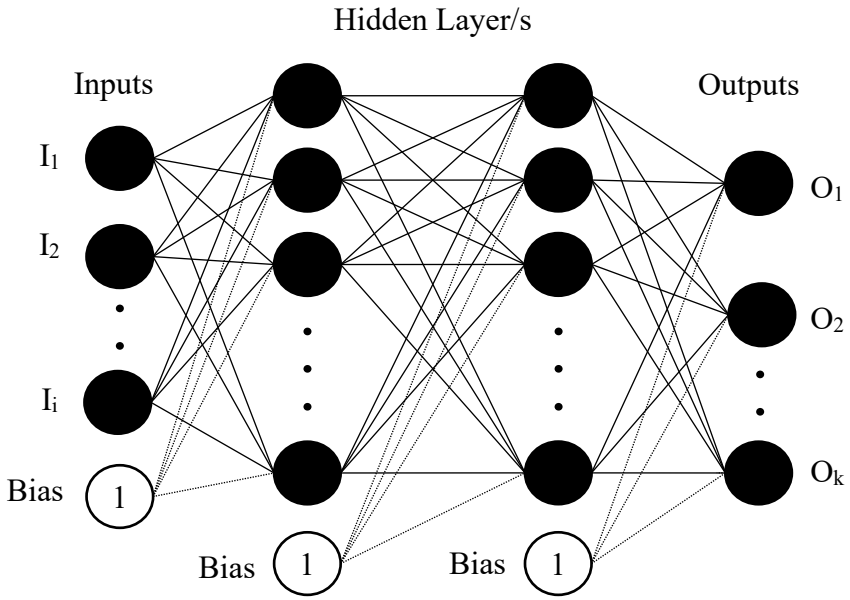

Figure 3: Typical ANN model structure

The input and hidden layers have a “bias neuron” (Rojas 1996). These neurons are added to each layer to prevent the network from being “biased” to a specific neuron during the calculation process. The bias term is also referred to in the literature as neuron threshold. The value of bias neurons is kept constant at 1. However, its connection weight to the other neurons in the next layer is optimized during the training stage.

The information is carried over from any layer to the next using a ***“Transfer function”*** utilizing the connection weights. Then, the ***“Learning rule”*** is defined, which specifies how the connection weights are optimized (i.e., learning). Finally, the ***“Training Algorithm”*** need to be assigned to reach the final network structure.

In this section, the node activation function, transfer function, learning rule, as well as the training algorithm is discussed extensively.

2.1 Activation function

The calculation at each node is applied using the activation function. There are different types of activation functions. The step or threshold function, as the name suggests, only has two values 0, 1. If the value of the neuron input exceeds a certain value, the function returns 1, otherwise, it returns 0. This function is generally used in clustering or classification problems. The linear function, where the weighted sum input of the neuron is added to a linearly dependent bias. This function can be used in engineering problems (Pham and Hadi, 2014). Another function usually used in engineering problems is called Log-Sigmoid function, also known as the Logistic function. This function is represented by equation (1). The slope factor β determines the slope of the function. Figure 4, shown below depicts the Log-Sigmoid activation function at different slope factors.

$$f(x) = \frac{1}{1 + e^{\beta x}} \tag{1}$$

Where β: slope factor

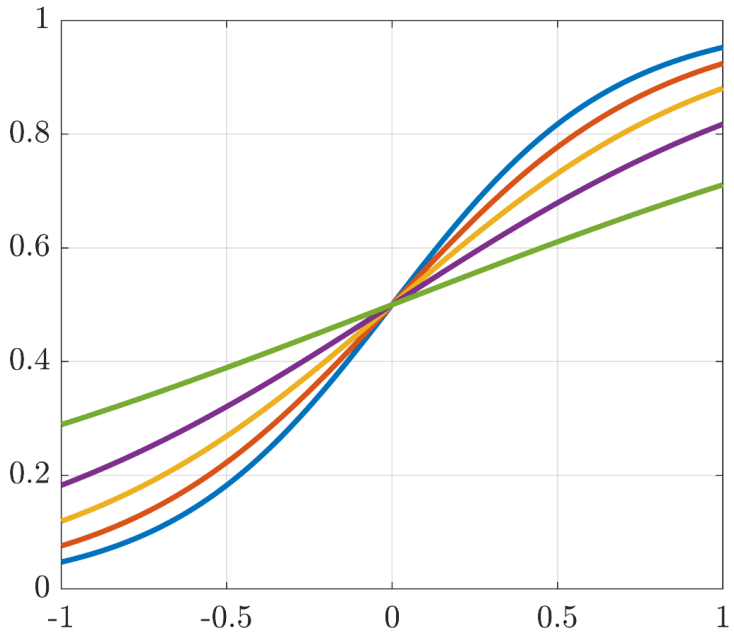

Figure 4: Sigmoid activation function

Another variation of the Log-Sigmoidal function is the Tan-sigmoid function. Where a hyperbolic tangent function is used instead of equation (1).

In this dissertation, the Log-Sigmoid function, referred to as the Sigmoid function, is utilized due to the simplicity to calculate its derivatives. Which will be helpful during the training stage.

2.2 Transfer function

Neurons transmit data from each layer to the next (i.e., Feed-Forward). Each Neuron receives the data (i.e., signal) from all the neurons in the previous layer as a weighted sum represented by equation (2). The signal S_k becomes the input of the activation function.

$$S_k^L = \sum_j w_{jk} f_j^{L-1} + \theta_k \tag{2}$$

Where: S_k: The total input of neuron k in the layer L

w_{jk}: The connection weight between neuron k in layer L and neuron j in layer L-1

f_j^{L-1}: The output from neuron j in layer L-1

θ_k: The connection weight between the bias neuron in layer L-1 to neuron k

2.3 Learning rule

After the data has been transferred through the network. The result from the output neuron (i.e., the predicted value) is compared with the target value. The error between these two values is used to tweak the connection weights. There are different methods of propagating this error (i.e., Error Back-Propagation) to adjust the connection weights, such as; Perceptron's, Gradient Descent, Levenberg-Marquardt, and many others. The most popular learning method is the Gradient Decent method due to its simplicity, stability, and effectiveness.

The Gradient Decent method propagates the error from the output layer to the previous layers utilizing the derivatives of the activation function. The weight adjustments are calculated using equation (3).

$$\Delta w_{jk}^{L} = \eta \delta_j^L f_k^{L-1} \tag{3}$$

Where: η: Learning rate that specifies the step size between iterations

δ_j^L: Correction factor in layer L, calculated using equations (4) and (6).

f_k^{L-1}: The output of neuron k in layer L-1

The error factor for the connection weights between the neurons in the output layer and the hidden layer is calculated using equation (4). The error signal is then propagated to the hidden layer utilizing the connection weights between these two layers using equation (5). The error factor for the neurons in the hidden layer is then calculated using equation (6). The first derivative of the Sigmoid activation function is represented by equation (7). After calculating the error factors for all neurons in the output and hidden layers, the weight adjustments are computed for each connection weight within the network.

$$\delta_j^O = \left(T_j^O - f_j^O\right) f'\left(f_j^O\right) \tag{4}$$

$$ES_k^H = \sum_j w_{jk}\, \delta_j \tag{5}$$

$$\delta_k^H = ES_k^H \, f'(f_i^I) \tag{6}$$

$$f' = f\,(1 - f) \tag{7}$$

Where: δ_j^O: The correction factor for neuron j in the output layer

T_j: The target value of neuron j in the output layer

f_j^O: The output of neuron j in the output layer

f': The first derivative of the activation function.

ES_k^H: Error Signal transmitted from the output layer to neuron k in the hidden layer

δ_k^H: Error factor for neuron k in the hidden layer

f_i^I: The output of neuron i in the input layer

2.4 Training Algorithm

The Feed-Forward – Error-Backpropagation method is utilized for updating the connection weights. This method is comprised of 5 steps, as follows:

Step 1: Initialize connection weights.

Step 2: Pass inputs through the network utilizing the transfer function, equation (2).

Step 3: Calculate the error factors for all neurons in each layer, equations (4) & (6).

Step 4: Update the connection weights using the weight adjustments, equation (3).

Step 5: Repeat Steps 2-4 for all datasets (Iteration).

The training algorithm in this research is chosen using the procedure outlined in (Najjar and Huang 2007). Accordingly, the network is trained using the Feed-Forward – Error-Backpropagation method, described earlier, starting from 1 hidden node and for 20,000 iterations on the specified structure. Then, hidden nodes are added one by one until it reaches the maximum number of hidden nodes calculated using equation (8).

$$\text{HN} = \frac{\text{N-NO}}{\text{C} \cdot (\text{IN+NO+1})} \tag{8}$$

Where: N: The number of training data sets.

NO: The number of outputs.

IN: The number of inputs

C: The number of data points allocated to each connection weight (constant).

The network with the lowest Averaged Squared Error (ASE), equation (9), is chosen as the best prediction network for this scenario. Then, the same process is performed for structure starting with two hidden nodes, and so on, until the maximum number of hidden nodes is reached. The best of the best prediction network structures is chosen as the optimal ANN prediction model.

$$\text{ASE} = \frac{1}{N} \sum_N (T_i - O_i) \tag{9}$$

Where: N: The number of training datasets.

T_i: The Target value of dataset i

O_i: The model output corresponding to T_i

To prevent the ANN models from being biased towards a specific input, the values of all the inputs are normalized using equation (10).

$$X_n = \frac{X - X_{max}}{X_{max} - X_{min}} \tag{10}$$

Where: X_n: The normalized value.

X: The actual value

X_{max}: The maximum value of X

X_{min}: The minimum value of X

3. GRAPHENE NANOCOMPOSITES

Graphene has attracted colossal research interest in the past decade. That is due to its excellent electrical, thermal, and mechanical properties (Chen et al. 2008). These properties present possible improvements in many areas of research, one of which is manufacturing the graphene nanoplatelets into a macroscopic, paper-like, freestanding sheet form called graphene paper. The material developed by (Li et al. 2015), shown in Figure 5, is manufactured and tested a standard stress controlled tension unit. Seventy-one tests were conducted for several graphene loadings ranging from 0~97 wt.%.

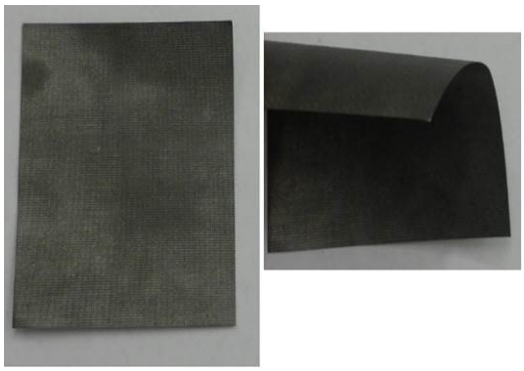

Figure 5: Typical sample of the PEIGNP Nanocomposite paper

In this section, the manufacturing and testing processes are discussed in detail. Then the preparation of the database for ANN modeling is explained. After that, the developed models are described. Additionally, ANN simulations are performed utilizing the developed models as well as sensitivity analysis and mechanical properties. Finally, a graphical user interface (GUI) is designed as a helpful tool to predict the behavior of the material for any given WT%.Material manufacturing

In this research, PEI and dimethylacetamide (DMAc) were purchased from Sigma-Aldrich and Fisher Scientific, respectively. GNPs with an average diameter of 50 μm were used to

manufacture the PEIGNP composites. The graphene-based nanocomposite analyzed in this paper was PEIGNP that was manufactured using the filtration-hot press method reported by (Li et al. 2015), namely, GNPs were dispersed in DMAc in a one-neck flask by magnetically stirring and sonication. The right amount of PEI was added into the mixture. While being stirred and quenched with a condenser, the mixture of GNPs, PEI, and DMAc was refluxed for half an hour. After cooling the suspension to room temperature, it was vacuum filtered (vacuum pressure: -66 cm mercury) through a porous Teflon fabric to obtain a PEIGNP cake, which was then dried in an oven at 190°C for 1 hour to allow the DMAc to evaporate. The dried PEIGNP cake was placed between two PI films coated with the release agent and then clamped with two aluminum panels for hot-pressing. The operating parameters during hot-pressing were: a pressure of 10 nominal MPa based on the applied tonnage and the area of the sample, 4 minutes and 340°C. The pressed paper was then lightly pressed (about 3 MPa, 1 min and 340°C) a second time to smooth the final PEIGNP paper. Either neat PEI film or pure GNP paper was hot-pressed in the same way as that for PEIGNP paper.

3.1 Testing

Dynamic Mechanical Analyzer, DMA Q800 (TA Instruments Inc., New Castle DE, USA), Figure 6, was used to perform the tensile tests is used utilizing a standard stress-controlled tension module. The temperature is held constant throughout all tests at 35°C. The force was ramped at a rate of 0.5 N/min up to failure.

Figure 6: DMA Q800 by TA Instruments

Figure 7 shows samples of the resulting stress-strain curves for different GNP loadings. The test results exhibited a variation ranging between 1-40% was found in the maximum stress for the samples with the same WT.% of added graphene. This variation was the motivation for using ANN to model the behavior of the material with different wt. %. All tested samples curves are shown in APPENDIX A.

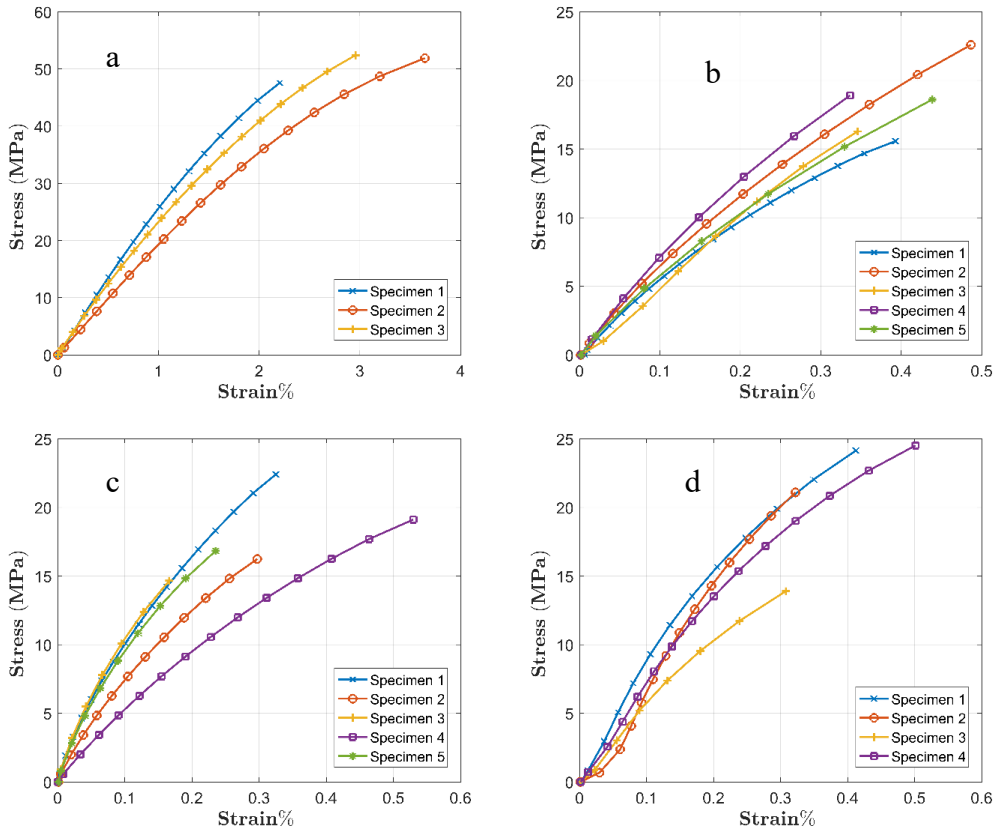

Figure 7: Sample experimental stress-strain responses for a) 0.5 wt. % b) 25 wt.% c) 40 wt.% and d) 85 wt.%

3.2 Database preparation

A total of 71 tests were performed with varying graphene content. Each stress-strain curve contained its corresponding wt. %, stress, and strain data values. Since there was a difference in the number of data points available for each experimental response (curve). To prevent the ANN model from being biased towards a specific curve more than another, therefore, all stress-strain responses (curves) were interpolated based on their respective ranges to provide 600 data

points. A total of 42,600 datasets are provided for training the ANN model. The tests were divided into three categories; training, testing, and validation. Thirty-six experiments were included in the training, 21 tests in the testing, and 14 tests in the validation.

Additionally, the stress and strain at failure were recorded for each test and prepared as a separate database. This database containing the WT%, Maximum stress, and Maximum strain will be utilized to develop another ANN model that works as a stopping criterion for each ANN stress-strain simulation.

A maximum of 12 hidden nodes was set to prevent the ANN model from memorizing the data. Which inhibit the model ability to predict the behavior of samples that were not given in the training stage. Finally,to find a better solution for the optimum network structure, the ANN model is trained on all the data (training, testing, validation) utilizing the same structure of the train-test model (Najjar and Huang 2007).

3.3 ANN Optimization

Three different ANN models were developed; stress-controlled, strain-controlled, and stopping criterion models. The first two models are utilized to predict the stress-strain behavior for a given graphene loading. The third model, which predicts the maximum strain for a given WT% of graphene loading, is utilized to stop the simulation for the first two models.

3.3.1 Stress-controlled model

In this model, the strain is predicted as a function of stress and the weight percent of added GNP. After performing the training process discussed in section 2.4, the best performing model was obtained by adaptively starting at 1 hidden node and stopping at 7 hidden nodes and 19,900 iterations. Since the model performed worse on the testing and validation datasets, as shown in Table 3, the train-all model was utilized to capture the logic within the testing and validation datasets and not included in the training datasets.

Table 1: Training, testing, validation, and train all statistics for the stress-controlled model

Training		Testing		Validation		Train All	
R^2	ASE	R^2	ASE	R^2	ASE	R^2	ASE
0.912	0.00132	0.873	0.00223	0.8681	0.00202	0.909	0.00138

The train-all model produced an excellent representation of the stress-strain curves involved. Accordingly, the final ANN model can be represented, as shown in equation (11).

$$\varepsilon\% = ANN_{2\text{-}[1\text{-}7\text{-}19,900]\text{-}1}[\sigma, wt.\%] \quad (11)$$

Where: 2: is the number of input variables [σ in MPa, wt. %], 1-7-19,900 represents the starting hidden node and the final hidden node and corresponding iterations. Lastly, 1 represents the number of output variables (ε %).

The connection weights and thresholds of the final network are shown in Table 2.

Table 2: Connection weights and thresholds (TS) of the stress-controlled model

	HN1	HN2	HN3	HN4	HN5	HN6	HN7
WT%	16.49	-38.44	-0.55	-0.60	-18.97	-15.98	-8.56

Stress	-4.38	3.86	-8.98	-4.41	8.06	4.23	-4.55	
TS 1	5.19	-3.65	10.48	-0.54	-4.96	-4.74	2.39	
	HN1	HN2	HN3	HN4	HN5	HN6	HN7	TS 2
Strain	-17.90	-25.90	-13.29	-15.73	5.30	11.72	3.49	29.90

3.3.2 Strain-controlled model

This model predicts the stress as a function of strain and wt. % of added GNP. The final model was obtained by adaptively training the network starting from 1 hidden node and stopping at 9 hidden nodes and 20,000 iterations. Since the model performed worse on the testing and validation datasets, as shown in Table 3, the train-all model was utilized to capture the logic within the testing and validation datasets and not included in the training datasets.

Table 3: Training, testing, and validation statistics for the strain-controlled model

Training		Testing		Validation		Train All	
R^2	ASE	R^2	ASE	R^2	ASE	R^2	ASE
0.936	0.00163	0.893	0.00276	0.858	0.00274	0.927	0.00171

The train-all model produced an excellent representation of the stress-strain curves involved. Accordingly, the final ANN model structure can be represented, as shown in equation (12).

$$\sigma = ANN_{2\text{-}[1\text{-}9\text{-}20,000]\text{-}1}[\varepsilon, \text{wt.}\%] \quad (12)$$

Similarly, 2: is the number of input variables [ε %, wt. %], 1-9-20,000 represents the starting hidden node and the final hidden node and corresponding iterations. Lastly, 1 represents the number of output variables (σ in MPa).

3.3.3 Stopping criterion model

In this model, the maximum strain is predicted as a function of the weight percent of added GNP. After performing the training process similar to the one used in the earlier models, the best performing model was obtained at 9 hidden nodes and 3,000 iterations. The statistical measures for the train-test model are shown in Table 4.

Table 4: Training, testing, and validation statistics for the stopping criterion model

Training		Testing		Validation		Train All	
R^2	ASE	R^2	ASE	R^2	ASE	R^2	ASE
0.817	0.00512	0.848	0.00411	0.885	0.0034	0.803	0.0055

The train-all model did not improve the prediction accuracy of the strain value at failure. Accordingly, the train-test ANN model was adopted, which can be represented, as shown in equation (13).

$$\varepsilon_{max}\%=\text{ANN}_{1\text{-}[1\text{-}9\text{-}3,000]\text{-}1}[\text{wt.}\%] \quad (13)$$

3.4 ANN Simulations

In this study, the stress-strain responses are predicted using the ANN approach. In this section, the ANN simulations using the developed models are compared with the experimental responses. Then a sensitivity analysis is performed for a range of 0-97 wt. %. Finally, the toughness, maximum tangent modulus, and maximum strength and strain values are calculated and compared with their corresponding experimental values.

3.4.1 Stress-strain simulations

In this section, both stress-controlled and strain-controlled models are simulated and compared with the experimental responses. A sample of simulations for wt.% = 0.5 wt.%, 25 wt.%, 40 wt.% and 85 wt.% are shown, respectively in Figure 8. As noted in Figure 8, the stress-controlled model outputs higher predictions while the strain-controlled model predicts lower values of stress. It is to be noted that the prediction accuracy of the developed models has been impacted by the discrepancy observed in the experimental data. Moreover, at higher percentages, the strain-controlled model seems to fit the experimental data better than the stress-controlled model. This observation is in accordance with the statistical accuracy measures (R2 & ASE) reported earlier. In this case, the stress-controlled model tends to

overestimate the stress values. All the ANN simulations compared with the experimental stress-strain curves are shown in APPENDIX B.

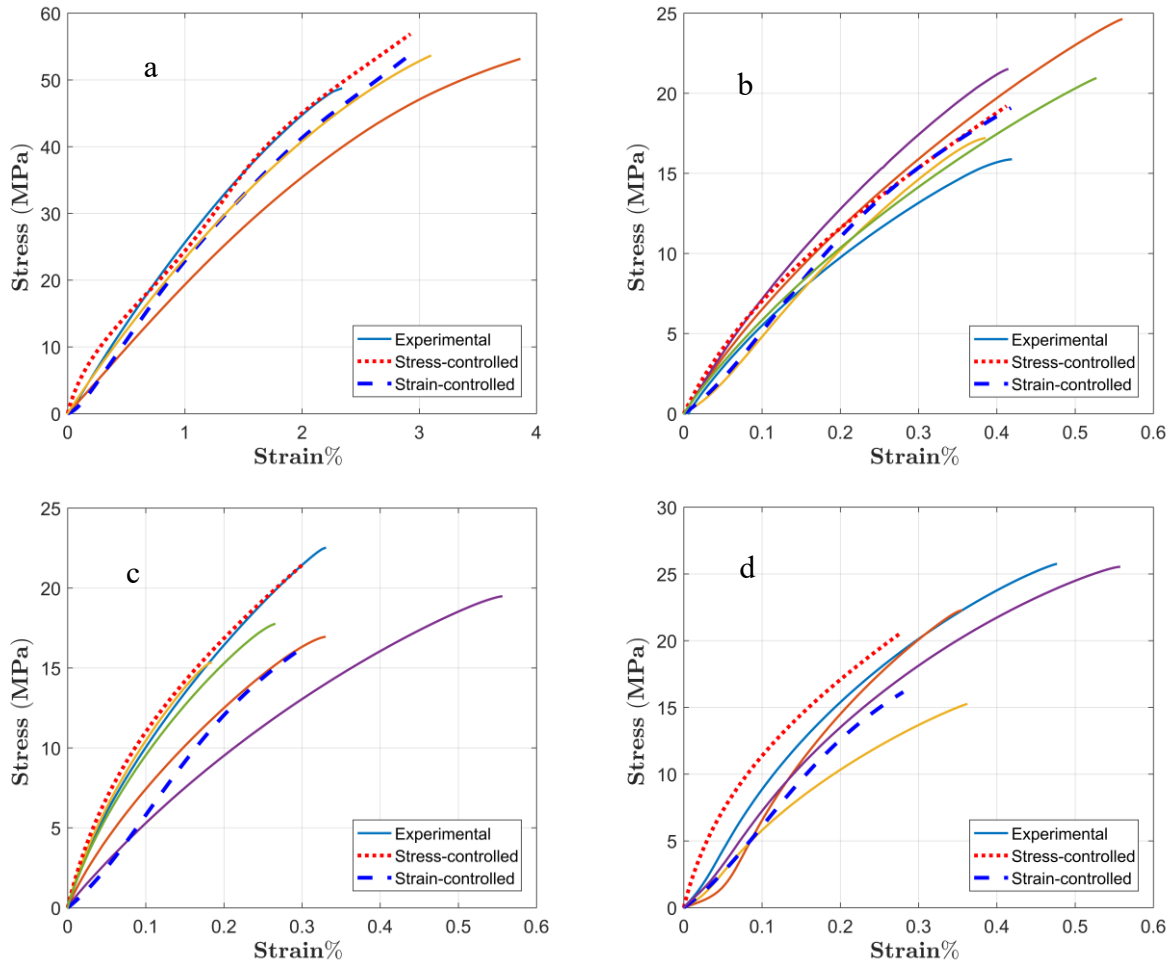

Figure 8: ANN simulations compared with experimental stress-strain curves for: a) 0.5 wt.% b) 25 wt.% c) 40 wt.% d) 85 wt.%

3.4.2 Sensitivity analysis

In this section, a sensitivity analysis is performed using both models, as shown in Figure 9 and Figure 10. The analysis was performed by changing the wt.% from 0 to 97% by an increment not higher than 1%. As observed in the figures below, both models predict a softening behavior of the material with an increase in graphene content, which may be due to clustering of the graphene within the material until the weight percent reaches approximately 10%. At this point, the platelets start to mechanically interlock, which enhances the strength of the material.

Finally, the material reaches a plateau where almost no more strength is developed beyond the 40 wt.%.

Moreover, it can also be observed from the figures below; the strain-controlled model seems to predict a lower strength for a given weight percent when compared with the value obtained from the stress-controlled model. This behavior is consistent with the observation noted in section 4.1. Additionally, for weight percentages between 0-1%, a finer simulation is done to capture any behavioral change in the material when a fraction of a percent is added. For this case, the strain-controlled model predicts less strength loss than the stress-controlled model. At 1%, the strain-controlled model predicts a loss of 26% while the stress-controlled model predicts a 35% strength loss.

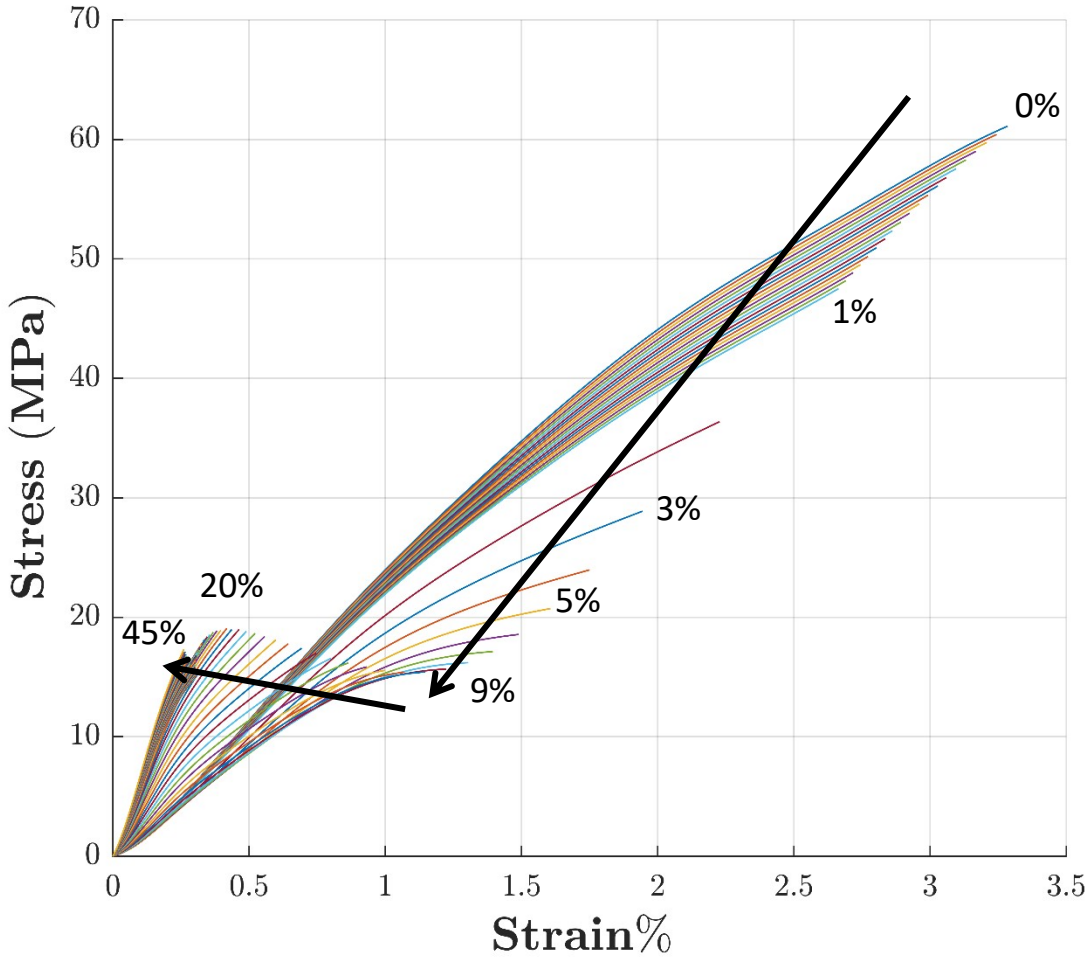

Figure 9: Sensitivity analysis simulation for the strain-controlled model

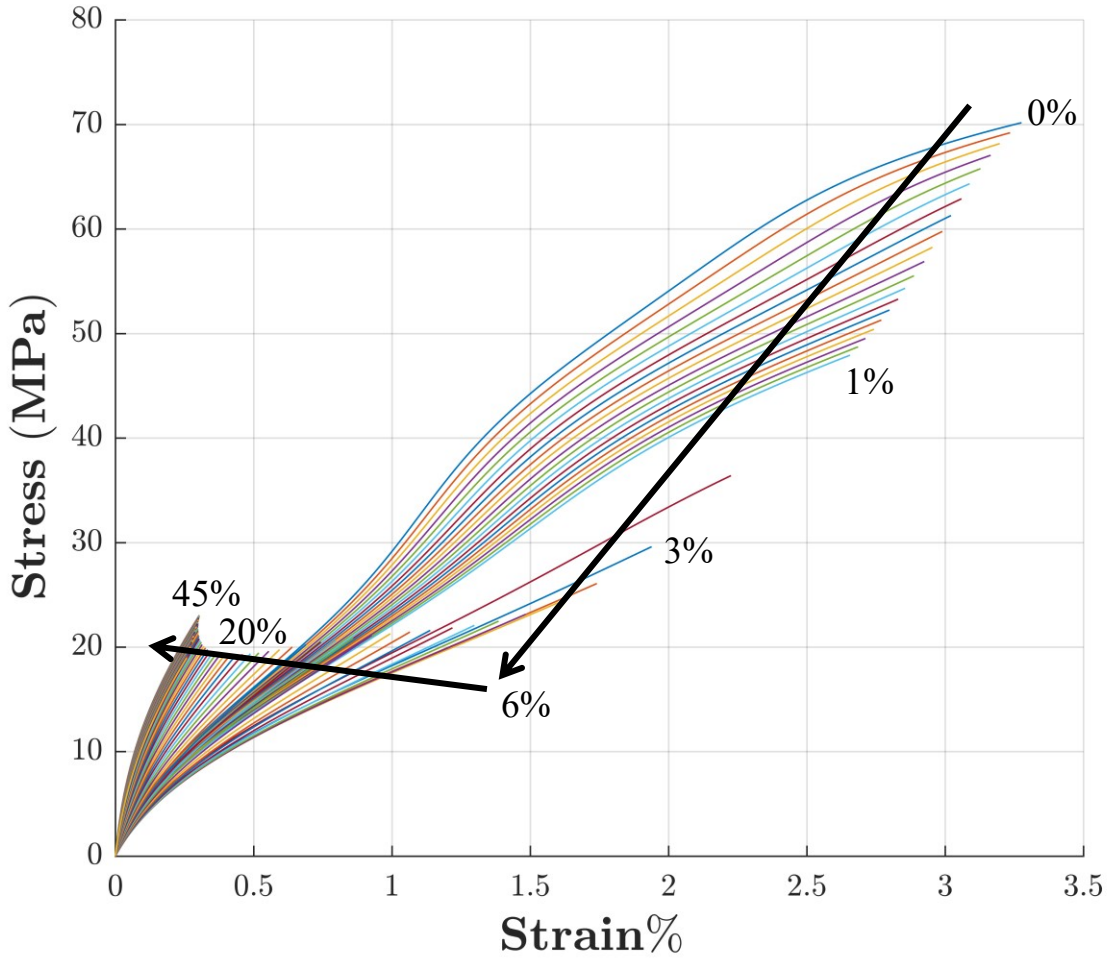

Figure 10: Sensitivity analysis simulation for the stress-controlled model

3.4.3 Mechanical Properties

In this section, the 4 different mechanical properties are calculated from the stress-strain responses simulated earlier, namely: the toughness, which essentially is the area under the curve; the maximum tangent modulus, which takes the maximum slope at each point for the entire curve; and the maximum stress and strain, which form the final points on the curve. These properties are calculated from the experimental test data as well as the predicted corresponding responses, shown in Figure 11.

The toughness curve in Figure 11a shows a rapid decrease in toughness until the weight percent of added GNPs reaches 40%, and then it stays almost unchanged. Both ANN models fall in the

middle of the experimental data. It can also be noted the strain-controlled model always predicts a lower toughness than the stress-controlled model. The same behavior can be concluded from the maximum tangent modulus in Figure 11b, where it is evident that the stress-controlled model defines the upper bound, and the other model depicts the lower bound. At low percentages (i.e., less than 10%) the stress-controlled model predicts a higher modulus than any of the experiments which is not the case with the other model where it almost falls right in the mid-range of the corresponding experimental-based data. The maximum strength behavior is shown in Figure 11c; it follows the same trend noted in the toughness case. The strength decreases until the added GNPs percentage reaches a minimum at 40 wt. %. Finally, the maximum strain is shown in Figure 11d, which is mostly plotting the results from the stopping criterion model since the maximum strain is used to terminate the simulation for both models. The stopping criterion ANN-based model shows excellent predictions of the maximum strain except at 20 wt. % where the experimental values of the maximum strain increase at 20 wt. % then drops back for the 25 wt.%. The same plateau noted earlier at 40 wt. % can also be pointed out in this case as well.

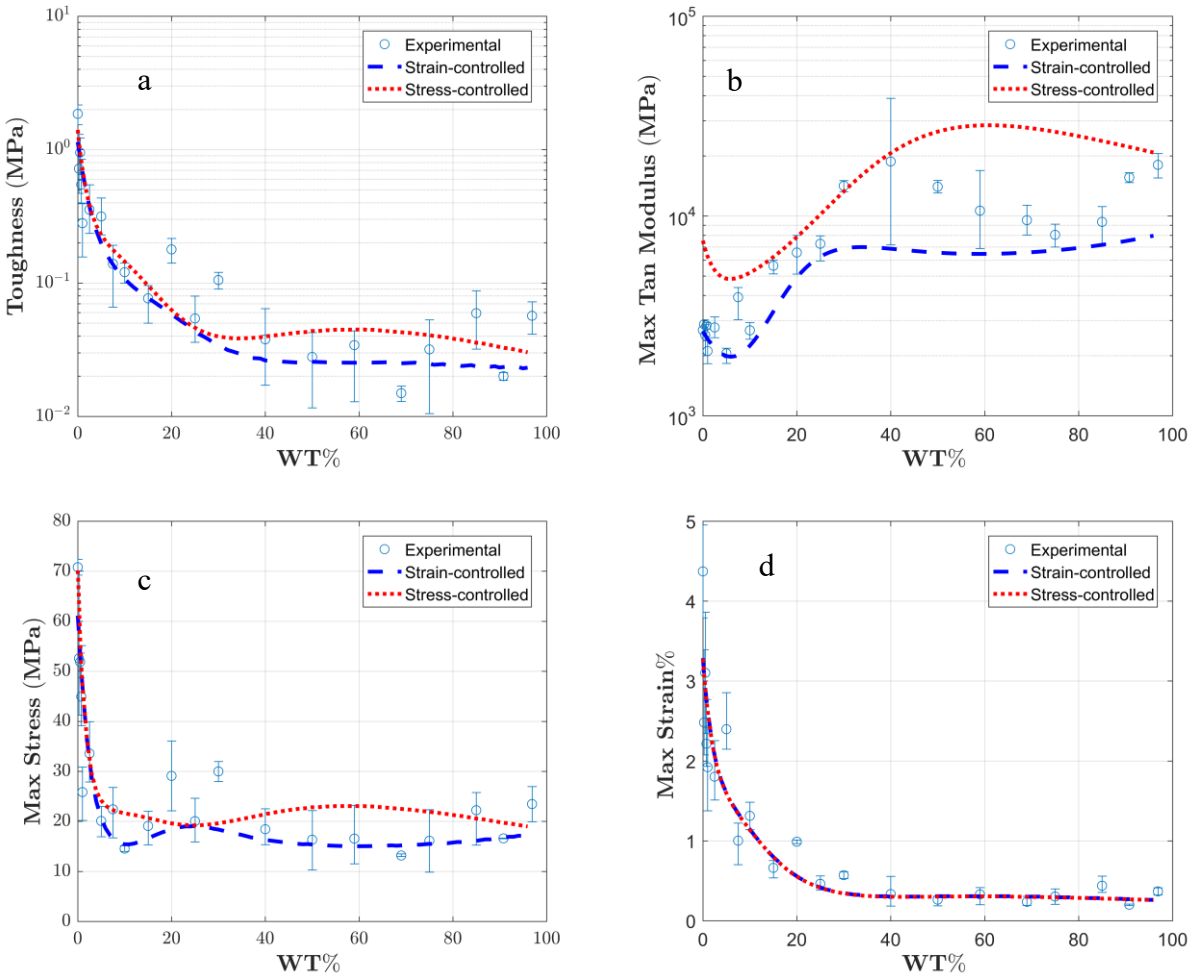

Figure 11: Mechanical properties calculated from the stress-strain responses; a) toughness b) maximum tangent modulus c) maximum strength d) maximum strain

3.5 Graphical User Interface (GUI)

In order to make the models more accessible, an Excel GUI is created. In this GUI, all three models were programmed in separate sheets. All the connection weights necessary calculations are done within these sheets. The interface, shown in Figure 12, is comprised of three parts; WT% slider bar, mechanical properties table, and upper and lower limit stress-strain curves. The WT% slider bar is the only input needed from the user to set the desired WT% of added graphene. The mechanical properties are calculated instantaneously. Finally, the stress-strain

curves for the upper and lower limits are plotted. The stress-controlled model is considered as the upper limit and the strain-controlled model as the lower limit.

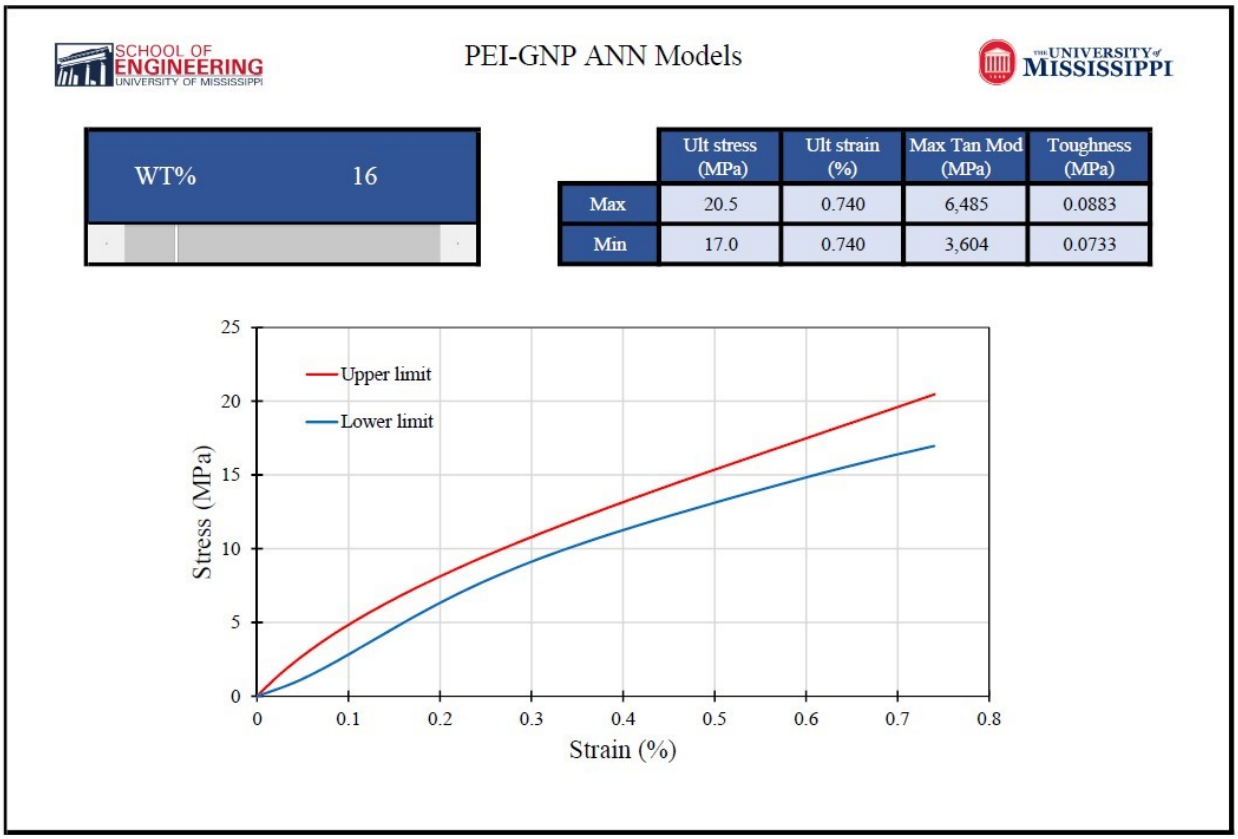

Figure 12: Graphical User Interface for PEI-GNP Nanocomposites

3.6 Conclusions

Graphene nanocomposites exhibit a variation in mechanical properties. In this research, the mechanical properties of PEIGNP composites are studied, including the toughness, maximum tangent modulus, maximum strength, and strain.

- PEIGNPs were manufactured with varying graphene loading ranging from 0-97%.
- The papers were tested using a standard stress-controlled tension test via Dynamic Mechanical Analyzer, DMA Q800.
- A total of 71 samples were tested, and the corresponding stress-strain curves were obtained.

- Two ANN models were developed; the first was a strain-controlled model (i.e., strain-input), and the other was a stress-controlled model.
- Another ANN model was developed and incorporated to predict the maximum strain at a given wt.%.
- The strain-controlled model tends to predict lower values for the mechanical properties while the stress-controlled model tends to predict higher values.
- Toughness, Strength, and Ductility decrease until the WT% reaches 40% then it stays almost unchanged
- Stiffness keeps decreasing for wt.% 0-10% until reaching to 40 wt.%.
- Both stress and strain-controlled models showed excellent agreement with the experimentally observed data with R^2 of 0.909 and 0.927, respectively.
- By employing the developed ANN stress- and strain-controlled models, the stress-strain response can be efficiently simulated at any given wt.%.
- Finally, the developed ANN models are utilized to create a GUI to aid in future material design.

4. DAM OVERTOPPING FAILURE

Dam Failure is a disastrous type of failure can be described as an unexpected, rapid, and unrestrained discharge of impounded water. This failure can be due to deterioration of the dam soil condition or due to extreme loading the dam wasn't designed to withstand. It is essential to prepare for emergencies like dam failure, especially high-hazard potential dams. It is also vital to predict dam failure before the incident itself to provide time to execute emergency plans.

Additionally, post-failure behavior is essential to predict the extent of the damage caused by this event. Many studies have been carried out in this area. Failure parameters such as; peak discharge, time to fail, and others are often used to describe dam failure. However, most researchers assume one type of failure due to dam overtopping, which starts with the assumption of initial damage to the crest of the dam and study its progression. Additionally, all the collected data from literature only provide dam geometry, the volume of impounded water, as well as the corresponding failure parameters.

In this research, Numerical simulations are performed considering the geotechnical behavior of soil as well as the hydraulic flow of water through the dam body (seepage) and water overtopping (surface flow). Smoothed Particle Hydrodynamics (SPH) is employed to perform the numerical simulation. SPH is especially attractive in post failure analyses due to its meshless representation of the material, which avoids numerical instability and mesh distortion. In this chapter, the SPH modeling of soil is discussed first. After that, the development of the numerical model and numerical simulations are performed and processed. Finally, the ANN models and the graphical user interface are developed. Smoothed Particle Hydrodynamics (SPH)

Smoothed Particle Hydrodynamics (SPH) is a Lagrangian meshless numerical method used to obtain the solution of fluid and continuum dynamics equations by replacing the fluid and/or continuum with particles. The material is discretized into Particles that have material properties such as density, velocity, and stress. These particles move according to their defined governing equations. Particle interaction is only calculated within a certain radius called smoothing distance (h). The weight of each particle contribution is calculated using a kernel function (W). The Choice of the smoothing distance and kernel function affects the stability, accuracy, and the efficiency of the numerical solution (Monaghan 1994). The most used kernel function developed by (Monaghan 1994) is the cubic spline function shown in equation (14).

$$W_{ab} = W(r_{ij}, h) = \alpha_d \begin{cases} 1 - \frac{3}{2}q^2 + \frac{3}{4}q^3 & 0 \le q \le 1 \\ \frac{1}{4}(2-q)^2 & 1 \le q \le 2 \\ 0 & q \ge 2 \end{cases} \quad (14)$$

Where: Subscript i: denotes the integration point particle

Subscript j: indicates the neighboring particles

r_{ij}: The distance between particles i and j

h: The Smoothing range

q: The non-dimensional distance between particles $q = \frac{r_{ab}}{h}$

α_d: Dimensional normalizing factor, $\alpha_d = \frac{10}{7\pi h^2}$ in 2D and $\alpha_d = \frac{1}{\pi h^3}$ in 3D

SPH utilizes an interpolation technique to represent any field function $f(x_i)$ for each particle along the particles' neighboring particles using the following approximation

$$f(x_i) = \sum_{j=1}^{N} \frac{m_j}{\rho_j} f(x_j) W_{ij} \quad (15)$$

$$\frac{\partial f(x_i)}{\partial x} = \sum_{j=1}^{N} \frac{m_j}{\rho_j} f(x_j) W_{ij} \cdot \frac{\partial W_{ij}}{\partial x_i} \quad (16)$$

Where: N: Number of neighboring particles

m, ρ: mass and density of the particle, respectively.

In the last decade, SPH has been used for various geomechanical applications, such as; soil stability, soil structures failure, and hydraulically loaded soil embankments. Saturated soils are generally modeled as two separate layers; Soil and water layer, as illustrated in Figure 13. Each layer is simulated separately, and the interaction between the layers is modeled in two parts. Surface particles exhibit lift and drag forces, and deep soil particles experience seepage forces. Modeling each layer is discussed extensively in the next sections. After that, soil-water interaction and numerical challenges are examined. Finally, the simulated numerical model parameters are defined.

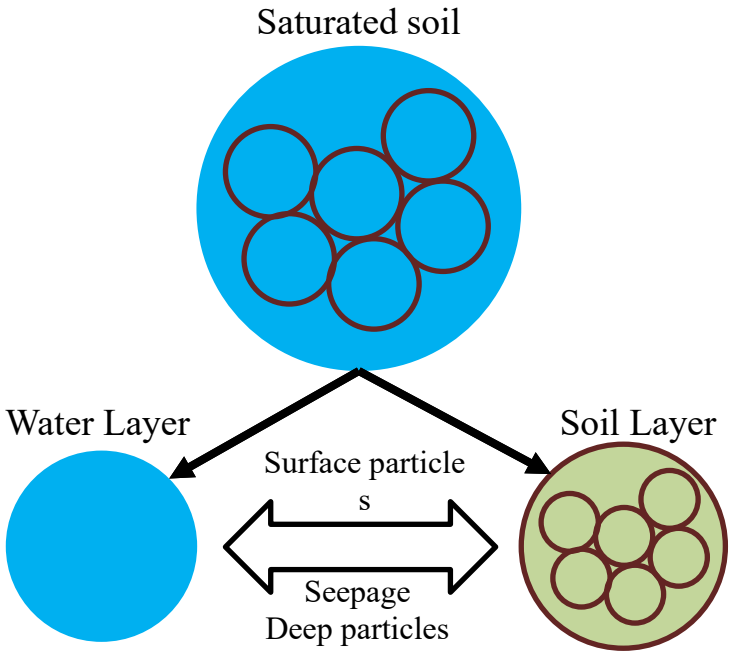

Figure 13: Saturated Soil Model in SPH formulation

4.1.1 Water Layer

Water is simulated as a weakly incompressible viscous fluid utilizing Weakly Compressible SPH (WCSPH). The conservation of mass and momentum equations govern the fluid motion in the Lagrangian space, also known as Navier-Stocks equations, equations (17) and (18).

$$\frac{D\rho_a}{Dt} = -\rho_a \frac{\partial v^\alpha}{\partial x^\alpha} \tag{17}$$

$$\frac{Dv_a^\alpha}{Dt} = \frac{1}{\rho}\frac{\partial \sigma^{\alpha\beta}}{\partial x^\beta} + f^\alpha \quad (18)$$

Where: $\sigma^{\alpha\beta} = -p\delta^{\alpha\beta} + \tau^{\alpha\beta}$

$\tau^{\alpha\beta} = \mu\varepsilon^{\alpha\beta}$

f^α: Acceleration due to external forces

$\frac{D}{Dt}$: material derivative which is defined as $\frac{D}{Dt} = \frac{\partial}{\partial t} + v^\alpha \frac{\partial}{\partial x^\alpha}$

$\sigma^{\alpha\beta}$: Stress Tensor

p: Thermodynamic Pressure

$\delta^{\alpha\beta}$: Kronecker delta

$\tau^{\alpha\beta}$: Shear stress

μ: Dynamic viscosity

$\varepsilon^{\alpha\beta}$: Shear strain

The pressure p is calculated via the Equation of State (EOS). There are many forms of EOS for fluid simulations. The choice of EOS depends on the material and application. In this research equation (19) developed by (Monaghan 1994) shown below is utilized. This equation has been widely used in WCSPH. The assumption of the speed of sound c_s directly affects the time step and the stability of the simulation. Subsequently, it is recommended to assume cs equal or to more than 10U. Where U is the upstream velocity of the flow (Bui et al. 2007; Korzani et al. 2017; Monaghan 1994). This assumption limits the fluctuation in water density to less than 1% (Bui et al. 2007).

$$p = \frac{\rho_0 c_s^2}{7}\left[\left(\frac{\rho}{\rho_o}\right)^7 - 1\right] \quad (19)$$

Where: ρ_0: Reference density (density at rest)

c_s: Speed of sound

Navier-Stocks equations are written in the SPH formulation as follows (Korzani et al. 2017):

$$\frac{d\rho_i}{dt} = \rho_i \sum_j \frac{m_j}{\rho_j}(v_i - v_j) \cdot \nabla W_{ij} \tag{20}$$

$$\frac{dv_i}{dt} = -\sum_j m_j \left(\frac{p_i}{\rho_i^2} + \frac{p_j}{\rho_j^2}\right) \nabla W_{ij} + \left\{\frac{\mu}{\rho} \nabla^2 v\right\}_i \tag{21}$$

Where: ∇: The gradient with respect to the coordinates of particle a

The resulting water model requires three parameters for proper definition using the SPH formulation; density, dynamic viscosity, and speed of sound.

4.1.2 Soil Layer

The conservation of momentum equation (18) is used to define the soil motion and written in the SPH formulation as follows:

$$\frac{dv_i^\alpha}{dt} = \sum_j m_j \left(\frac{\sigma^{\alpha\beta}{}_i}{\rho_i^2} + \frac{\sigma^{\alpha\beta}{}_j}{\rho_j^2}\right) \frac{\partial W_{ij}}{\partial x_i^\beta} + f^\alpha \tag{22}$$

The stress tensor consists of two components; hydrostatic pressure p, and deviatoric shear stress $s^{\alpha\beta}$, as shown in equation (23) below.

$$\sigma^{\alpha\beta} = -p\delta^{\alpha\beta} + s^{\alpha\beta} \tag{23}$$

Where: $s^{\alpha\beta}$: Deviatoric shear stress

The pressure p is calculated using the mean stress definition, equation (24), as opposed to the EOS calculations for the water layer (Korzani et al. 2018a).

$$p = -\frac{1}{3}(\sigma^{\alpha\alpha} + \sigma^{\beta\beta} + \sigma^{\gamma\gamma}) \tag{24}$$

Where: $\sigma^{\alpha\alpha}, \sigma^{\beta\beta}, \sigma^{\gamma\gamma}$: Normal stresses in X, Y, and Z directions

Traditionally, the soil is modeled as an elastic-perfectly plastic material. Thus, it is usually represented by the Drucker-Prager model with a non-associated flow rule (Bui et al. 2008b). Drucker-Prager model is described using the following equation.

$$f(I_1, J_2) = \sqrt{J_2} + \alpha_\phi I_1 - k_c = 0 \tag{25}$$

Where I_1, and J_2 are the first and second invariants of the stress tensor. Which are given by equations (26) and (27), respectively. Additionally, α_ϕ, and k_c are Drucker-Prager constants,

which are related to the soil cohesion (c) and angle of friction (ϕ), equations (28) and (29), respectively.

$$I_1 = \frac{1}{3}\left(\sigma^{\alpha\alpha} + \sigma^{\beta\beta} + \sigma^{\gamma\gamma}\right) \tag{26}$$

$$J_2 = \frac{1}{2} s^{\alpha\beta} s^{\alpha\beta} \tag{27}$$

$$\alpha_\phi = \frac{\tan\phi}{\sqrt{9+12\tan^2\phi}} \tag{28}$$

$$k_c = \frac{3c}{\sqrt{9+12\tan^2\phi}} \tag{29}$$

The stress-strain relationship was derived in details by (Bui et al. 2008b) and written in the form shown in the following equation.

$$\frac{d\sigma_i^{\alpha\beta}}{dt} = \sigma_i^{\alpha\gamma}\dot{\omega}_i^{\beta\gamma} + \sigma_i^{\gamma\beta}\dot{\omega}_i^{\alpha\gamma} + 2\,G_i\dot{e}_i^{\alpha\beta} + K_i\varepsilon_i^{\gamma\gamma}\delta_i^{\alpha\beta} - \dot{\lambda}_i\left[9K_i\sin\psi_i\,\delta^{\alpha\beta} + \left(\frac{G}{\sqrt{J2}}\right)_i s_i^{\alpha\beta}\right] \tag{30}$$

$$\dot{\lambda}_i = \frac{3\alpha_\phi K\dot{\varepsilon}_i^{\gamma\gamma} + \left(\frac{G}{\sqrt{J2}}\right)s_i^{\alpha\beta}\varepsilon_i^{\alpha\beta}}{27\,\alpha_\phi K_i\sin\psi_i + G_i} \tag{31}$$

$$\dot{e}_i^{\alpha\beta} = \dot{\varepsilon}_i^{\alpha\beta} - \frac{1}{3}\dot{\varepsilon}_i^{\gamma\gamma}\delta_i^{\alpha\beta} \tag{32}$$

Where: $\dot{e}_i^{\alpha\beta}$: Deviatoric shear strain tensor,

$\varepsilon_i^{\alpha\beta}$, $\dot{\omega}_i^{\beta\gamma}$: Strain rate, and Spin rate, respectively.

G_i, K_i: Shear and Bulk moduli, respectively.

$\dot{\lambda}_i$: Plastic flow multiplier

ψ_i: Dilatancy angle

The strain and spin rates are calculated using equations (33) and (34) and written in SPH formulation for as shown in equations (35) and (36), respectively.

$$\dot{\varepsilon}_i^{\alpha\beta} = \frac{1}{2}\left(\frac{\partial v^\alpha}{\partial x^\beta} + \frac{\partial v^\beta}{\partial x^\alpha}\right)_i \tag{33}$$

$$\dot{\omega}_i^{\alpha\beta} = \frac{1}{2}\left(\frac{\partial v^\alpha}{\partial x^\beta} - \frac{\partial v^\beta}{\partial x^\alpha}\right)_i \tag{34}$$

$$\dot{\varepsilon}_i^{\alpha\beta} = \frac{1}{2}\left[\sum_{j=1}^{N} \frac{m_j}{\rho_j}\left(v_j^{\alpha} - v_i^{\alpha}\right)\frac{\partial W_{ij}}{\partial x_i^{\beta}} + \sum_{j=1}^{N} \frac{m_j}{\rho_j}\left(v_j^{\beta} - v_i^{\beta}\right)\frac{\partial W_{ij}}{\partial x_i^{\alpha}}\right] \quad (35)$$

$$\dot{\omega}_i^{\alpha\beta} = \frac{1}{2}\left[\sum_{j=1}^{N} \frac{m_j}{\rho_j}\left(v_j^{\alpha} - v_i^{\alpha}\right)\frac{\partial W_{ij}}{\partial x_i^{\beta}} - \sum_{j=1}^{N} \frac{m_j}{\rho_j}\left(v_j^{\beta} - v_i^{\beta}\right)\frac{\partial W_{ij}}{\partial x_i^{\alpha}}\right] \quad (36)$$

The resulting soil model requires five parameters for proper definition using the SPH formulation; density, cohesion, angle of friction, dilatancy angle, and bulk modulus.

4.1.3 Soil – Water interaction

The interaction between the soil and water layers is divided into two types; surface particles interaction, and deep particles interaction (Korzani et al. 2018c). Surface particles encounter lift and drag forces (Dong and Zhang 1999; Li et al. 2008), equations (37), and (38). And deep particles undergo seepage forces. Which is calculated using the Forchheimer Equation and Den Adel Coefficients, equation (42) (Korzani et al. 2018a).

$$f_x = \frac{3}{4d_{15}} \rho_f \, c \, C_D \, u_r \sqrt{u_r^2 + v_r^2} \quad (37)$$

$$f_y = \frac{3}{4d_{15}} \rho_f \, c \, C_D \, u_r \sqrt{u_r^2 + v_r^2} + \frac{3}{4} \rho_f \, c \, C_L \, |u_r| \frac{\partial u_r}{\partial y} \quad (38)$$

$$u_r = u_f - u_s \quad (39)$$

$$v_r = v_f - v_s \quad (40)$$

$$C_D = \frac{24\,\nu}{d_{15}\sqrt{u_r^2 + v_r^2}} + 2 \quad (41)$$

$$f_{seepage} = a\left(v_f - v_s\right)\gamma_f + b\left|v_f - v_s\right|\left(v_f - v_s\right)\gamma_f \quad (42)$$

$$a = \alpha \frac{(1-n)^2}{n^3} \frac{\nu}{g\, d_{15}} \quad (43)$$

$$b = \beta \frac{1}{n^2} \frac{1}{g\, d_{15}} \quad (44)$$

Where: u_r , v_r: Relative velocities between the fluid and soil particles in the horizontal and vertical directions, respectively.

Subscripts f and s: stand for fluid and soil particles, respectively.

C_L and C_D: Lift and drag coefficients.

c: Soil volumetric concentration, $c = 1 - n$.

n: Porosity

d_{15}: effective soil particle size

α, β: constants set as $\alpha = 150$, $\beta = 0.4$ (Korzani et al. 2018b)

g: Gravity acceleration.

ν: kinematic viscosity

Finally, in the case of saturated soils, effective stress is used in the equation of motion (22) instead of the total stress. The pore water effect is taken into account by using the effective density of the soil instead of the saturated density (Korzani et al. 2018b).

The resulting soil-water interaction requires two parameters for proper definition using the SPH formulation; soil porosity and effective diameter.

4.1.4 Numerical issues

Two issues are encountered when modeling solids and fluids in SPH; tensile instability, and unphysical particle penetration (Gray et al. 2001; Monaghan and Pongracic 1985). Tensile instability presents as clumping of particles during plastic flow. This problem is solved by introducing an artificial stress term to the equation of motion (45) (Gray et al. 2001). This term is only added to the particles in tension. Therefore, the principal stresses are calculated first to determine whether the particle in tension or not. Then, the artificial stress is added to the principal stresses. After that, the new stress tensor is found by rotating the coordinates back to its original orientation. The artificial stress is given by equations (46) to (48):

$$\left(\frac{\sigma^{\alpha\beta}{}_i}{\rho_i^2} + \frac{\sigma^{\alpha\beta}{}_j}{\rho_j^2}\right) \rightarrow \left(\frac{\bar{\sigma}^{\alpha\beta}{}_i}{\rho_i^2} + \frac{\bar{\sigma}^{\alpha\beta}{}_j}{\rho_j^2} + \bar{R}_{ij}^{\alpha\beta} f_{ij}^n\right) \tag{45}$$

$$\bar{R}_{ij}^{\alpha\beta} = \bar{R}_i^{\alpha\beta} + \bar{R}_j^{\alpha\beta} \tag{46}$$

$$\bar{R}_i^{\alpha\beta} = -\epsilon \frac{\bar{\sigma}_i^{\alpha\beta}}{\rho_i^2} \tag{47}$$

$$f_{ij} = \frac{W(r_{ij})}{W(\Delta P)} \tag{48}$$

Where: n and ϵ: Constants set as 2.55 and 0.5 (Bui et al. 2008b).

ΔP: Particle spacing (constant).

Artificial viscosity term is also introduced into the stress term of the equation of motion. The updated stress term is shown in equation (49). Artificial viscosity is calculated using equations (50) to (55).

$$\left(\frac{\sigma^{\alpha\beta}{}_i}{\rho_i^2} + \frac{\sigma^{\alpha\beta}{}_j}{\rho_j^2} + \bar{R}_{ij}^{\alpha\beta} f_{ij}^n\right) \rightarrow \left(\frac{\bar{\sigma}^{\alpha\beta}{}_i}{\rho_i^2} + \frac{\bar{\sigma}^{\alpha\beta}{}_j}{\rho_j^2} + \bar{R}_{ij}^{\alpha\beta} f_{ij}^n + \Pi_{ij}\delta^{\alpha\beta}\right) \tag{49}$$

$$\Pi_{ab} = \begin{cases} \frac{-\alpha \bar{c}_{ab}\mu_{ab} + \beta\mu_{ab}^2}{\bar{\rho}_{ab}^2}, & \boldsymbol{v}_{ab} \cdot \boldsymbol{x}_{ab} < 0 \\ 0, & \boldsymbol{v}_{ab} \cdot \boldsymbol{x}_{ab} \geq 0 \end{cases} \tag{50}$$

$$\bar{c}_{ab} = \frac{1}{2}(c_a + c_b) \tag{51}$$

$$\mu_{ab} = \frac{h_{ab}\boldsymbol{v}_{ab}\boldsymbol{x}_{ab}}{r_{ab}^2 + 0.1\, h_{ab}} \tag{52}$$

$$\bar{\rho}_{ab} = \frac{1}{2}(\rho_a + \rho_b) \tag{53}$$

$$\boldsymbol{v}_{ab} = \boldsymbol{v}_a - \boldsymbol{v}_b \tag{54}$$

$$\boldsymbol{x}_{ab} = \boldsymbol{x}_a - \boldsymbol{x}_b \tag{55}$$

Where: α, β: Constants set as 0.1 (Bui et al. 2008b)

c_a: Speed of sound for particle a

$\boldsymbol{x}$, $\boldsymbol{v}$: Position and velocity vectors

In conclusion, to accurately define a saturated soil model, several parameters are required; water parameters; namely, water density, viscosity and speed of sound, and soil parameters; including, soil density, angle of friction, cohesion, effective diameter, and porosity.

4.1.5 Software validation

The software used in this research, "PersianSPH," is developed by Dr. Korzani (Korzani 2015). This software is a C++ based algorithm on the Linux platform. It can perform coupled

simulations for solids, fluids, and structures in 2D as well as 3D. It is especially suitable for post-failure analysis and soil-water interactions.

To validate the software, two problems are simulated and compared with the corresponding experiment. The first experiment is performed to validate the soil failure model in the SPH platform. The second experiment is performed to validate the soil-water interaction.

4.1.5.1 Sandbox failure

In this section, a 2D simulation of a sand column collapse is performed. This experiment has been studied previously by (Bui et al. 2008a). Since the numerical simulation is performed in 2D, the test was designed to reflect it. (Bui et al. 2008a) used aluminum bars with diameters of 1 and 1.5 mm and a density of 2650 kg/m^3. The bars were arranged in a 200x100 mm box. The equivalent soil properties such as cohesion (c), friction angle (φ), and elastic bulk modulus (K) were measured for the aluminum bars using a shear box experiment. The cohesion (c) was found to be zero, the friction angle (φ) was 19.8º, and the elastic bulk modulus was 0.7 MPa. The numerical model is defined in 2D with the same properties mentioned earlier. The particle size is set as 2 mm. The final surface configuration, as well as the failure surface, are compared to the experiment. Figure 14 depicts the final soil configuration for the experiment performed by (Bui et al. 2008a) as well as the SPH simulation using PersianSPH software.

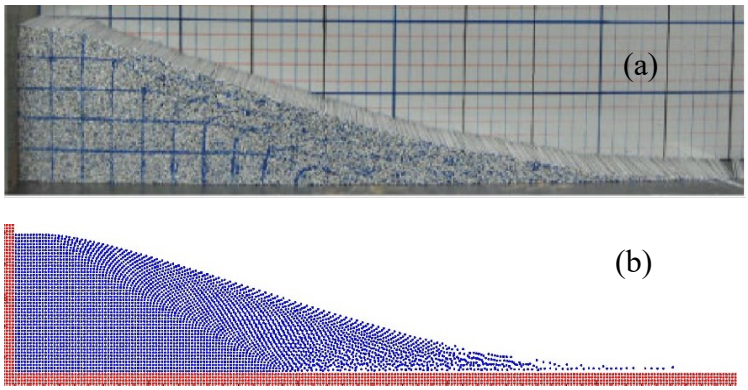

Figure 14: Sandbox failure, (a) Experiment (Bui et al. 2008a) (b) SPH simulation

The SPH simulation shows an excellent correlation to the experimental results. This is further shown in Figure 15. The failure surface and final surface configuration of the SPH simulation agree with the experiment. This result indicates that PersianSPH software can simulate large deformation soil problems with excellent accuracy.

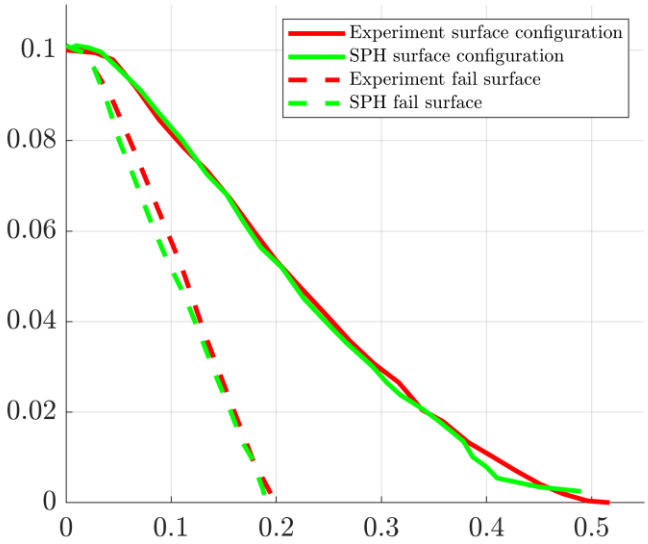

Figure 15: Sandbox failure surface and surface configuration

4.1.5.2 Phreatic surface in a rock-fill embankment

In this section, fluid flow through porous media is studied and compared with experimental results. The experiment utilized in this study was conducted by (Larese et al. 2013). In this experiment, a rock-fill embankment made of gravel with porosity (n) of 0.41 and effective diameter (D_{15}) of 25.5 mm. The phreatic surface was measured using pressure sensors installed at the bottom of the embankment. Two different flow rates were introduced from the upstream side, 25.46 L/s, and 51.75 L/s.

The same soil configuration was modeled using PersianSPH software. An excellent correlation between the experiment and the numerical simulation was found in both cases for the available points of the test, as seen in Figure 16. This shows that the software is also capable of simulating water flow through porous media with precision.

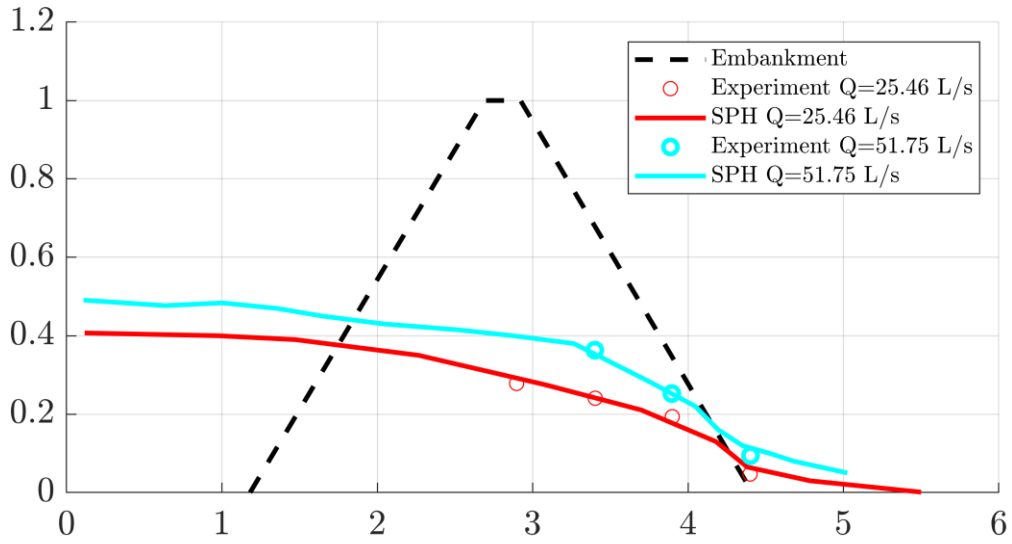

Figure 16: Phreatic Surface within a rock-fill embankment

4.2 Numerical simulations

In the purpose of developing superior ANN model, the training database is essential to encompass many variations of each variable that governs the outcome of the problem. In this case, dam overtopping behavior. There are many parameters to be designed for an earthen embankment, including; physical and engineering parameters. Physical parameters include geometry, type, specially designed sections such as wave protection surface treatment, filters, spillways, and many others. Engineering parameters include soil properties such as density, cohesion, angle of friction, compaction, Elastic modulus, grain size distribution, and porosity. Moreover, extreme events vary in intensity and type of loading on the embankment. The magnitude of loading can be represented in water elevation on the upstream side of the embankment. Water elevation can be constant over time or vary over time in a wave-like manner. In this study, only homogenous embankments with a maximum height of 15m are studied.

As discussed earlier, five parameters are needed to define soil material properties; density, angle of friction, cohesion, porosity, and effective diameter. Additionally, another three

parameters are required to define the geometry of the dam; dam height, crest width, and side slope. In this context, more than 65,000 simulations are needed to build the database, if only four variations of each parameter are considered. Moreover, some of these combinations could represent an artificial soil, as soil parameters are interrelated, for example, a change in cohesion would affect porosity or angle of friction and vice versa. To evade this problem, each section of the soil model is considered as a whole, and only soil type is changed.

It is crucial to select soil types with properties that envelop the range for each property of soil. In this research, the chosen soil types for the foundation section are; medium compaction high plasticity clay, well-graded gravel, dense silty gravel, loose high plasticity slit, and dense high plasticity silt. The properties of each soil type are shown in Table 5.

Table 5: Foundation section soil properties

	Density (kg/m3)	Cohesion (kPa)	Friction angle	Elastic modulus (MPa)	Porosity	Diameter (m)
CH	1890	11	19	7	0.39	4.2E-04
GM	2320	0	34	20	0.17	4.0E-02
MH	1930	50	18	2	0.53	8.0E-03
GW	2370	0	40	30	0.27	5.0E-02
ML	2220	22	27	15	0.42	8.0E-03

The selected soil types for the embankment section are; dense compacted high plasticity clay, dense silty gravel, compacted high plasticity silt and compacted clayey sand. The properties for each soil type are shown in Table 6. Porous soil options are excluded since it doesn't make sense to build a dam using highly porous material.

Table 6: Embankment section soil properties

	Density (kg/m^3)	Cohesion (kPa)	Friction angle	Elastic modulus (MPa)	Porosity	Diameter (m)
CH	2090	103	19	32	0.39	4.2E-04
GM	2420	5	40	35	0.17	4.0E-02
MH	2130	72	18	10	0.53	8.0E-03
SC	2150	11	31	20	0.15	1.0E-03

The embankment crest width is kept constant at 3 meters. Three different values are considered for the slope ranging between 1.2-3:1 (H:V). And four values are set for height ranging between 3-15 m.

In conclusion, the model is divided into embankment and foundation sections. Four different soil types are considered for dam section, whereas Five soil types for the foundation section. Embankment geometry parameters are identified as; height, slope, and crest width. Three different values are considered for the slope ranging between 1.2-3:1 (H:V). And Four values are set for height ranging between 3-15 m. The embankment width is kept constant at 3 m. The total number of simulations to be considered in this study is 240 simulations, as shown in Figure 17. The modeling parameters for each simulation are shown in APPENDIX C.

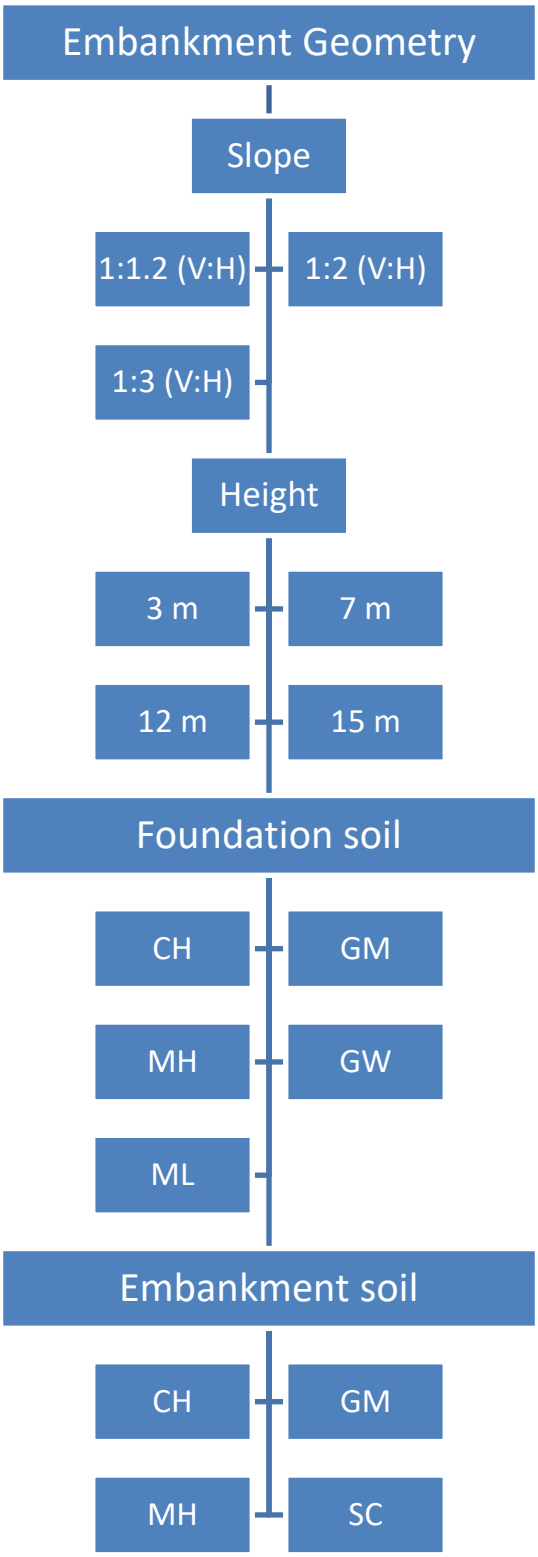

Figure 17: Numerical Simulations Database

4.3 Numerical Model

In this study, earthen embankment behavior is studied during a water overtopping event. The numerical simulations are performed using an SPH code developed by Dr. Korzani "PersianSPH" (Korzani 2015). The soil layer, shown in Figure 18, is divided into dam and foundation sections. Each section has different soil properties. Dam geometry parameters are identified as height, slope, and crest width.

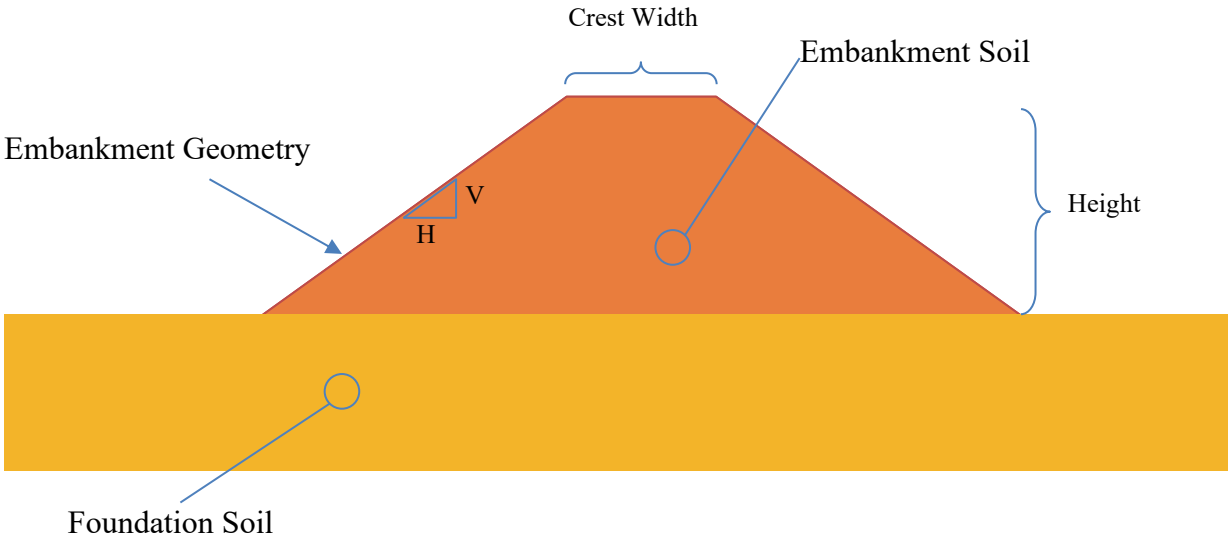

Figure 18: Typical configuration of the soil layer

The water layer, shown in Figure 19, is defined as one section filling the embankment and foundation section as well. Additionally, the height of the water is increased beyond the height of the embankment by H_w to simulate water overtopping. Which is kept constant at 0.5m in all the performed simulations.

Particle size (r_{in}) is chosen to be equal to 0.1m for the soil particles as well as the water particles based on the convergence study discussed in the next section. The smoothing length (h) is set as $1.2*r_{in}$ as well (Bui et al. 2007).

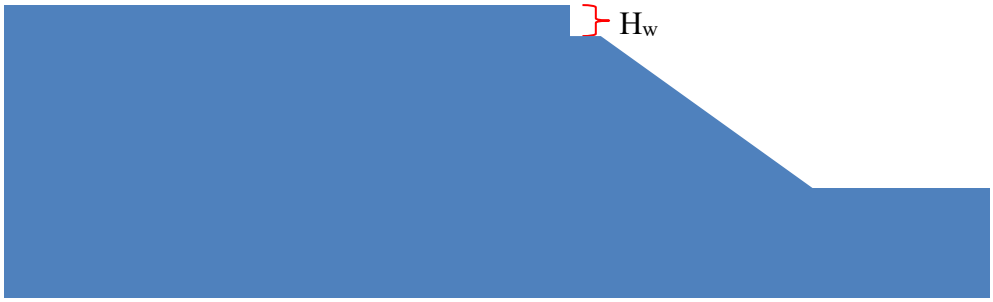

Figure 19: Typical configuration of the water layer

4.3.1 Convergence study

There are many numerical parameters to be considered in this study, namely, particle size (r_{in}), smoothing distance (h), artificial viscosity and artificial stress coefficients, and seepage flow coefficients (Den Adel coefficients). In this study, the smoothing distance is set to be equal to $1.2xr_{in}$, (Bui et al. 2008b), artificial viscosity coefficients α, β: set as 0.1, and artificial stress coefficients n and ϵ set as 2.55 and 0.5, respectively, (Bui et al. 2008b), and the seepage flow coefficients $\alpha,$ and β are set to be 150, and 0.4 respectively, (Korzani et al. 2018b).

Finally, the initial particle size is optimized, which is problem dependent. In this research, particle sizes ranging from 0.05m to 0.25m are considered. One simulation is performed for each particle size considering one variation of the simulation database. For this simulation, the embankment height is 3m, and the side slope is 1:1.2 (H:V). The embankment soil is silty gravel (GM), and the foundation soil is high plasticity clay (CH).

As depicted in Figure 20, the failure mode is the same in all simulations, which is embankment instability. However, there is a soil failure in the upstream side of the embankment for particle sizes 0.2 and 0.15m. Additionally, there are differences in other failure parameters considered in this research, such as breach percent, and peak discharge.

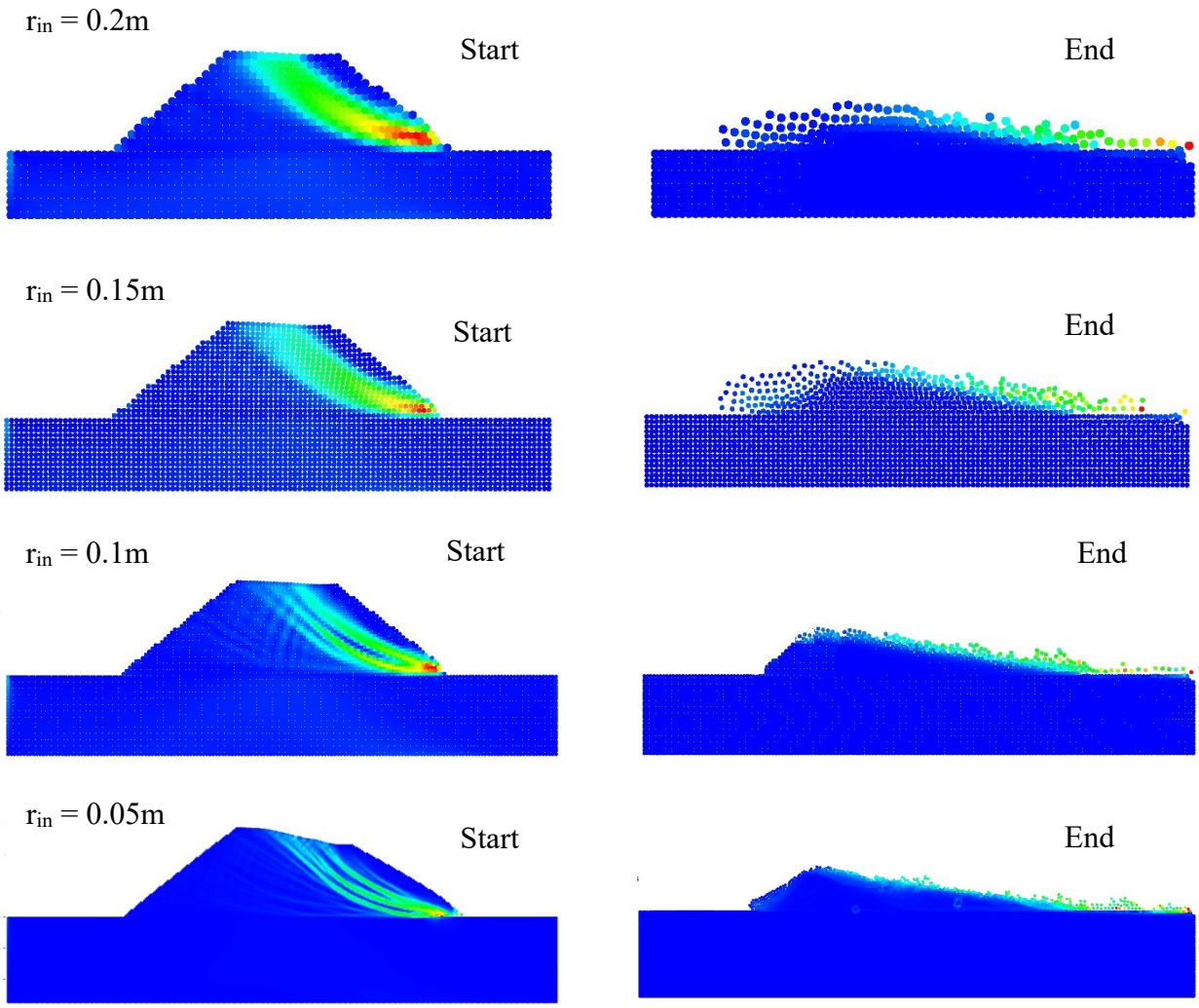

Figure 20: Failure mode for different particle sizes

Breach percent and initiation time, and peak discharge calculations are explained in sections 4.4.2 and 4.4.3, respectively. Breach initiation time in all the simulations is calculated to be 5 seconds (instant). Breach percent and peak discharge for each particle size simulation are depicted in Figure 21 and Figure 22, respectively. Breach percent and peak discharge are almost identical for 0.05m and 0.1m particle size (80% vs. 79%, and 1.55 vs. 1.512, respectively). Therefore, a particle size of 0.1m is considered for all other simulations performed in this study.

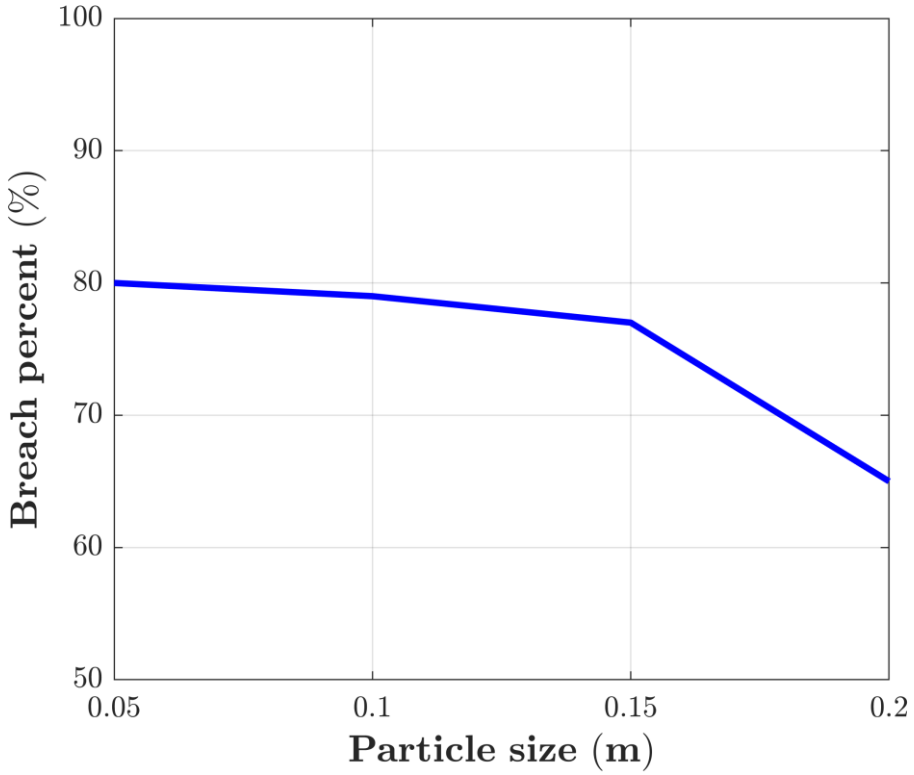

Figure 21: Breach percent vs. Particle size

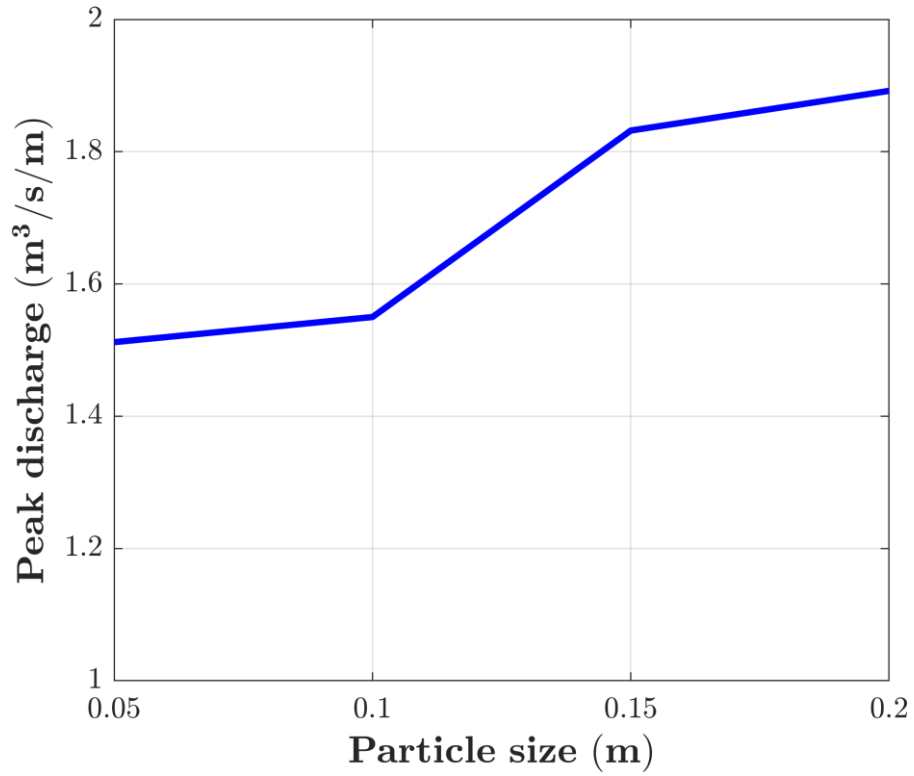

Figure 22: Peak discharge vs. Particle size

4.4 Post Processing

Many studies were performed to investigate dam failure. In most of these studies, empirical formulae were developed to predict failure parameters, such as; failure mode, breach shape, breach height and width, breach formation time, and peak discharge. In this research, the ANN approach is used to predict the behavior of earthen embankments during an overtopping event. For all the 240 performed simulations, the following parameters are studied; fail mode, breach percent, and peak discharge.

4.4.1 Fail modes

One of the shortcomings found in the literature is the study of dam overtopping. It is generally categorized as the mode of failure. Additionally, only the erosion progression of the embankment body is studied. However, water flow over the embankment can cause other problems to the dam structure. In this study, embankment failure, as well as foundation failure, is studied. Fail modes are classified into two categories; embankment failure and foundation failure. Two embankment fail modes are identified; Embankment erosion and instability. And three foundation fail modes are identified; Foundation erosion, piping, and bearing capacity failure. In the following sections, a sample of each failure mode is shown. All the simulations fail modes are reported in APPENDIX D.

4.4.1.1 Embankment erosion

This failure mode is characterized as the initiation of embankment erosion process and its progression over time. In this failure mode, shown in Figure 23, the downstream part of the embankment experiences a concentration of stresses, seen at $t = 20\ s$. After that, the water begins to erode the soil of the surface, $t = 30\ s$, of the downstream part of the embankment until the whole embankment is eroded.

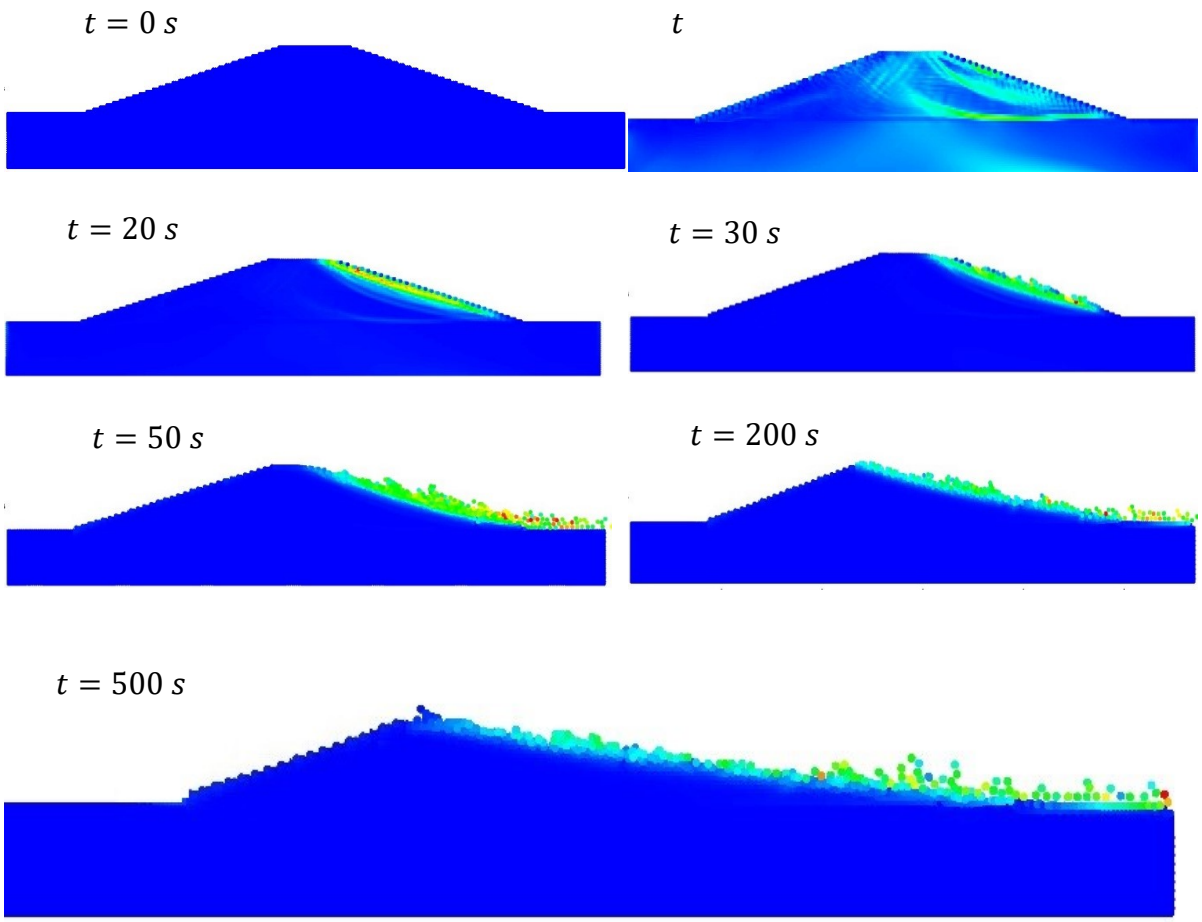

Figure 23: Total deviatoric strain progression during dam erosion.

This mode of failure mainly occurs when the embankment consists of clayey sand soil and less steep slopes and lower heights. This failure mode usually presents with embankment instability, since it is the only present mode by itself in only five simulations. However, in many other cases, there is a potential for erosion. But since the simulation is only for 500 seconds, it doesn't evolve into full failure within the simulated time.

4.4.1.2 Embankment instability

In this failure mode, the stresses exceed the design capacity of the embankment. Which is caused by the extreme water level. As seen in Figure 24, the failure starts from the downstream slope toe and progressed back to reach the embankment crest $t < 20\ s$. After that, the failed soil portion starts to erode due to the water flow $t > 180\ s$.

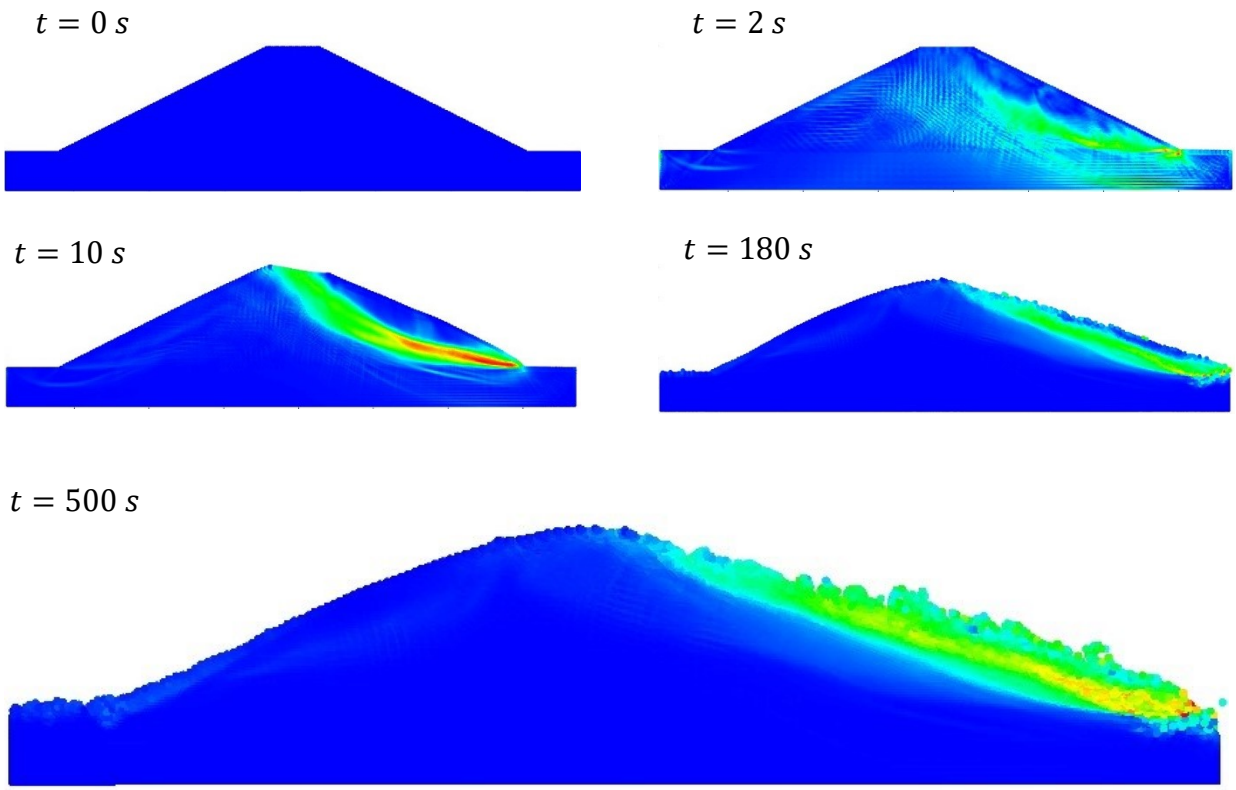

Figure 24: Total deviatoric strain progression during dam instability failure.

This mode of failure happens when the embankment is made of silty gravel soil regardless of the dam geometry and foundation soil. Additionally, this mode of failure occurs if the embankment is made of clayey sand with steeper embankment slope or higher embankments.

4.4.1.3 Foundation erosion

In this failure mode, the dam is not eroded. However, the water flow over the dam causes the foundation to erode near the toe of the embankment. This is caused by the stress concentration due to water colliding with the soil. This erosion eventually will cause the embankment to become unstable and fail, as shown in Figure 25.

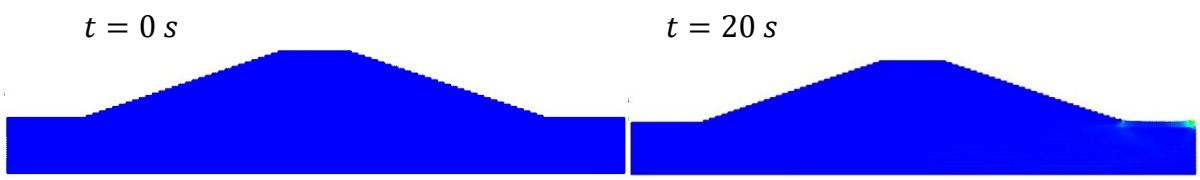

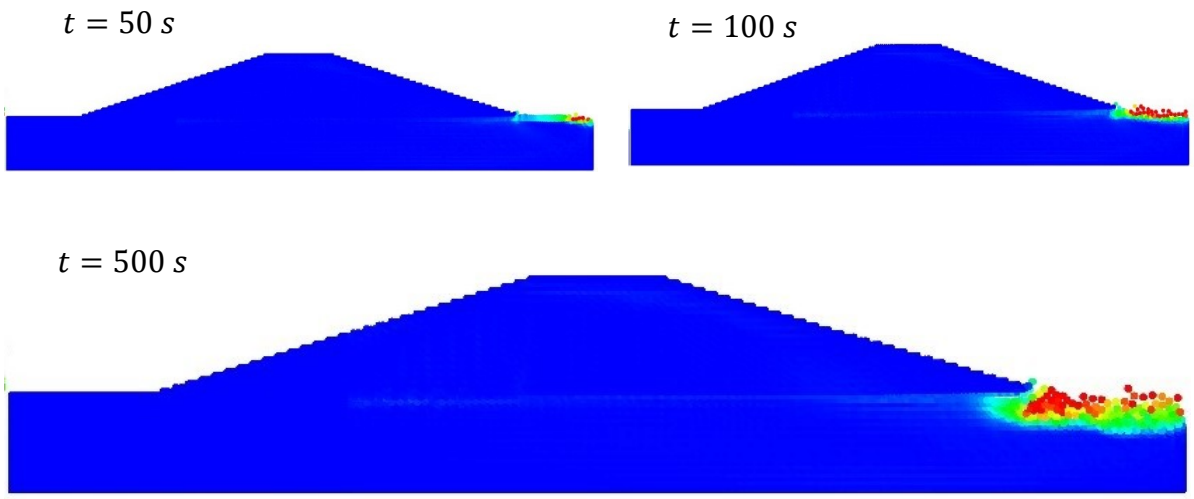

Figure 25: Total deviatoric strain progression during foundation erosion.

This failure mode arises when the foundation soil is silty gravel and less steep embankment slopes. Moreover, there is a potential of foundation erosion if the foundation soil is low plasticity silt, which could increase with time.

4.4.1.4 Piping

In this mode of failure, the hydraulic gradient at the embankment toe is enough to deform the soil and create piping conditions. Figure 26 depicts the progression of piping failure over time. In the beginning, $t < 180\ s$, the strain forms a channel for the seepage flow to increase. After that, the soil starts to deform more and eroded by the overtopping water.

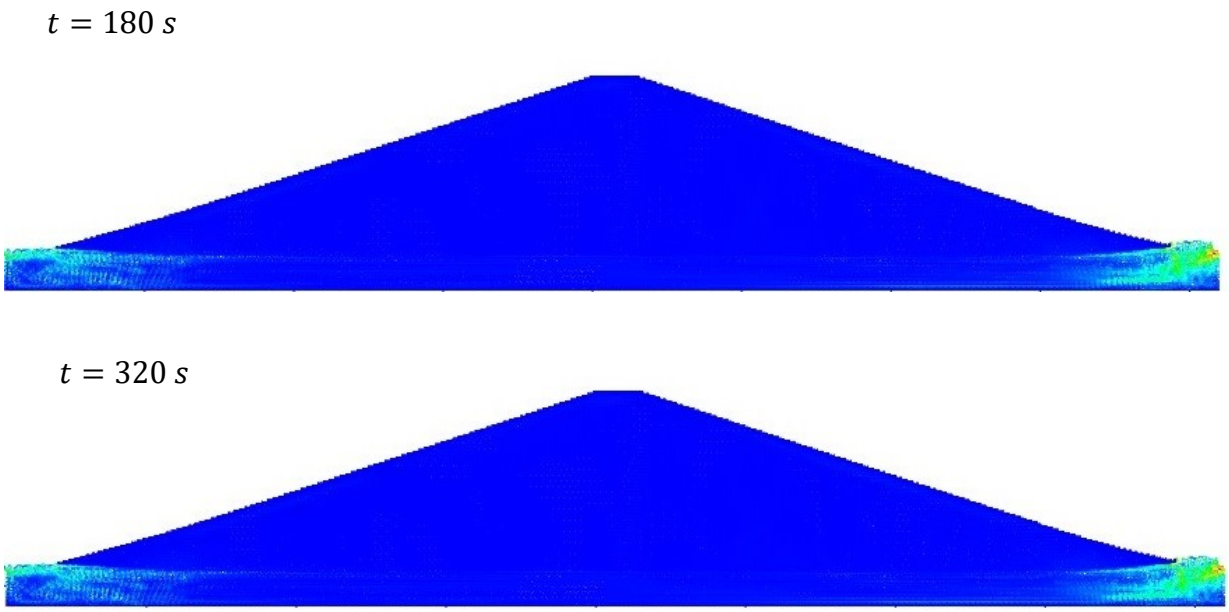

Figure 26: Total deviatoric strain progression during piping failure

This mode failure mainly happens when the foundation consists of well-graded gravel regardless of embankment soil or geometry. In some cases, piping failure occurs alongside embankment instability failure if the embankment is made of silty gravel or clayey sand.

4.4.1.5 Bearing capacity slide

In this failure mode, the foundation soil is overloaded by the dam and water beyond its bearing capacity, which causes a shear band to form and cause foundation slide. As depicted in Figure 27, the deviatoric shear strain is concentrated underneath the downstream slope of the dam, $t = 5\ s$. Then a shear band starts to form, $t = 190\ s$, which creates a slipping surface for the embankment and the foundation. Finally, this failure triggers a sliding of structure, which eventually leads to embankment breaching.

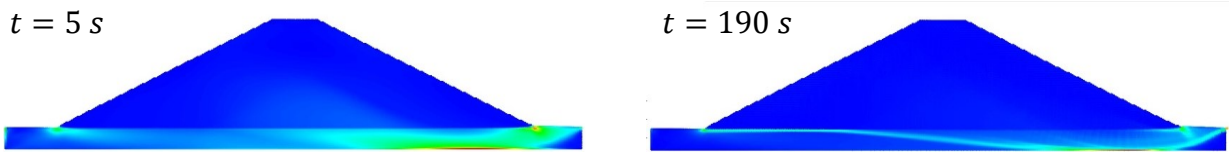

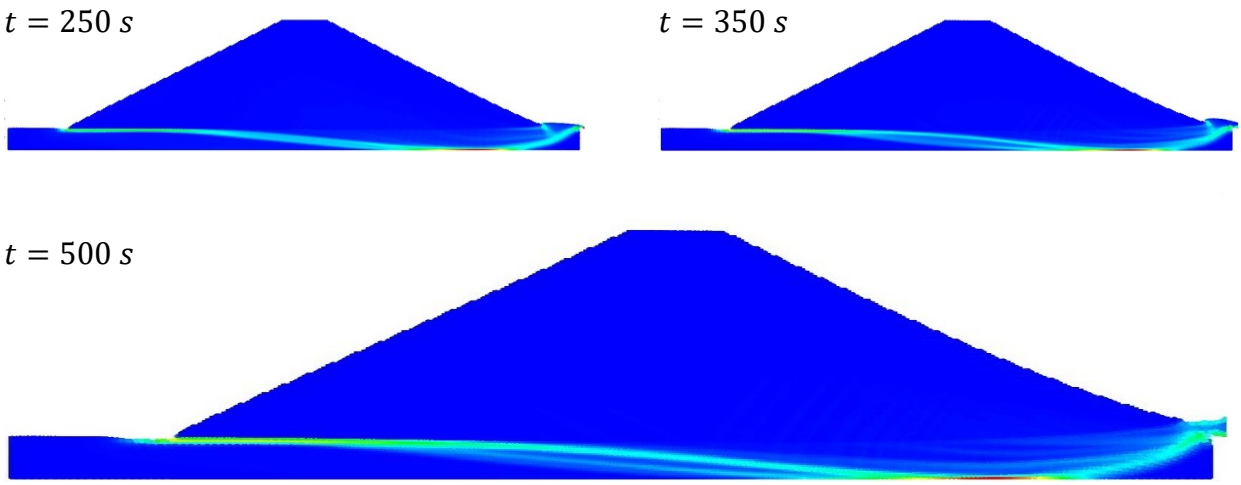

Figure 27: Total deviatoric strain progression during bearing capacity slide failure

This failure mode mainly happens with high embankment elevations and steep slopes. The probability of breaching (i.e., embankment instability) increases when the foundation is made of high plasticity clay or clayey gravel.

4.4.1.6 Failure index

In many cases, failure didn't evolve to cause breaching during the simulated time. To account for this progress, a failure index is defined for all the failure modes discussed before. Where the index is given a value of 1 when the failure is fully formed, and 0 when no failure is observed.

The value of the failure index depends on the failure progress during the simulated time. In some cases, the strain is increasing over time, it will eventually lead to failure, as depicted in Figure 28. Depending on how far the failure has progressed, the failure value is increased. These cases are given a failure index larger than 0.5.

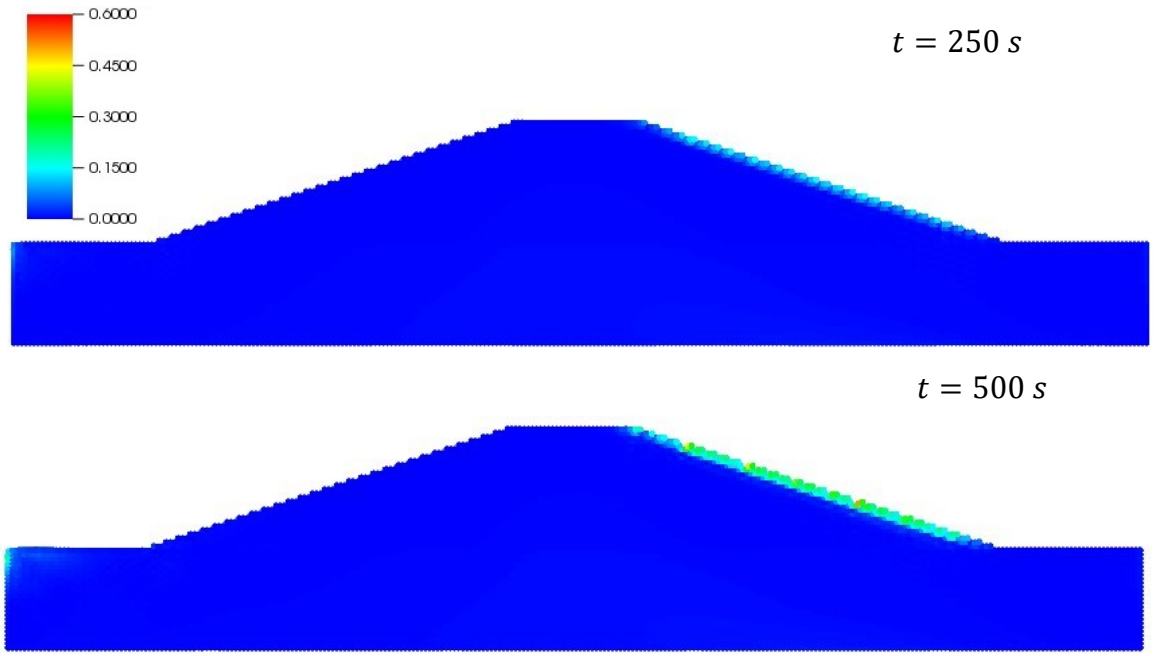

Figure 28: Total deviatoric shear strain for potential embankment erosion failure

In other cases, little to no increase in the deviatoric shear strain is observed. In this case, the failure index is given a value lower than 0.5. Figure 29 shows an example case for a possible foundation erosion. In this case, foundation erosion is possible if the overtopping event continues for an extended period of time. The failure index value increases with the increase of the total deviatoric shear strain.

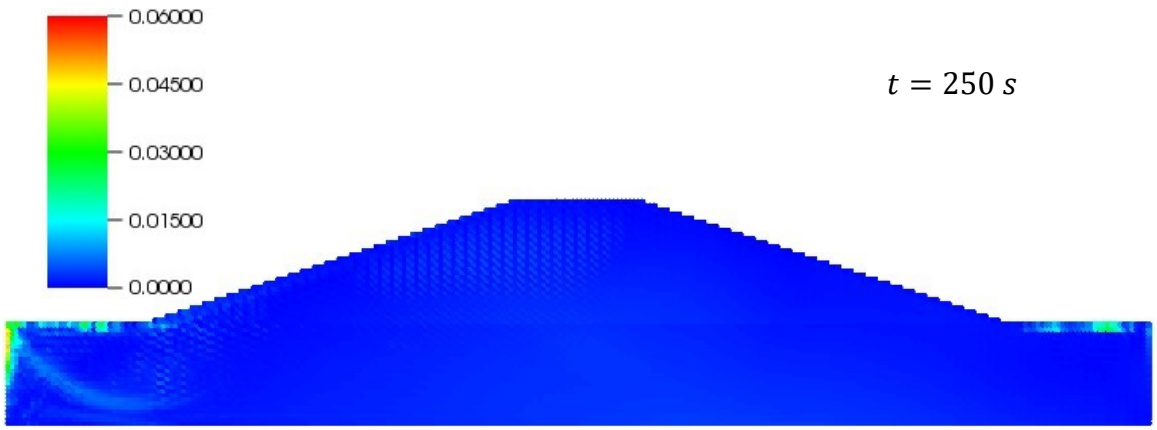

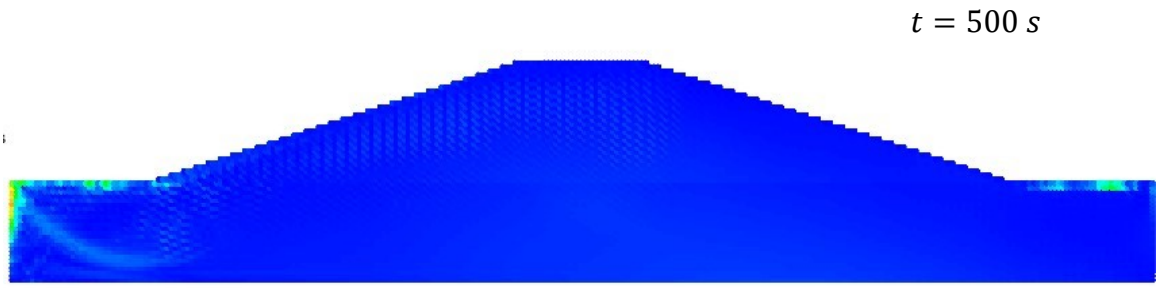

Figure 29: Total deviatoric shear strain for possible foundation erosion

4.4.2 Breach percentage

Generally, the breach formation time is measured from the start of the overtopping event until the embankment is completely eroded (Franca and Almeida 2004; Morris et al. 2018). Since the simulation takes a long time to perform, the embankment height is recorded over the time of the simulations (500 s) as shown in Figure 30. The breach percentage at the end of the simulation is calculated by dividing the embankment height at the end of the simulation by its original height. Additionally, the breach initiation time is also recorded, marked by the red circle in Figure 30. All the simulations' breach percent, initiation time, and peak discharge are reported in APPENDIX D.

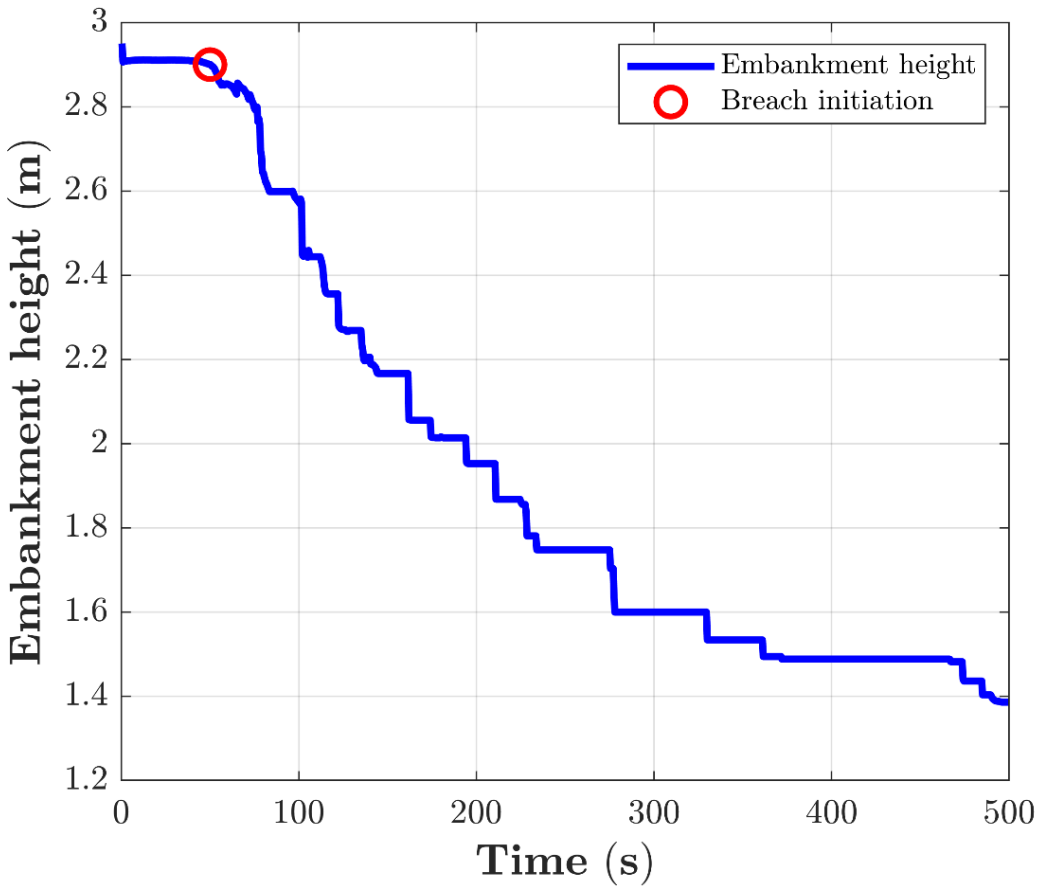

Figure 30: Embankment height over time

4.4.3 Peak discharge

To calculate the peak discharge, the average velocity of the particles leaving the model domain is recorded as well as the depth of water exiting the model. The discharge is calculated using equation (56). Since a two-dimensional simulation is performed, the discharge is calculated per meter width.

$$Q = V \times A \tag{56}$$

Where: Q: Discharge ($m^3/s/m$)

V: Average velocity (m/s)

A: Discharge area (m^2/m)

Figure 31 illustrates the discharge over time. Since the discharge fluctuates significantly, a moving average is applied with a window of 5 seconds. The peak discharge is obtained from the moving average curve.

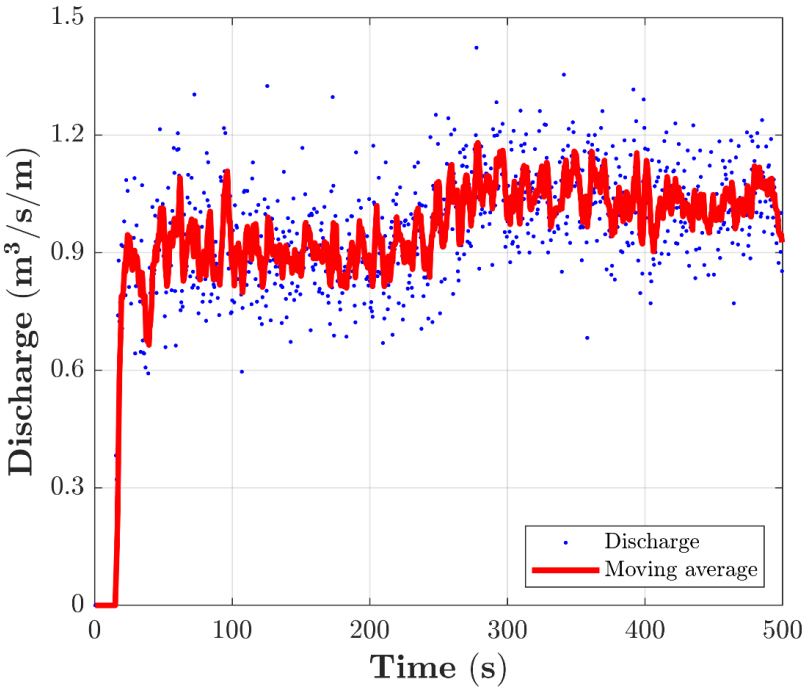

Figure 31: Water discharge over time

4.4.4 Foundation erosion

The maximum depth of failed foundation soil on the downstream side is recorded at the end of the simulation. This failure can be due to any of the foundation failure modes; erosion, piping, or bearing capacity slide. Regardless of the failure mode, the maximum depth of the failed foundation soil is documented.

4.5 Database preparation

In this research, a total of 240 simulations are performed. Each simulation requires 14 parameters to define the model correctly. Two parameters are needed to define the embankment geometry; embankment side slope and height. The model is divided into two sections; embankment and foundation. 6 parameters are required to define each soil section; density (φ), Cohesion (c), Angle of friction (φ), Modulus of elasticity (E), Porosity (n), and effective diameter (D_{15}).

Moreover, failure modes are assigned a generalized failure embankment or foundation failure. After that, each generalized failure is classified into the failure modes discussed in section 4.4.1. Additionally, the maximum discharge, breach percent, breach initiation time, and foundation erosion are calculated for each simulation, as explained in sections 4.4.2 to 4.4.4. This brings the total number of outputs to 11 outputs.

A total of 240 simulations are performed. Each simulation has 14 inputs and 11 outputs. The database is divided into 150 datasets for training, 60 datasets for testing, and 30 for validation. The maximum number of hidden nodes is set to 7 hidden nodes, calculated using equation (8). Each output is modeled in a separate ANN model except the classification of foundation failure, which produced better results when combined in one model.

4.6 ANN Optimization

Each output is modeled in a separate ANN model except the classification of foundation failure, which produced better results when combined in one model. In some models, the prediction of previously developed ANN models is utilized as inputs to enhance the prediction of the model. In other models, not all the inputs are used which produced better model prediction accuracy than using all the inputs. The choice of the utilized inputs is based on the correlation factor

between the input and the output, shown in APPENDIX E. Each model is trained adaptively using the training algorithm discussed in section 2.4.

4.6.1 Failure Modes

4.6.1.1 General embankment failure

In this model, the general embankment failure index (GEF) is predicted as a function of all the inputs; embankment side slope (α) and height (H), embankment soil properties as well as foundation soil properties. After performing the training process discussed in section 2.4, the best performing model was obtained by adaptively starting at 6 hidden nodes and stopping at 6 hidden nodes and 200 iterations. Since the model performed worse on the testing and validation datasets, as shown in Table 7, the train-all model was utilized to capture the logic within the testing and validation datasets and not included in the training datasets.

Table 7: Training, testing, validation, and train all statistics for the general embankment failure index (GEF) prediction model.

Training		Testing		Validation		Train All	
R^2	ASE	R^2	ASE	R^2	ASE	R^2	ASE
0.902	0.01510	0.912	0.01319	0.821	0.03564	0.916	0.01363

The train-all model produced an excellent representation of the embankment instability failure index. Accordingly, the final ANN model can be represented, as shown in equation (57).

$$GEF = ANN_{14\text{-}[6\text{-}6\text{-}200]\text{-}1}[\alpha, H, \rho_e, C_e, \varphi_e, E_e, n_e, D_{15e}, \rho_f, C_f, \varphi_f, E_f, n_f, D_{15f}] \quad (57)$$

Where: 14-[6-6-200]-1: 14: is the number of input variables [α is side slope degrees, H is embankment height in meters, ρ is density in kg/m^3, C is cohesion in kPa, φ is angle of friction in degrees, E is modulus of elasticity in MPa, n is porosity, and D_{15} is effective diameter in meters, subscript e refers to embankment property and f refers to foundation property, 6-6-200 represents the starting hidden node and the final hidden node and corresponding iterations. Lastly, 1 represents the number of output variables (GEF).

The connection weights and thresholds of the final network are shown in Table 8.

Table 8: Connection weights and thresholds (TS) of the generalized embankment failure (GEF) probability prediction model.

	HN1	HN2	HN3	HN4	HN5	HN6
α	-1.815	-1.732	-6.369	0.105	-3.896	-0.445
H	2.703	1.848	-4.793	0.192	4.591	-2.653
ρ_e	-0.578	-0.356	2.251	-0.455	3.235	1.396
C_e	-1.237	-0.777	1.146	0.506	2.347	-0.411
φ_e	0.162	-0.047	1.398	-0.951	-1.396	0.451
E_e	1.084	0.740	2.715	-0.286	-2.549	1.506
n_e	-0.153	-0.537	2.420	-0.653	-4.575	-1.235
D_{15e}	0.842	0.766	0.379	-0.241	-0.938	0.647
ρ_f	0.345	-0.213	-2.251	-0.701	-2.945	-0.777
C_f	-1.884	-1.101	2.239	-0.151	4.650	0.149
φ_f	-0.217	-0.450	-2.575	-0.237	-3.391	-0.561
E_f	-0.952	-0.270	1.161	0.892	-0.616	1.004
n_f	-0.869	-1.174	-0.379	-1.837	2.953	-1.615
D_{15f}	1.193	0.611	-1.401	0.136	-1.517	0.295
TS 1	-0.761	-0.614	-0.847	-0.090	0.426	-0.172

	HN1	HN2	HN3	HN4	HN5	HN6	TS 2
GEF	1.479	1.054	-5.699	-1.356	-4.342	-1.650	-8.965

4.6.1.2 Embankment instability

In this model, the embankment instability failure index (EIF) is predicted as a function of all the inputs; embankment side slope (α) and height (H), embankment soil properties, foundation soil properties, and the prediction from the GEF model developed earlier in section 4.6.1.1. After performing the training process discussed in section 2.4, the best performing model was obtained by adaptively starting at 1 hidden node and stopping at 2 hidden nodes and 400 iterations. Since the model performed worse on the testing and validation datasets, as shown in Table 9, the train-all model was utilized to capture the logic within the testing and validation datasets and not included in the training datasets.

Table 9: Training, testing, validation, and train all statistics for the embankment instability failure index (EIF) prediction model.

Training		Testing		Validation		Train All	
R^2	ASE	R^2	ASE	R^2	ASE	R^2	ASE
0.892	0.01796	0.923	0.01221	0.835	0.03210	0.908	0.01551

The train-all model produced an outstanding representation of the generalized embankment failure probability. Accordingly, the final ANN model can be represented as shown in equation (58).

$$\text{EIF} = \text{ANN}_{15\text{-}[1\text{-}2\text{-}400]\text{-}1}[\alpha, H, \rho_e, C_e, \varphi_e, E_e, n_e, D_{15e}, \rho_f, C_f, \varphi_f, E_f, n_f, D_{15f}, \text{GEF}] \quad (58)$$

Where: 15-[1-2-400]-1: 15: is the number of input variables [α is side slope degrees, H is embankment height in meters, ρ is density in kg/m^3, C is cohesion in kPa, φ is angle of friction in degrees, E is modulus of elasticity in MPa, n is porosity, and D_{15} is effective diameter in meters, subscript e refers to embankment property and f refers to foundation property, and GEF is the prediction of the generalized embankment failure model], 1-2-400 represents the starting hidden node and the final hidden node and corresponding iterations. Lastly, 1 represents the number of output variables (EIF).

4.6.1.3 Embankment erosion

In this model, the embankment erosion failure index (EEF) is predicted as a function of embankment height (H), embankment soil cohesion (C), angle of friction (φ), porosity (n), and effective diameter (D_{15}). And the prediction from the GEF, EIF models developed earlier in section 4.6.1.1 and section 4.6.1.2, respectively. As well as the forecast from the general foundation failure (GFF) developed in section 4.6.1.4. The best performing model was obtained by adaptively starting at 2 hidden nodes and stopping at 5 hidden nodes and 20,000 iterations. Since the model performed worse on the testing and validation datasets, as shown in Table 10, the train-all model was utilized to capture the logic within the testing and validation datasets and not included in the training datasets.

The coefficient of determination (R^2) for the validation is very low. This can be reasoned to the fact that embankment erosion has a value in only 5 validation datasets. The other validation datasets are zeros. This inconsistency of the coefficient of determinations is avoided when using ASE, which is the primary statistical measure utilized in determining the best model.

Table 10: Training, testing, validation, and train all statistics for the embankment erosion failure index (EEF) prediction model.

Training		Testing		Validation		Train All	
R^2	ASE	R^2	ASE	R^2	ASE	R^2	ASE
0.886	0.00624	0.651	0.00848	0.050	0.02121	0.862	0.00634

The train-all model produced a very good representation of the generalized embankment failure probability. Accordingly, the final ANN model can be represented, as shown in equation (59).

$$\text{EEF} = \text{ANN}_{\text{8-[1-2-400]-1}}[\text{H}, C_e, \varphi_e, n_e, D_{15e}, \text{GEF}, \text{EIF}, \text{GFF}] \quad (59)$$

Similarly: 8-[1-2-400]-1: 8: is the number of input variables [H is embankment height in meters, C is cohesion in kPa, φ is angle of friction in degrees, n is porosity, and D_{15} is effective diameter in meters, subscript e refers to embankment, and GEF, EIF, and GFF are the predictions of the generalized embankment failure, Embankment instability failure, and the generalized foundation failure models, respectively], 1-2-400 represents the starting hidden node and the final hidden node and corresponding iterations. Lastly, 1 represents the number of output variables (EEF).

4.6.1.4 General foundation failure

In this model, the general foundation failure index (GFF) is predicted as a function of all the inputs; embankment side slope (α) and height (H), embankment soil properties as well as foundation soil properties. After performing the training process discussed in section 2.4, the best performing model was obtained by adaptively starting at 5 hidden nodes and stopping at 6 hidden nodes and 600 iterations. The train-all model produced a very good representation of the generalized foundation failure index, as shown in Table 11. Accordingly, the final ANN model can be represented, as shown in equation (60).

Table 11: Training, testing, validation, and train all statistics for the general foundation failure index (GFF) prediction model.

Training		Testing		Validation		Train All	
R^2	ASE	R^2	ASE	R^2	ASE	R^2	ASE

0.954	0.007	0.721	0.04545	0.713	0.06109	0.933	0.01033

$$GFF = ANN_{14\text{-}[5\text{-}6\text{-}600]\text{-}1}[\alpha, H, \rho_e, C_e, \varphi_e, E_e, n_e, D_{15e}, \rho_f, C_f, \varphi_f, E_f, n_f, D_{15f}] \quad (60)$$

Where: 14-[5-6-600]-1: 14: is the number of input variables [α is side slope degrees, H is embankment height in meters, ρ is density in kg/m^3, C is cohesion in kPa, φ is angle of friction in degrees, E is modulus of elasticity in MPa, n is porosity, and D_{15} is effective diameter in meters, subscript e refers to embankment property and f refers to foundation property], 5-6-600 represents the starting hidden node and the final hidden node and corresponding iterations. Lastly, 1 represents the number of output variables (GFF).

4.6.1.5 Foundation failure classification

In this model, the foundation erosion failure index (FEF), foundation piping failure index (FPF), and foundation bearing capacity slide failure index (FBF) are predicted as a function of embankment side slope (α) and height (H), and foundation soil properties, in addition to generalized foundation failure index (GFF). The best performing model was obtained by adaptively starting at 5 hidden nodes and stopping at 6 hidden nodes and 11,100 iterations. The train-all model produced a good representation of the generalized foundation failure index, as shown in Table 12. Accordingly, the final ANN model can be represented, as shown in equation (61).

Table 12: Training, testing, validation, and train all statistics for FEF, FPF, and FBF prediction models.

	Training		Testing		Validation		Train All	
	R^2	ASE	R^2	ASE	R^2	ASE	R^2	ASE
FEF	0.876	0.00471	0.709	0.00583	0.985	0.00058	0.768	0.00735
FPF	0.977	0.00235	0.869	0.01695	0.993	0.00155	0.960	0.00487
FBF	0.824	0.01125	0.655	0.03939	0.767	0.01871	0.766	0.01767
Avg	0.893	0.00610	0.745	0.02072	0.915	0.00695	0.831	0.00996

$$[FEF, FPF, FBF] = ANN_{9\text{-}[5\text{-}6\text{-}11,100]\text{-}3}[\alpha, H, \rho_f, C_f, \varphi_f, E_f, n_f, D_{15f}, GFF] \quad (61)$$

Where: 9-[5-6-11,100]-1: 9: is the number of input variables [α is side slope degrees, H is embankment height in meters, ρ is density in kg/m^3, C is cohesion in kPa, φ is angle of friction

in degrees, E is modulus of elasticity in MPa, n is porosity, and D_{15} is effective diameter in meters, subscript f refers to foundation property, GFF is the prediction from the generalized foundation failure model], 5-6-11,100 represents the starting hidden node and the final hidden node and corresponding iterations. Lastly, 3 represents the number of output variables (FEF, FPF, FBF).

4.6.2 Breach percentage and initiation time

In this model, breach percent and initiation time are predicted as a function of embankment side slope (α) and height (H), and foundation soil properties, in addition to the prediction of the embankment instability failure (EIF) as well as the foundation piping failure model (FPF). Since failure didn't occur in all simulations, the inverse of the initiation time is taken. The dataset with no failure will have a value of zero (1/infinity). The best performing model was obtained by adaptively starting at 2 hidden nodes and stopping at 4 hidden nodes and 500 iterations. The train-all model produced a good representation of the generalized foundation failure index, as shown in Table 13(62). Accordingly, the final ANN model can be represented, as shown in equation (62).

Table 13: Training, testing, validation, and train all statistics for breach percent (BP) and initiation time (BIT) prediction model.

	Training		Testing		Validation		Train All	
	R^2	ASE	R^2	ASE	R^2	ASE	R^2	ASE
PB	0.954	0.00302	0.777	0.01569	0.373	0.07337	0.905	0.00726
BIT	0.761	0.00554	0.633	0.00835	0.562	0.01247	0.794	0.00495
Avg	0.858	0.00428	0.705	0.01202	0.468	0.04292	0.849	0.00611

$$[BP, BIT] = ANN_{16\text{-}[2\text{-}4\text{-}500]\text{-}2}[\alpha, H, \rho_e, C_e, \varphi_e, E_e, n_e, D_{15e}, \rho_f, C_f, \varphi_f, E_f, n_f, D_{15f}, EIF, FPF] \quad (62)$$

Where: 16-[2-4-500]-2: 16: is the number of input variables [α is side slope degrees, H is embankment height in meters, ρ is density in kg/m^3, C is cohesion in kPa, φ is angle of friction in degrees, E is modulus of elasticity in MPa, n is porosity, and D_{15} is effective diameter in meters, subscript e refers to embankment property and f refers to foundation property, EIF is

the prediction from the embankment instability failure model, and FPF is the prediction of foundation piping failure model], 2-4-500 represents the starting hidden node and the final hidden node and corresponding iterations. Lastly, 2 represents the number of output variables (BP, BIT).

4.6.3 Peak discharge

In this model, peak discharge (PD) is predicted as a function of all the inputs; embankment side slope (α) and height (H), embankment soil properties as well as foundation soil properties. The best performing model was obtained by adaptively starting at 3 hidden nodes and stopping at 3 hidden nodes and 100 iterations. The train-all model produced an excellent representation of peak discharge, as shown in Table 14. Accordingly, the final ANN model can be represented, as shown in equation (63).

Table 14: Training, testing, validation, and train all statistics for the peak discharge (PD) prediction model.

Training		Testing		Validation		Train All	
R^2	ASE	R^2	ASE	R^2	ASE	R^2	ASE
0.85	0.00316	0.926	0.00316	0.934	0.00241	0.883	0.00219

$$PD = ANN_{14\text{-}[3\text{-}3\text{-}100]\text{-}1}[\alpha, H, \rho_e, C_e, \varphi_e, E_e, n_e, D_{15e}, \rho_f, C_f, \varphi_f, E_f, n_f, D_{15f}] \quad (63)$$

Where: 14-[3-3-100]-1: 14: is the number of input variables [α is side slope degrees, H is embankment height in meters, ρ is density in kg/m^3, C is cohesion in kPa, φ is angle of friction in degrees, E is modulus of elasticity in MPa, n is porosity, and D_{15} is effective diameter in meters, subscript e refers to embankment property and f refers to foundation property], 3-3-100 represents the starting hidden node and the final hidden node and corresponding iterations. Lastly, 1 represents the number of output variables (PD) in m^3/s/m.

4.6.4 Foundation erosion

In this model, Foundation erosion (FE) is predicted as a function of the embankment side slope (α) and height (H), foundation soil properties, and the prediction from generalized foundation

failure (GFF). The best performing model was obtained by adaptively starting at 3 hidden nodes and stopping at 4 hidden nodes and 700 iterations. The train-all model produced a good representation of peak discharge, as shown in Table 15. Accordingly, the final ANN model can be represented, as shown in equation (64).

Table 15: Training, testing, validation, and train all statistics for the foundation erosion (FE) prediction model.

Training		Testing		Validation		Train All	
R^2	ASE	R^2	ASE	R^2	ASE	R^2	ASE
0.898	0.00597	0.742	0.02774	0.717	0.03347	0.783	0.01772

$$FE = ANN_{9\text{-}[3\text{-}4\text{-}700]\text{-}1}[\alpha, H, \rho_f, C_f, \varphi_f, E_f, n_f, D_{15f}, GFF] \quad (64)$$

Where: 9-[3-4-700]-1: 9: is the number of input variables [α is side slope degrees, H is embankment height in meters, ρ is density in kg/m^3, C is cohesion in kPa, φ is angle of friction in degrees, E is modulus of elasticity in MPa, n is porosity, and D_{15} is effective diameter in meters, subscript f refers to foundation property, GFF is the prediction from the generalized foundation failure model], 3-4-700 represents the starting hidden node and the final hidden node and corresponding iterations. Lastly, 1 represents the number of output variables (FE) in meters.

4.7 Post Validation

To further validate the developed models, two additional simulations are performed. These simulations were not included in the simulation database before. This will ensure that the developed models can predict the failure parameters for different scenarios.

In these simulations, the foundation is defined as high plasticity clay (CH) soil, and the embankment is defined as compacted clayey sand (SC). The modeling properties of these soils are shown in Table 16. The slope of the embankment is 1.5:1 (H:V). Finally, two different heights are considered 5m and 10m.

Table 16: Soil modeling properties for the post-validation simulations

	Density (kg/m3)	Cohesion (kPa)	Friction angle	Elastic modulus (MPa)	Porosity	Effective Diameter (m)
CH	1890	11	19	7	0.39	4.2E-04
SC	2150	11	31	20	0.15	1.0E-03

In the first problem (i.e., 5m embankment), definite embankment failure is predicted with general embankment failure index of 1. And values of 1 and 0.87 for the embankment erosion and instability failure indices, respectively. This result is consistent with numerical simulation shown in Figure 32. Embankment erosion starts to form at the beginning before the instability failure ($t = 60\ s$). After that, the embankment continues to failure while the embankment topsoil is eroding ($t > 350\ s$).

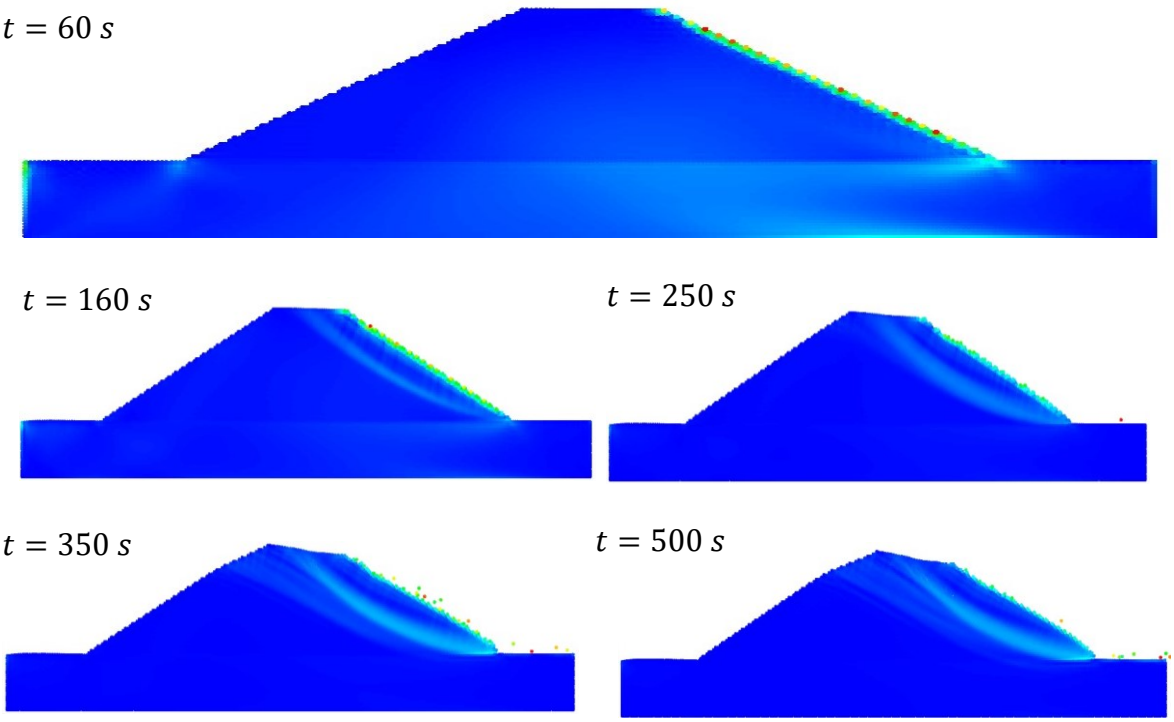

Figure 32: problem failure progression for the first post validation

Other failure parameters are shown in Table 17. Peak discharge and breach initiation time are underestimated. And the breach percent is overestimated by 2%. These predictions imply

embankment failure will start within the first minute of the overtopping event, and 12% breach will happen over the next 8 minutes.

Table 17: Failure parameters for first post validation problem, calculated vs. prediction.

	Peak discharge ($m^3/s/m$)	Foundation erosion (m)	Breach Percent (%)	Breach initiation time (s)
Calculated	1.823	0.0	10	51
Predicted	1.258	0.0	11.9	17.8

In the second problem (i.e., 10m embankment), definite embankment, as well as foundation failure, are predicted with general embankment and foundation failure indices of 1 and 0.98, respectively. The foundation failure is predicted to be a bearing capacity slide failure with a failure index of 1. And the embankment failure is predicted to be an instability failure with a failure index of 1 as well. The same failure modes occur during the numerical simulation, as shown in Figure 33. Bearing capacity failure starts to form at the beginning before the instability failure ($t = 10\ s$). After that b,oth failure modes progress to failure ($t > 180\ s$).

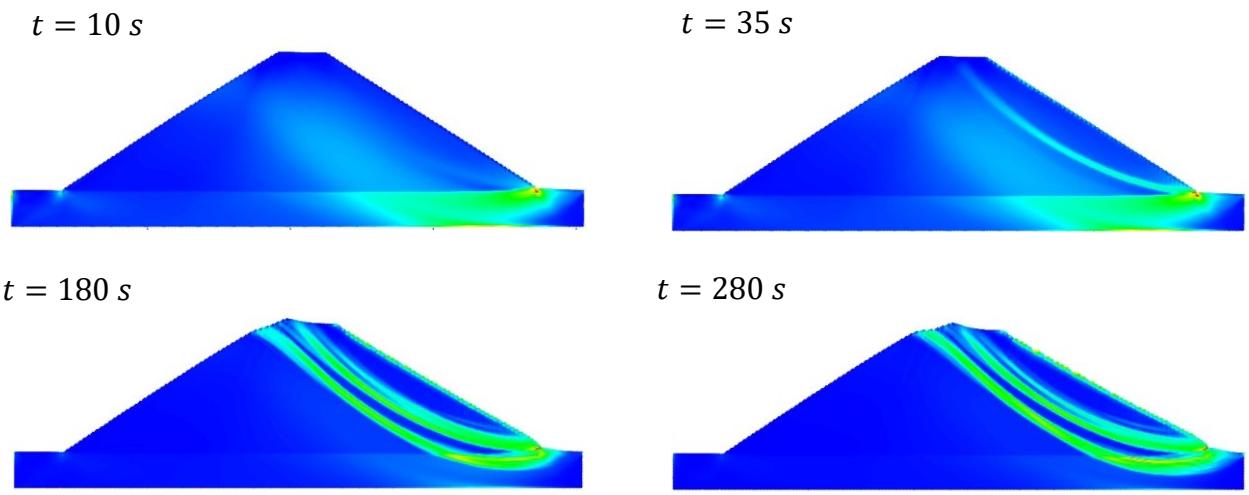

Figure 33: failure progression for second post validation problem

In this simulation, peak discharge and breach initiation time are also underestimated. And the breach percent is underestimated by 2% as depicted in Table 18. These predictions imply embankment and foundation failure will start within the first minute of the overtopping event, and 21% breach will happen over the next 8 minutes.

Table 18: Second post validation problem failure parameters, calculated vs. prediction.

	Peak discharge ($m^3/s/m$)	Foundation erosion (m)	Breach Percent (%)	Breach initiation time (s)
Calculated	1.691	0.4	23.9	29
Predicted	1.562	0.6	21.3	6.3

4.8 Graphical user interface (GUI)

In order for the results of this study more accessible for emergency planning or further research in a specific case study, a Graphical User interface is created utilizing all the developed ANN models. Excel is used to create the GUI since it is readily available on most computers and doesn't require unique software installation.

The GUI is comprised of 3 sheets; the first is an information sheet describing the interface and how to use it, and the ANN model statistics. The second sheet is the interface itself, shown in Figure 34. And finally, the third sheet is a calculation sheet.

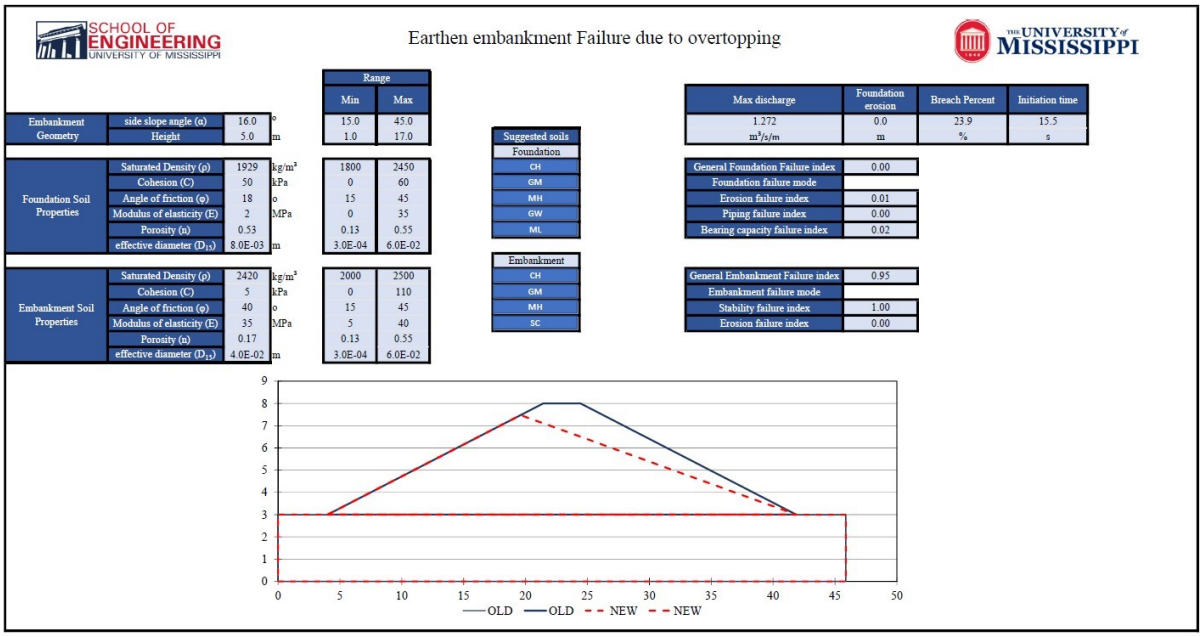

Figure 34: Embankment failure due to overtopping graphical user interface (GUI)

The user inputs are the geometry of the embankment, embankment soil properties, and the foundation soil properties, shown in Figure 35. The confidence range for each input is displayed next to it. Additionally, the soils utilized in the numerical simulations are listed as suggested soils for the foundation and the embankment. The user can click on the soil name, and its properties will automatically be filled.

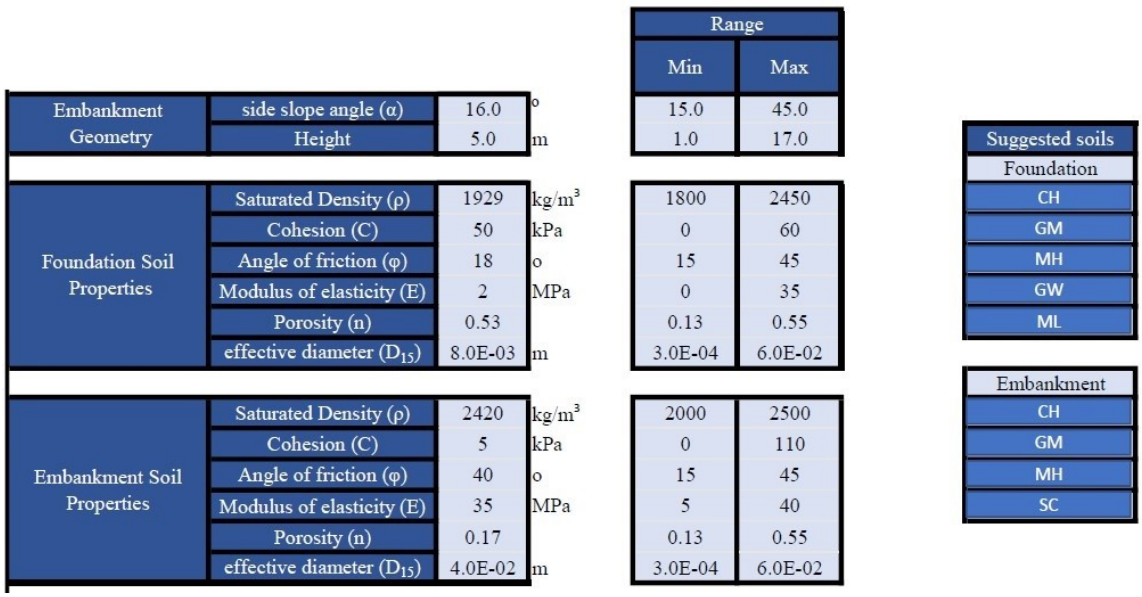

Figure 35: Embankment failure GUI inputs

The outputs of all the models developed in this study are the failure mode for the embankment and the foundation and their classification, peak discharge, breach percent and foundation erosion at the end of the simulation (after 500s), and breach initiation time. As shown in Figure 36.

Max discharge	Foundation erosion	Breach Percent	Initiation time
1.272	0.0	23.9	15.5
$m^3/s/m$	m	%	s

General Foundation Failure index	0.00
Foundation failure mode	
Erosion failure index	0.01
Piping failure index	0.00
Bearing capacity failure index	0.02

General Embankment Failure index	0.95
Embankment failure mode	
Stability failure index	1.00
Erosion failure index	0.00

Figure 36: Embankment failure GUI outputs

Finally, the results are visually represented compared to the initial conditions, as depicted in Figure 37.

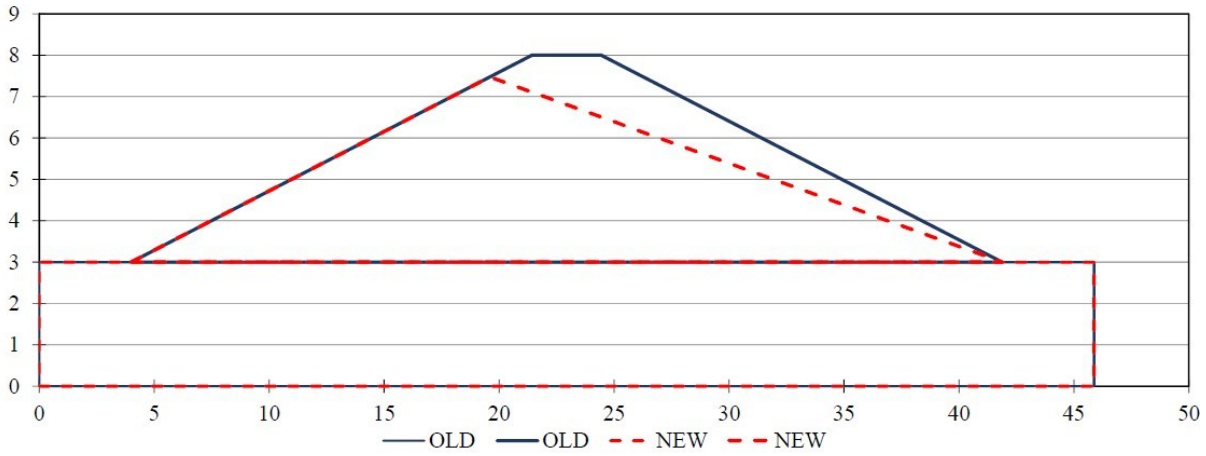

Figure 37: Embankment failure prediction visual representation

4.9 Conclusions

In this study, the post-failure behavior of earthen embankments was numerically simulated utilizing an open source code smoothed particle hydrodynamics (SPH) code "PersianSPH." The software was successfully validated by modeling experiments from literature focusing on soil failure and soil-water interaction.

- The numerical model input parameters were identified as embankment slope and height, embankment soil properties, and foundation soil properties.
- Embankments with slope varying from 1.2-3:1 (H:V) and height ranging between (3-15m). Instead of changing each soil property individually, five different soils were considered for the foundation and four soil types for the embankment.
- A total of 240 simulations were performed; each simulation was performed for 500 seconds.
- Five different failure modes were identified; Embankment erosion and instability, and foundation erosion, piping, and bearing capacity failure.
- Embankment erosion presented in low height and low slope embankment and the embankment is made of clayey sand soil.
- Embankment instability failure occurred in clayey gravel embankments and silty sand embankments with steeper slopes or higher embankments.
- Foundation erosion arose for silty gravel foundations and low embankments, a potential foundation erosion was observed for low plasticity silt foundations.
- Foundation piping failure occurred when the foundation is made of well-graded gravel.
- Foundation bearing capacity slide failure was observed for steeper and higher embankments.
- Peak discharge, foundation erosion, breach percent at the end of the simulation, and breach initiation time are identified as failure parameters.

- Eight ANN models were developed to correlate the numerical simulation inputs and the identified failure parameters.
- Each failure parameter was modeled independently except; foundation failure, and breach percent and initiation time.
- The developed ANN models showed good to excellent correlation to the numerical simulations results with R^2 ranging from 0.768 – 0.960.
- Two additional simulations were performed to validate the ANN models. These simulations were not included in the original database.
- The developed ANN models were utilized to create a GUI to predict the behavior of earthen embankment during an overtopping event.

5. CONCLUSIONS AND RECOMMENDATIONS

5.1 Conclusions

Artificial Neural Network (ANN) technique is utilized in this research to analyze and optimize two engineering problems; ***characterizing the stress-strain behavior of graphene nanocomposites*** and ***predicting earthen embankment failure due to overtopping***. The first problem is an experimental study, and the second application is based on numerical data. In both cases, ANN was employed to overcome the complexity of the problem and predict the behavior of the studied engineering system with high accuracy. The developed ANN models can be reliably and efficiently utilized by engineers and save time, money, and effort. Here is a summary of the most important conclusions of this dissertation, more detailed conclusions of each study are given in their respective chapters.

In the first application, the mechanical properties of PEIGNP composites are studied, including the toughness, maximum tangent modulus, maximum strength, and strain. ANN approach was utilized to overcome the inhomogeneous behavior of the material.

- Two ANN models were developed; the first was a strain-controlled model, and the other was a stress-controlled model.
- Another ANN model was developed and incorporated to predict the maximum strain at a given wt.%.
- Both stress- and strain-controlled models display excellent agreement with the experimentally observed data.
- The strain-controlled model tends to predict lower values for the mechanical properties, while the stress-controlled model tends to predict higher values.

- The strain-controlled model was noted to be more reliable in predicting the stress-strain behavior at different wt.% which is consistent with its higher statistical accuracy measures.
- By employing the developed ANN stress- and strain-controlled models, the stress-strain response can be efficiently simulated at any given wt.%.
- The developed ANN models are utilized to create a GUI to aid in future material design.

In the second problem, the post-failure behavior of earthen embankments was numerically simulated utilizing a smoothed particle hydrodynamics (SPH) code "PersianSPH".

- 14 input parameters for the numerical model input parameters were identified; including embankment slope and height, 6 parameters to model embankment soil, and an additional 6 parameters to accurately define the foundation soil.
- A total of 240 simulations were performed; each simulation was performed for 500 seconds.
- Embankments with slope varying from 1.2-3:1 (H:V) and height ranging between (3-15m). Five different soils were considered for the foundation and four soil types for the embankment.
- Five unique failure modes were identified; Embankment erosion and instability, and foundation erosion, piping, and bearing capacity failure.
- Peak discharge, foundation erosion, breach percent at the end of the simulation, and breach initiation time were identified as failure parameters.
- A total of eight ANN models were developed to predict earthen embankments during an overtopping event.
- The developed ANN models showed good to excellent correlation to the numerical simulations results with R^2 ranging from 0.768 – 0.960.
- Two other numerical simulations were performed and validated the ANN models.

- The developed ANN models were utilized to create a GUI to predict the behavior of earthen embankment during an overtopping event.

5.2 Recommendations

- This study of embankment overtopping failure is the first step in a long and much more detailed research. This includes considering more variation of physical, engineering, and other modeling parameters.
- The overtopping numerical model needs to be validated experimentally.
- The GUI is created to save time and effort. However, the applicable range for each parameter should be considered.
- Real soil parameters should be used in predicting failure of earthen embankments. Since soil parameters are interrelated.
- The developed ANN models are retrainable in case of future database expansion.

BIBLIOGRAPHY

Alhasan, Z., Jandora, J., and Říha, J. (2015). "Study of dam-break due to overtopping of four small dams in the Czech Republic." Acta Universitatis Agriculturae et Silviculturae Mendelianae Brunensis, 63(3), 717–729.

Armaghani, D. J., Hedayat, A., Murlidhar, B. R., Gordan, B., Koopialipoor, M., and Mohamad, E. T. (2019). "The use of new intelligent techniques in designing retaining walls." Engineering with Computers, Springer London, 0(0), 1–12.

ASDSO. (2015). "Association of State Dam Safety Officials, Vital Statistics."

Baldo, N., Manthos, E., and Pasetto, M. (2018). "Analysis of the Mechanical Behaviour of Asphalt Concretes Using Artificial Neural Networks." Advances in Civil Engineering, 2018, 1–17.

Bui, D. K., Nguyen, T., Chou, J. S., Nguyen-Xuan, H., and Ngo, T. D. (2018). "A modified firefly algorithm-artificial neural network expert system for predicting compressive and tensile strength of high-performance concrete." Construction and Building Materials, Elsevier Ltd, 180, 320–333.

Bui, H. H., and Fukagawa, R. (2013). "An improved SPH method for saturated soils and its application to investigate the mechanisms of embankment failure: Case of hydrostatic pore-water pressure." International Journal for Numerical and Analytical Methods in Geomechanics, 37, 31–50.

Bui, H. H., Fukagawa, R., and Sako, K. (2006). "Smoothed particle hydrodynamics for soil mechanics." Numerical Methods in Geotechnical Engineering.

Bui, H. H., Fukagawa, R., Sako, K., and Ohno, S. (2008a). "Lagrangian meshfree particles method (SPH) for large deformation and failure flows of geomaterial using elastic–plastic soil

constitutive model." International Journal for Numerical and Analytical Methods inGeomechanics, 32(March 2007), 189–213.

Bui, H. H., Fukagawa, R., Sako, K., and Wells, J. C. (2008b). "{SPH}-Based Numerical Simulations for Large Deformation of Geomaterial Considering Soil-Structure Interaction." The 12th International Conference of International Association for Computer sMethods and Advances in Geomechanics (IACMAG), 1, 570–578.

Bui, H. H., Sako, K., and Fukagawa, R. (2007). "Numerical simulation of soil-water interaction using smoothed particle hydrodynamics (SPH) method." Journal of Terramechanics, 44(5), 339–346.

Chen, J. H., Jang, C., Xiao, S., Ishigami, M., and Fuhrer, M. (2008). "Intrinsic and extrinsic performance limits of graphene devices on SiO2." nature nanotechnology, 3, 206–209.

Dong, P., and Zhang, K. (1999). "Two-phase flow modelling of sediment motions in oscillatory sheet flow." Coastal Engineering, 36(2), 87–109.

Franca, M. J., and Almeida, A. B. (2004). "A computational model of rockfill dam breaching caused by overtopping (RoDaB)." Journal of Hydraulic Research, 42(2), 197–206.

Froehlich, D. C. (2008). "Embankment dam breach parameters and their uncertainties." Journal of Hydraulic Engineering, 134(12), 1708–1721.

Froehlich, D. C. (2016). "Empirical model of embankment dam breaching." International Conference on Fluvial Hydraulics (River Flow 2016), 1821–1826.

Gangi Setti, S., and Rao, R. N. (2014). "Artificial neural network approach for prediction of stress-strain curve of near β titanium alloy." Rare Metals, 33(3), 249–257.

García-Alba, J., Arcena, J. F. B., Ugarteburu, C., and Es García, A. (2019). "Artificial neural networks as emulators of process-based models to analyse bathing water quality in estuaries." Water Research, 150, 283–295.

Gee, D. M. (2009). “Comparison of Dam Breach Parameter Estimators.” World Environmental and Water Resources Congress, 1–10.

Gingold, R. A., and Monaghan, J. J. (1977). “Smoothed particle hydrodynamics: theory and application to non-spherical stars.” Monthly notices of the royal astronomical society, 181(3), 375–389.

Gray, J. P., Monaghan, J. J., and Swift, R. P. (2001). “SPH elastic dynamics.” Computer Methods in Applied Mechanics and Engineering, North-Holland, 190(49–50), 6641–6662.

Jiajie, L., Yan, W., Yi, H., Ma, Y., Zunfeng, L., Jinming, C., Chendong, Z., Hongjun, G., and Yongsheng, C. (2009). “Electromagnetic interference shielding of graphene/epoxy composites.” Carbon, 47(3), 922–925.

Koopialipoor, M., Fahimifar, A., Ghaleini, E. N., Momenzadeh, M., and Armaghani, D. J. (2019). “Development of a new hybrid ANN for solving a geotechnical problem related to tunnel boring machine performance.” Engineering with Computers, Springer London, 0(0), 1–13.

Korzani, G. M. (2015). “Persian SPH.”

Korzani, G. M., Galindo-Torres, S. A., Scheuermann, A., and Williams, D. J. (2018a). “SPH approach for simulating hydro-mechanical processes with large deformations and variable permeabilities.” Acta Geotechnica, Springer Berlin Heidelberg, 13(2), 303–316.

Korzani, G. M., Galindo-Torres, S. A., Scheuermann, A., and Williams, D. J. (2018b). “Smoothed Particle Hydrodynamics for investigating hydraulic and mechanical behaviour of an embankment under action of flooding and overburden loads.” Computers and Geotechnics, Elsevier Ltd, 94, 31–45.

Korzani, G. M., Galindo-Torres, S. A., Scheuermann, A., Williams, D. J., Korzani, G. M., Galindo-Torres, S. A., Scheuermann, A., and Williams, D. J. (2017). “Parametric study on

smoothed particle hydrodynamics for accurate determination of drag coefficient for a circular cylinder." Water Science and Engineering, Elsevier Ltd, 10(2), 143–153.

Korzani, G. M., Scheuermann, A., and Williams, D. J. (2018c). "A novel approach in sph to simulate scouring of an erodible bed." Computer and Fluids.

Lahiri, D., Das, S., Choi, W., and Arvind Agarwal. (2012). "Unfolding the damping behavior of multilayer graphene membrane in the low-frequency regime." ACS Nano, 6(5), 3992–4000.

Larese, A., Morán, R., Toledo, M. Á., Oñate, E., Campos, H., and Rossi, R. (2013). "Numerical and Experimental Study of Overtopping and Failure of Rockfill Dams." International Journal of Geomechanics, 15(4), 04014060.

Li, M., Pan, S., and O'Connor, B. A. (2008). "A two-phase numerical model for sediment transport prediction under oscillatory sheet flows." Coastal Engineering, Elsevier B.V., 55(12), 1159–1173.

Li, X., Manasrah, A., Al-Ostaz, A., Alkhateb, H., Lincoln, D., Rushing, G., and Cheng, A. H.-D. (2015). "Preparation and Characterization of High Content Graphene Nanoplatelet-Polyetherimide Paper." Journal of Nanoscience and Nanoengineering, 1(4), 252–258.

McCulloch, W. S., and Pitts, W. (1943). "A logical calculus of the ideas immanent in nervous activity." The bulletin of mathematical biophysics, 5(4), 115–133.

Monaghan, J. J. (1994). "Simulating free surface flows with SPH." Journal of computational physics, 110(4), 399–406.

Monaghan, J. J., and Pongracic, H. (1985). "Artificial viscosity for particle methods." Applied Numerical Mathematics, North-Holland, 1(3), 187–194.

Morris, M., West, M., and Hassan, M. (2018). "A Guide to Breach Prediction." Dams and Reservoirs, 28(4), 150–152.

Najjar, Y. M., and Huang, C. (2007). "Simulating the stress-strain behavior of Georgia kaolin via recurrent neuronet approach." Computers and Geotechnics, 34(5), 346–361.

Pham, T. M., and Hadi, M. N. S. (2014). “Predicting Stress and Strain of FRP-Confined Square/Rectangular Columns Using Artificial Neural Networks.” Journal of Composites for Construction, 18(6).

Rojas, R. (1996). Neural Networks: A Systematic Introduction.

Wang, C., Li, D., Too, C. O., and Wallace, G. G. (2009a). “Electrochemical Properties of Graphene Paper Electrodes Used in Lithium Batteries.” Chemistry of Materials, 21(13), 2604–2606.

Wang, D. D.-W., Li, F., Zhao, J., Ren, W., Chen, Z. Z.-G., Tan, J., Wu, Z.-S., Gentle, I., Lu, G. Q., and Cheng, H.-M. (2009b). “Fabrication of Graphene/Polyaniline Composite Paper via In Situ Anodic Electropolymerization for High-Performance Flexible Electrode.” ACS Nano, 3(7), 1745–1752.

Wu, H., and Drzal, L. T. (2012). “Graphene nanoplatelet paper as a light-weight composite with excellent electrical and thermal conductivity and good gas barrier properties.” Carbon, 50(3), 1135–1145.

Zhong, Q., Chen, S., and Deng, Z. (2018). “A simplified physically-based model for core dam overtopping breach.” Engineering Failure Analysis, Elsevier, 90, 141–155.

LIST OF APPENDICES

APPENDIX A

- PEI-xGnP nanocomposite experimental results

0 WT%

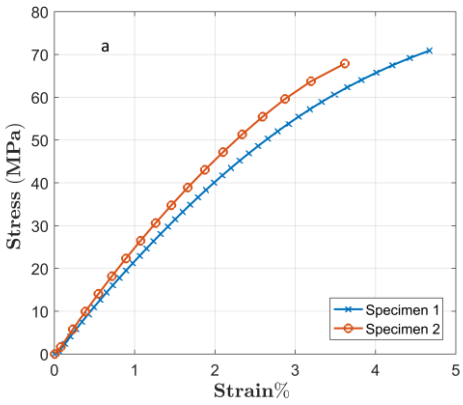

0.25 WT%

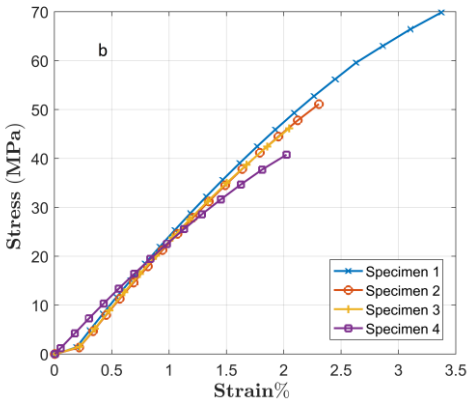

0.5 WT%

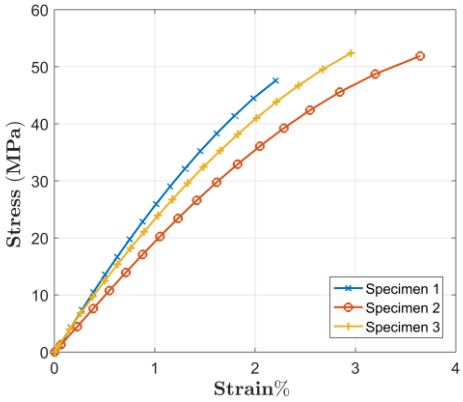

0.75 WT%

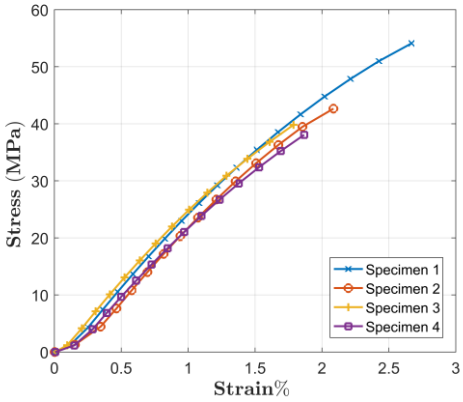

1 WT%

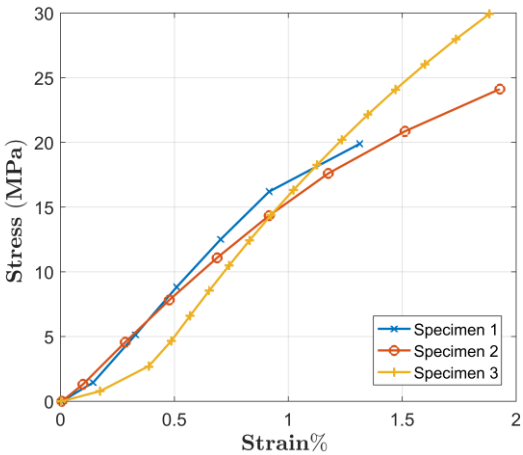

2.5 WT

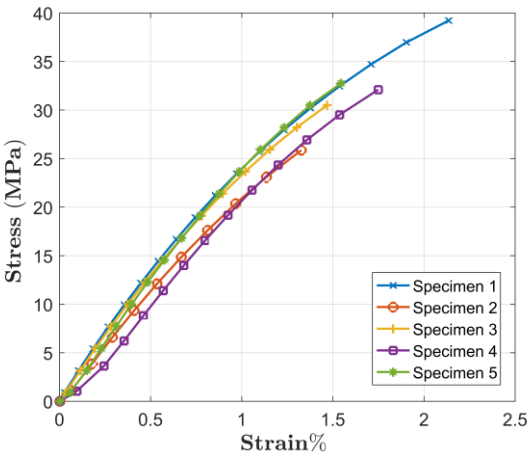

5 WT%

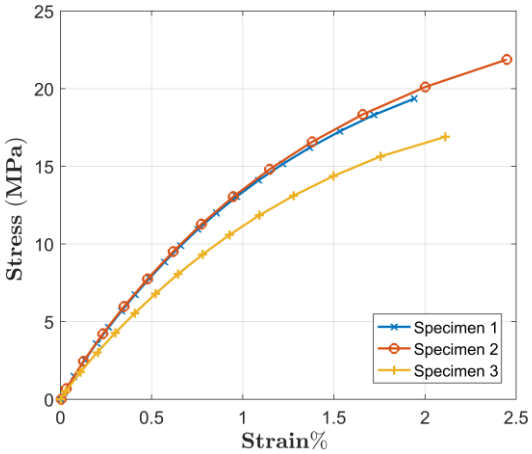

7.5 WT%

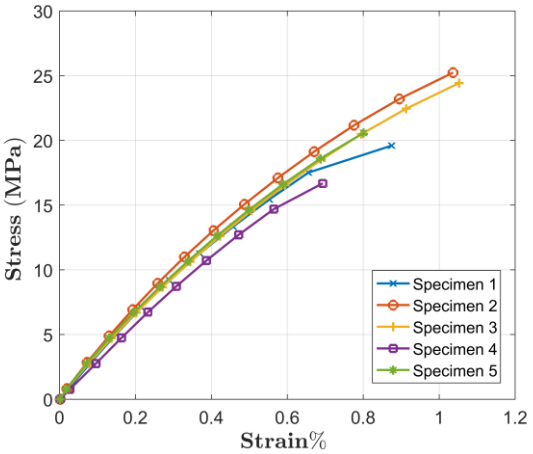

10 WT%

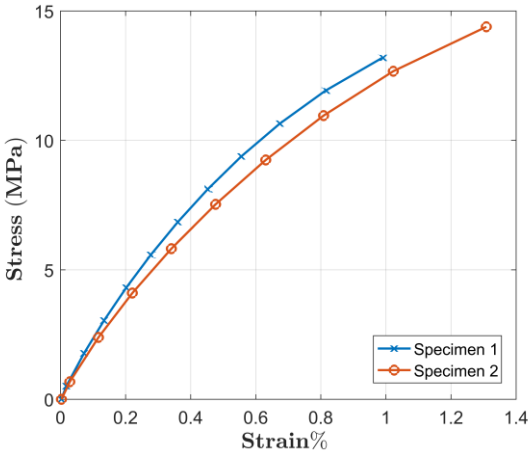

15 WT%

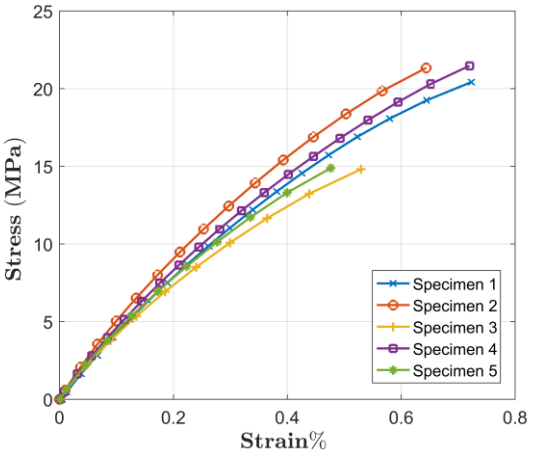

20 WT%

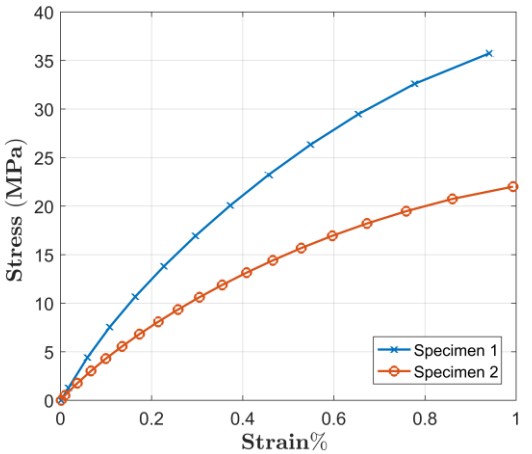

25 WT

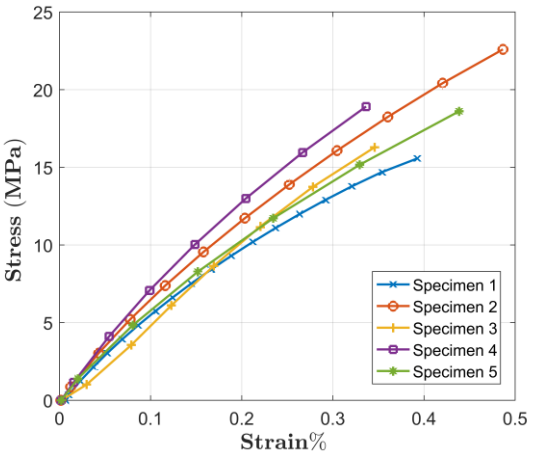

30 WT%

40 WT%

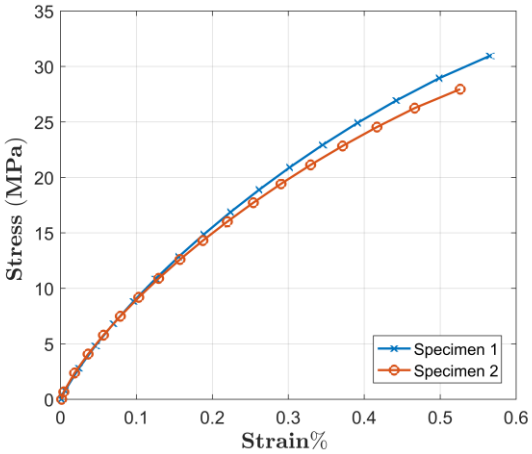

50 WT%

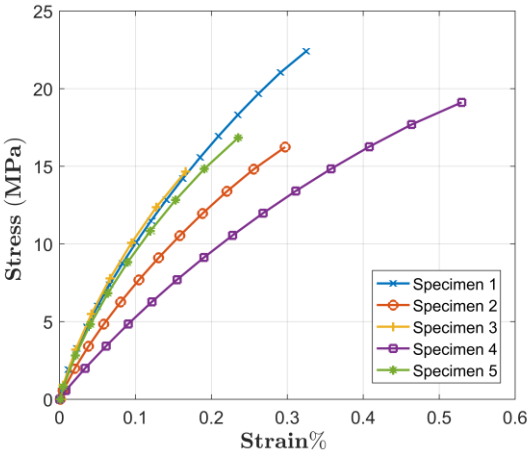

59 WT%

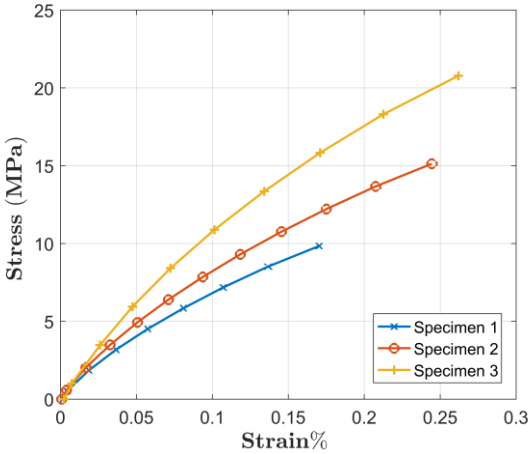

69 WT%

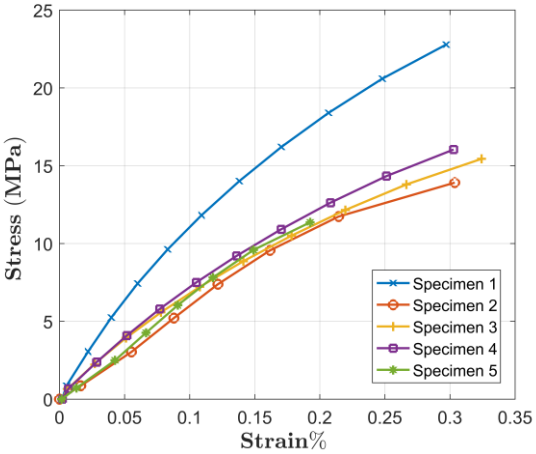

75 WT

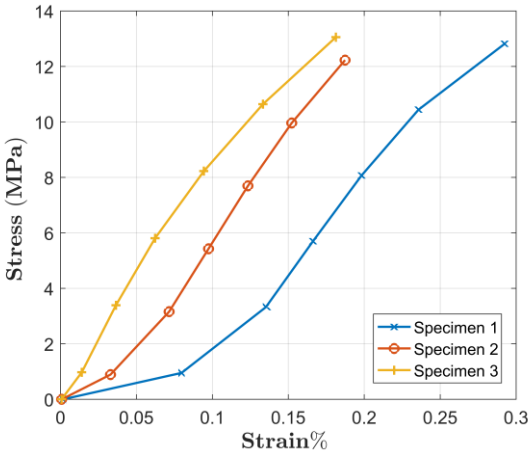

85 WT%

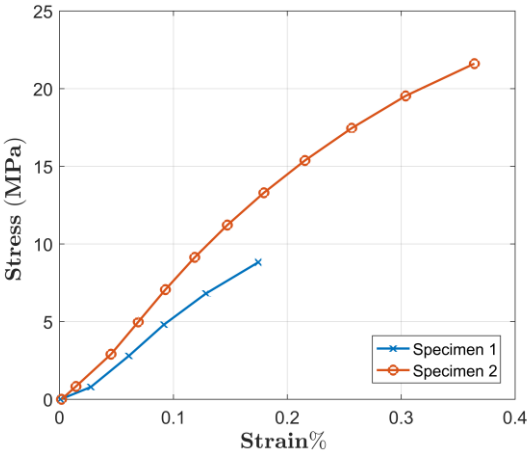

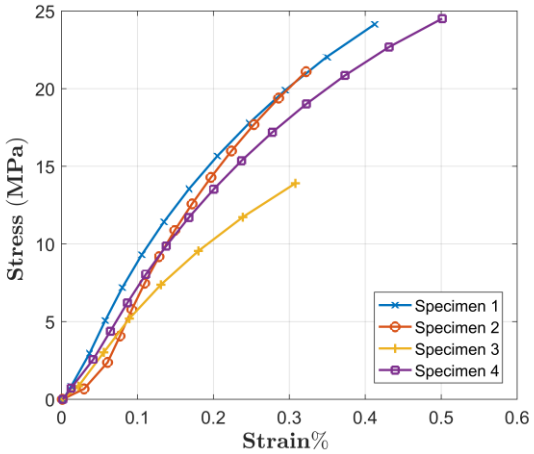
Stress (MPa)
Strain%
Specimen 1
Specimen 2
Specimen 3
Specimen 4

90.8 WT%

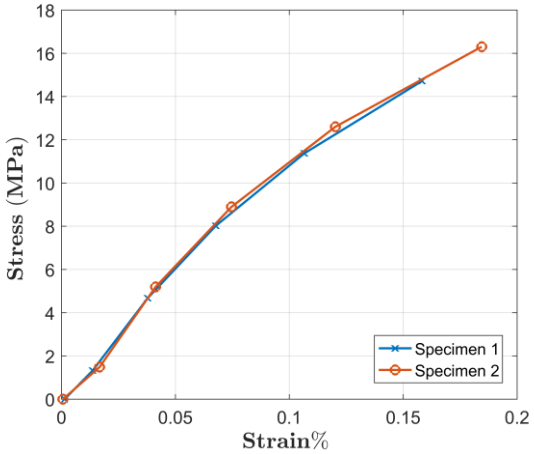
Stress (MPa)
Strain%
Specimen 1
Specimen 2

96.9 WT%

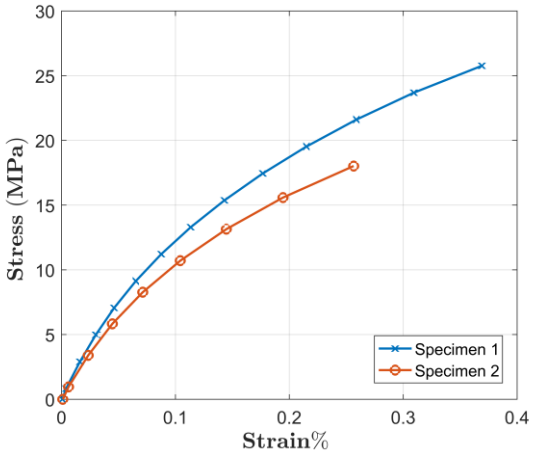
Stress (MPa)
Strain%
Specimen 1
Specimen 2

APPENDIX B

- PEI-xGnP ANN Simulations vs Experiments

0 WT%

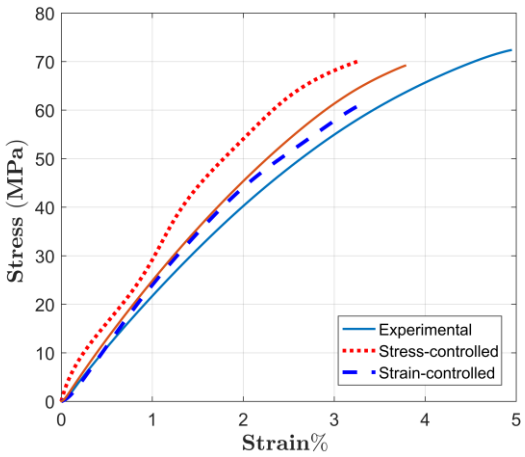

0.25 WT%

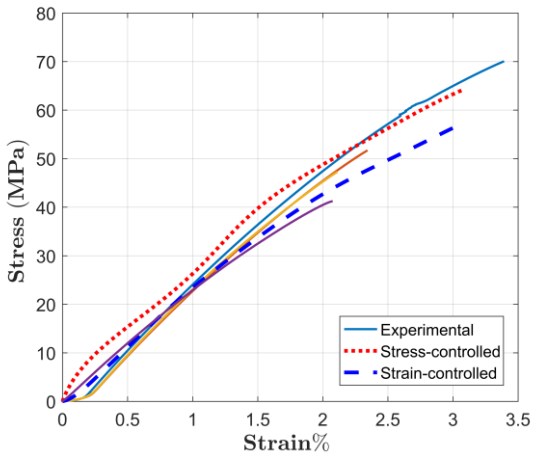

0.5 WT%

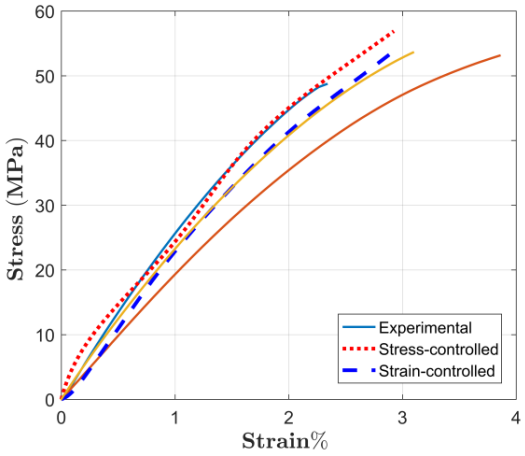

0.75 WT%

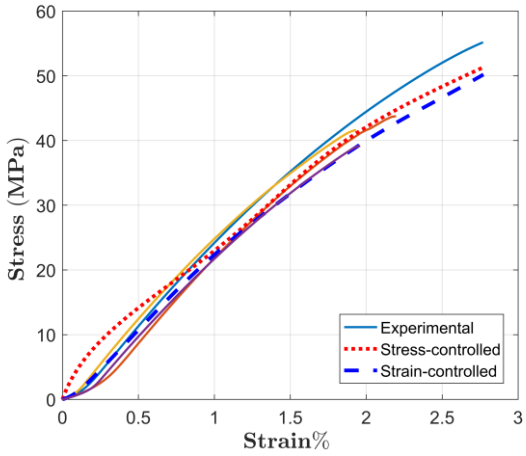

1 WT%

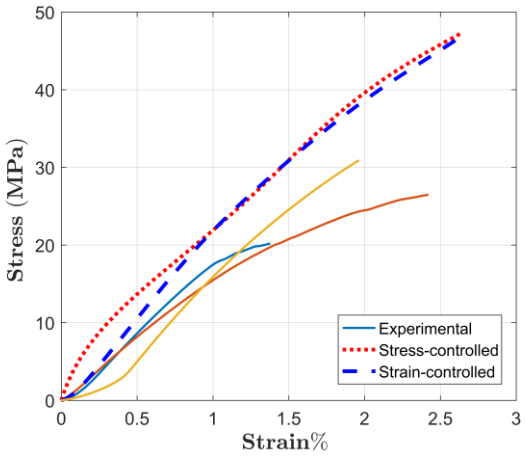

2.5 WT

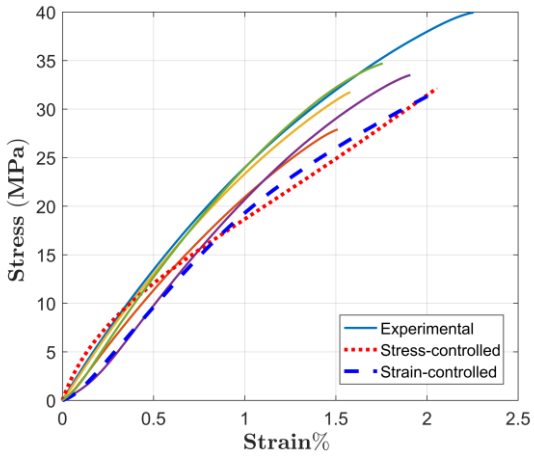

5 WT%

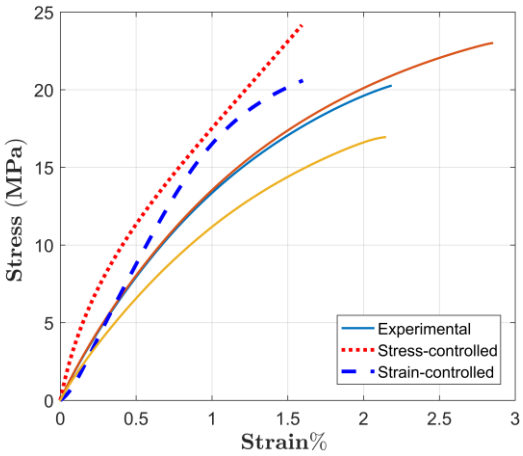

7.5 WT%

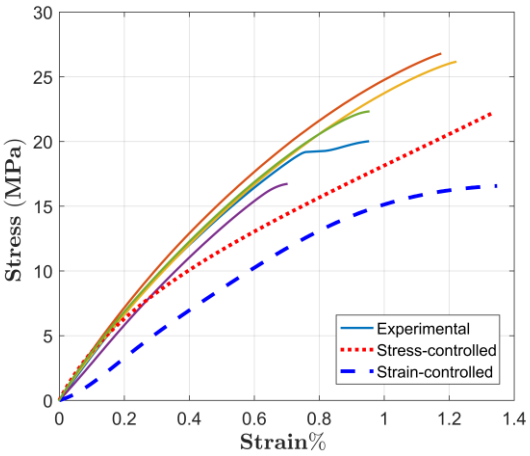

10 WT%

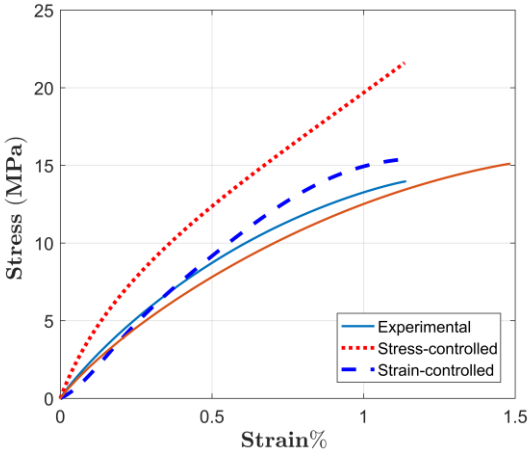

15 WT%

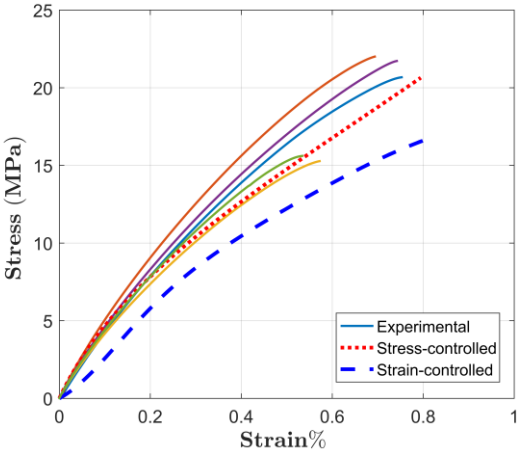

20 WT%

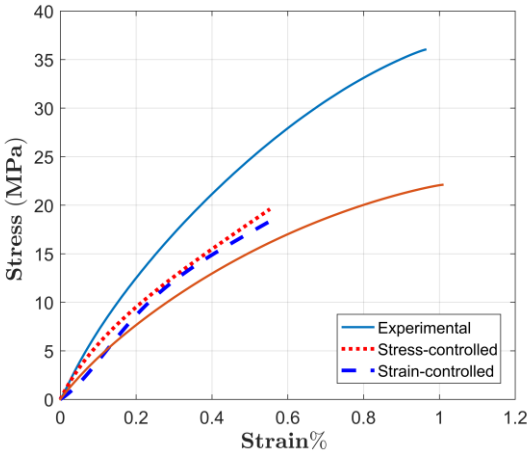

25 WT

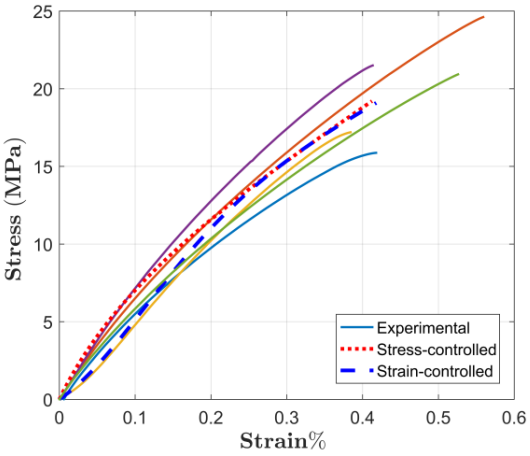

30 WT%

40 WT%

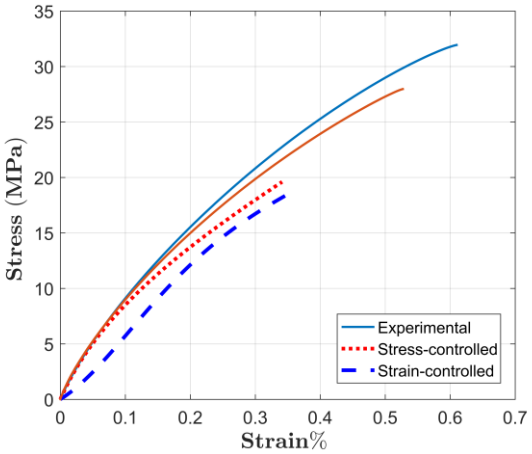

50 WT%

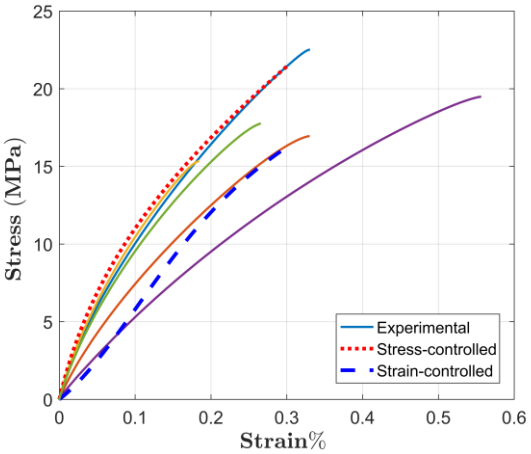

59 WT%

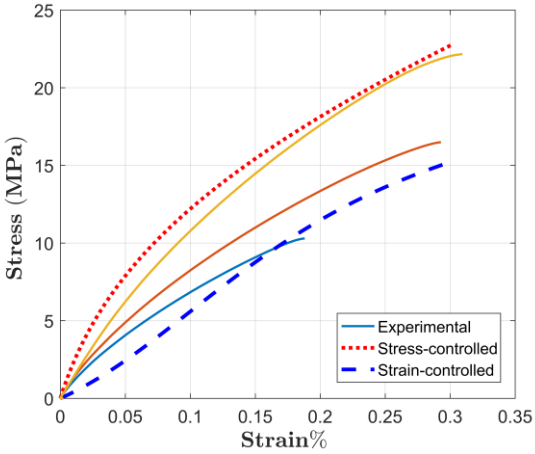

69 WT%

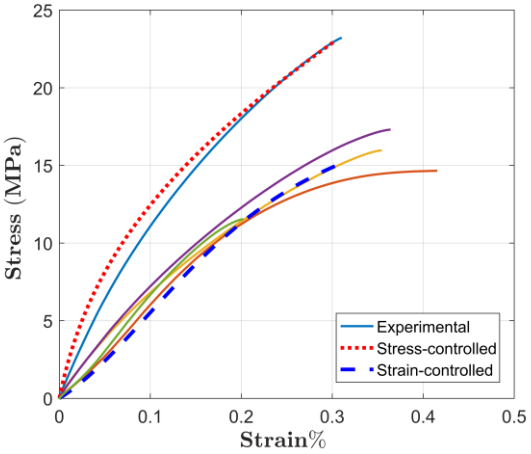

75 WT

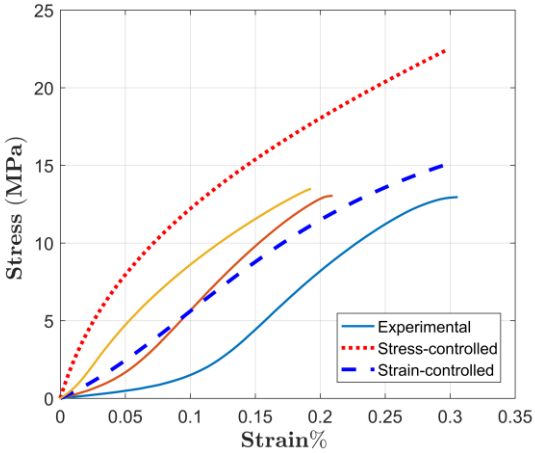

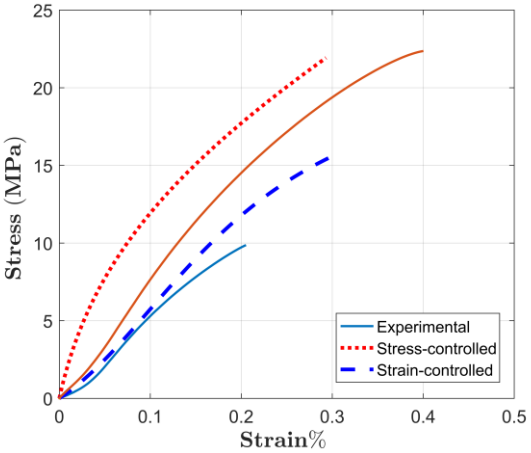

85 WT%

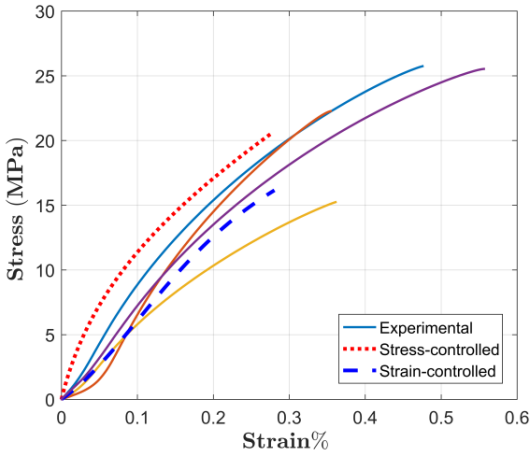
Stress (MPa)
Strain%
Experimental
Stress-controlled
Strain-controlled

90.8 WT%

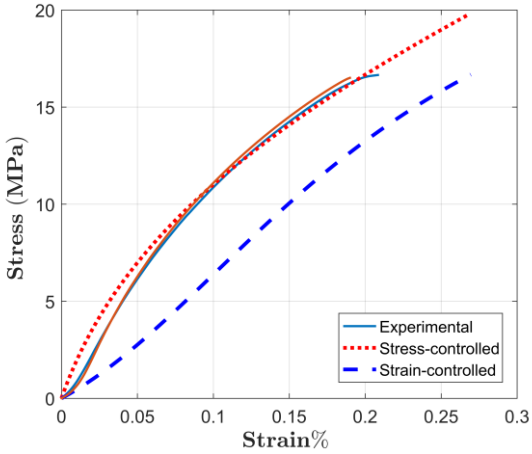
Stress (MPa)
Strain%
Experimental
Stress-controlled
Strain-controlled

96.9 WT%

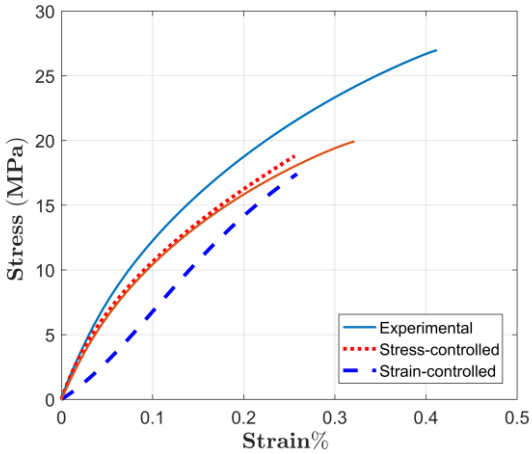
Stress (MPa)
Strain%
Experimental
Stress-controlled
Strain-controlled

APPENDIX C

- Dam failure: Modeling parameters of all the performed simulations

	Geom.		Foundation soil properties							Embankment soil properties						
#	α	H	Soil	ρ	C	Φ	E	n	d_{15}	Soil	ρ	C	Φ	E	n	d_{15}
1	18.43	3	CH	1889	11	19	7	0.39	4.2E-04	CH	2089	103	19	32	0.39	4.2E-04
2	18.43	3	CH	1889	11	19	7	0.39	4.2E-04	GM	2420	5	40	35	0.17	4.0E-02
3	18.43	3	CH	1889	11	19	7	0.39	4.2E-04	MH	2129	72	18	10	0.53	8.0E-03
4	18.43	3	CH	1889	11	19	7	0.39	4.2E-04	SC	2150	11	31	20	0.15	1.0E-03
5	18.43	3	GM	2320	0	34	20	0.17	4.0E-02	CH	2089	103	19	32	0.39	4.2E-04
6	18.43	3	GM	2320	0	34	20	0.17	4.0E-02	GM	2420	5	40	35	0.17	4.0E-02
7	18.43	3	GM	2320	0	34	20	0.17	4.0E-02	MH	2129	72	18	10	0.53	8.0E-03
8	18.43	3	GM	2320	0	34	20	0.17	4.0E-02	SC	2150	11	31	20	0.15	1.0E-03
9	18.43	3	MH	1929	50	18	2	0.53	8.0E-03	CH	2089	103	19	32	0.39	4.2E-04
10	18.43	3	MH	1929	50	18	2	0.53	8.0E-03	GM	2420	5	40	35	0.17	4.0E-02
11	18.43	3	MH	1929	50	18	2	0.53	8.0E-03	MH	2129	72	18	10	0.53	8.0E-03
12	18.43	3	MH	1929	50	18	2	0.53	8.0E-03	SC	2150	11	31	20	0.15	1.0E-03
13	18.43	3	GW	2369	0	40	30	0.27	5.0E-02	CH	2089	103	19	32	0.39	4.2E-04
14	18.43	3	GW	2369	0	40	30	0.27	5.0E-02	GM	2420	5	40	35	0.17	4.0E-02
15	18.43	3	GW	2369	0	40	30	0.27	5.0E-02	MH	2129	72	18	10	0.53	8.0E-03
16	18.43	3	GW	2369	0	40	30	0.27	5.0E-02	SC	2150	11	31	20	0.15	1.0E-03
17	18.43	3	ML	2219	22	27	15	0.42	8.0E-03	CH	2089	103	19	32	0.39	4.2E-04
18	18.43	3	ML	2219	22	27	15	0.42	8.0E-03	GM	2420	5	40	35	0.17	4.0E-02
19	18.43	3	ML	2219	22	27	15	0.42	8.0E-03	MH	2129	72	18	10	0.53	8.0E-03
20	18.43	3	ML	2219	22	27	15	0.42	8.0E-03	SC	2150	11	31	20	0.15	1.0E-03
21	18.43	7	CH	1889	11	19	7	0.39	4.2E-04	CH	2089	103	19	32	0.39	4.2E-04
22	18.43	7	CH	1889	11	19	7	0.39	4.2E-04	GM	2420	5	40	35	0.17	4.0E-02
23	18.43	7	CH	1889	11	19	7	0.39	4.2E-04	MH	2129	72	18	10	0.53	8.0E-03
24	18.43	7	CH	1889	11	19	7	0.39	4.2E-04	SC	2150	11	31	20	0.15	1.0E-03
25	18.43	7	GM	2320	0	34	20	0.17	4.0E-02	CH	2089	103	19	32	0.39	4.2E-04
26	18.43	7	GM	2320	0	34	20	0.17	4.0E-02	GM	2420	5	40	35	0.17	4.0E-02
27	18.43	7	GM	2320	0	34	20	0.17	4.0E-02	MH	2129	72	18	10	0.53	8.0E-03
28	18.43	7	GM	2320	0	34	20	0.17	4.0E-02	SC	2150	11	31	20	0.15	1.0E-03
29	18.43	7	MH	1929	50	18	2	0.53	8.0E-03	CH	2089	103	19	32	0.39	4.2E-04
30	18.43	7	MH	1929	50	18	2	0.53	8.0E-03	GM	2420	5	40	35	0.17	4.0E-02
31	18.43	7	MH	1929	50	18	2	0.53	8.0E-03	MH	2129	72	18	10	0.53	8.0E-03
32	18.43	7	MH	1929	50	18	2	0.53	8.0E-03	SC	2150	11	31	20	0.15	1.0E-03

33	18.43	7	GW	2369	0	40	30	0.27	5.0E-02	CH	2089	103	19	32	0.39	4.2E-04
34	18.43	7	GW	2369	0	40	30	0.27	5.0E-02	GM	2420	5	40	35	0.17	4.0E-02
35	18.43	7	GW	2369	0	40	30	0.27	5.0E-02	MH	2129	72	18	10	0.53	8.0E-03
36	18.43	7	GW	2369	0	40	30	0.27	5.0E-02	SC	2150	11	31	20	0.15	1.0E-03
37	18.43	7	ML	2219	22	27	15	0.42	8.0E-03	CH	2089	103	19	32	0.39	4.2E-04
38	18.43	7	ML	2219	22	27	15	0.42	8.0E-03	GM	2420	5	40	35	0.17	4.0E-02
39	18.43	7	ML	2219	22	27	15	0.42	8.0E-03	MH	2129	72	18	10	0.53	8.0E-03
40	18.43	7	ML	2219	22	27	15	0.42	8.0E-03	SC	2150	11	31	20	0.15	1.0E-03
41	18.43	12	CH	1889	11	19	7	0.39	4.2E-04	CH	2089	103	19	32	0.39	4.2E-04
42	18.43	12	CH	1889	11	19	7	0.39	4.2E-04	GM	2420	5	40	35	0.17	4.0E-02
43	18.43	12	CH	1889	11	19	7	0.39	4.2E-04	MH	2129	72	18	10	0.53	8.0E-03
44	18.43	12	CH	1889	11	19	7	0.39	4.2E-04	SC	2150	11	31	20	0.15	1.0E-03
45	18.43	12	GM	2320	0	34	20	0.17	4.0E-02	CH	2089	103	19	32	0.39	4.2E-04
46	18.43	12	GM	2320	0	34	20	0.17	4.0E-02	GM	2420	5	40	35	0.17	4.0E-02
47	18.43	12	GM	2320	0	34	20	0.17	4.0E-02	MH	2129	72	18	10	0.53	8.0E-03
48	18.43	12	GM	2320	0	34	20	0.17	4.0E-02	SC	2150	11	31	20	0.15	1.0E-03
49	18.43	12	MH	1929	50	18	2	0.53	8.0E-03	CH	2089	103	19	32	0.39	4.2E-04
50	18.43	12	MH	1929	50	18	2	0.53	8.0E-03	GM	2420	5	40	35	0.17	4.0E-02
51	18.43	12	MH	1929	50	18	2	0.53	8.0E-03	MH	2129	72	18	10	0.53	8.0E-03
52	18.43	12	MH	1929	50	18	2	0.53	8.0E-03	SC	2150	11	31	20	0.15	1.0E-03
53	18.43	12	GW	2369	0	40	30	0.27	5.0E-02	CH	2089	103	19	32	0.39	4.2E-04
54	18.43	12	GW	2369	0	40	30	0.27	5.0E-02	GM	2420	5	40	35	0.17	4.0E-02
55	18.43	12	GW	2369	0	40	30	0.27	5.0E-02	MH	2129	72	18	10	0.53	8.0E-03
56	18.43	12	GW	2369	0	40	30	0.27	5.0E-02	SC	2150	11	31	20	0.15	1.0E-03
57	18.43	12	ML	2219	22	27	15	0.42	8.0E-03	CH	2089	103	19	32	0.39	4.2E-04
58	18.43	12	ML	2219	22	27	15	0.42	8.0E-03	GM	2420	5	40	35	0.17	4.0E-02
59	18.43	12	ML	2219	22	27	15	0.42	8.0E-03	MH	2129	72	18	10	0.53	8.0E-03
60	18.43	12	ML	2219	22	27	15	0.42	8.0E-03	SC	2150	11	31	20	0.15	1.0E-03
61	18.43	15	CH	1889	11	19	7	0.39	4.2E-04	CH	2089	103	19	32	0.39	4.2E-04
62	18.43	15	CH	1889	11	19	7	0.39	4.2E-04	GM	2420	5	40	35	0.17	4.0E-02
63	18.43	15	CH	1889	11	19	7	0.39	4.2E-04	MH	2129	72	18	10	0.53	8.0E-03
64	18.43	15	CH	1889	11	19	7	0.39	4.2E-04	SC	2150	11	31	20	0.15	1.0E-03
65	18.43	15	GM	2320	0	34	20	0.17	4.0E-02	CH	2089	103	19	32	0.39	4.2E-04
66	18.43	15	GM	2320	0	34	20	0.17	4.0E-02	GM	2420	5	40	35	0.17	4.0E-02
67	18.43	15	GM	2320	0	34	20	0.17	4.0E-02	MH	2129	72	18	10	0.53	8.0E-03
68	18.43	15	GM	2320	0	34	20	0.17	4.0E-02	SC	2150	11	31	20	0.15	1.0E-03
69	18.43	15	MH	1929	50	18	2	0.53	8.0E-03	CH	2089	103	19	32	0.39	4.2E-04

70	18.43	15	MH	1929	50	18	2	0.53	8.0E-03	GM	2420	5	40	35	0.17	4.0E-02
71	18.43	15	MH	1929	50	18	2	0.53	8.0E-03	MH	2129	72	18	10	0.53	8.0E-03
72	18.43	15	MH	1929	50	18	2	0.53	8.0E-03	SC	2150	11	31	20	0.15	1.0E-03
73	18.43	15	GW	2369	0	40	30	0.27	5.0E-02	CH	2089	103	19	32	0.39	4.2E-04
74	18.43	15	GW	2369	0	40	30	0.27	5.0E-02	GM	2420	5	40	35	0.17	4.0E-02
75	18.43	15	GW	2369	0	40	30	0.27	5.0E-02	MH	2129	72	18	10	0.53	8.0E-03
76	18.43	15	GW	2369	0	40	30	0.27	5.0E-02	SC	2150	11	31	20	0.15	1.0E-03
77	18.43	15	ML	2219	22	27	15	0.42	8.0E-03	CH	2089	103	19	32	0.39	4.2E-04
78	18.43	15	ML	2219	22	27	15	0.42	8.0E-03	GM	2420	5	40	35	0.17	4.0E-02
79	18.43	15	ML	2219	22	27	15	0.42	8.0E-03	MH	2129	72	18	10	0.53	8.0E-03
80	18.43	15	ML	2219	22	27	15	0.42	8.0E-03	SC	2150	11	31	20	0.15	1.0E-03
81	26.57	3	CH	1889	11	19	7	0.39	4.2E-04	CH	2089	103	19	32	0.39	4.2E-04
82	26.57	3	CH	1889	11	19	7	0.39	4.2E-04	GM	2420	5	40	35	0.17	4.0E-02
83	26.57	3	CH	1889	11	19	7	0.39	4.2E-04	MH	2129	72	18	10	0.53	8.0E-03
84	26.57	3	CH	1889	11	19	7	0.39	4.2E-04	SC	2150	11	31	20	0.15	1.0E-03
85	26.57	3	GM	2320	0	34	20	0.17	4.0E-02	CH	2089	103	19	32	0.39	4.2E-04
86	26.57	3	GM	2320	0	34	20	0.17	4.0E-02	GM	2420	5	40	35	0.17	4.0E-02
87	26.57	3	GM	2320	0	34	20	0.17	4.0E-02	MH	2129	72	18	10	0.53	8.0E-03
88	26.57	3	GM	2320	0	34	20	0.17	4.0E-02	SC	2150	11	31	20	0.15	1.0E-03
89	26.57	3	MH	1929	50	18	2	0.53	8.0E-03	CH	2089	103	19	32	0.39	4.2E-04
90	26.57	3	MH	1929	50	18	2	0.53	8.0E-03	GM	2420	5	40	35	0.17	4.0E-02
91	26.57	3	MH	1929	50	18	2	0.53	8.0E-03	MH	2129	72	18	10	0.53	8.0E-03
92	26.57	3	MH	1929	50	18	2	0.53	8.0E-03	SC	2150	11	31	20	0.15	1.0E-03
93	26.57	3	GW	2369	0	40	30	0.27	5.0E-02	CH	2089	103	19	32	0.39	4.2E-04
94	26.57	3	GW	2369	0	40	30	0.27	5.0E-02	GM	2420	5	40	35	0.17	4.0E-02
95	26.57	3	GW	2369	0	40	30	0.27	5.0E-02	MH	2129	72	18	10	0.53	8.0E-03
96	26.57	3	GW	2369	0	40	30	0.27	5.0E-02	SC	2150	11	31	20	0.15	1.0E-03
97	26.57	3	ML	2219	22	27	15	0.42	8.0E-03	CH	2089	103	19	32	0.39	4.2E-04
98	26.57	3	ML	2219	22	27	15	0.42	8.0E-03	GM	2420	5	40	35	0.17	4.0E-02
99	26.57	3	ML	2219	22	27	15	0.42	8.0E-03	MH	2129	72	18	10	0.53	8.0E-03
100	26.57	3	ML	2219	22	27	15	0.42	8.0E-03	SC	2150	11	31	20	0.15	1.0E-03
101	26.57	7	CH	1889	11	19	7	0.39	4.2E-04	CH	2089	103	19	32	0.39	4.2E-04
102	26.57	7	CH	1889	11	19	7	0.39	4.2E-04	GM	2420	5	40	35	0.17	4.0E-02
103	26.57	7	CH	1889	11	19	7	0.39	4.2E-04	MH	2129	72	18	10	0.53	8.0E-03
104	26.57	7	CH	1889	11	19	7	0.39	4.2E-04	SC	2150	11	31	20	0.15	1.0E-03
105	26.57	7	GM	2320	0	34	20	0.17	4.0E-02	CH	2089	103	19	32	0.39	4.2E-04
106	26.57	7	GM	2320	0	34	20	0.17	4.0E-02	GM	2420	5	40	35	0.17	4.0E-02

107	26.57	7	GM	2320	0	34	20	0.17	4.0E-02	MH	2129	72	18	10	0.53	8.0E-03
108	26.57	7	GM	2320	0	34	20	0.17	4.0E-02	SC	2150	11	31	20	0.15	1.0E-03
109	26.57	7	MH	1929	50	18	2	0.53	8.0E-03	CH	2089	103	19	32	0.39	4.2E-04
110	26.57	7	MH	1929	50	18	2	0.53	8.0E-03	GM	2420	5	40	35	0.17	4.0E-02
111	26.57	7	MH	1929	50	18	2	0.53	8.0E-03	MH	2129	72	18	10	0.53	8.0E-03
112	26.57	7	MH	1929	50	18	2	0.53	8.0E-03	SC	2150	11	31	20	0.15	1.0E-03
113	26.57	7	GW	2369	0	40	30	0.27	5.0E-02	CH	2089	103	19	32	0.39	4.2E-04
114	26.57	7	GW	2369	0	40	30	0.27	5.0E-02	GM	2420	5	40	35	0.17	4.0E-02
115	26.57	7	GW	2369	0	40	30	0.27	5.0E-02	MH	2129	72	18	10	0.53	8.0E-03
116	26.57	7	GW	2369	0	40	30	0.27	5.0E-02	SC	2150	11	31	20	0.15	1.0E-03
117	26.57	7	ML	2219	22	27	15	0.42	8.0E-03	CH	2089	103	19	32	0.39	4.2E-04
118	26.57	7	ML	2219	22	27	15	0.42	8.0E-03	GM	2420	5	40	35	0.17	4.0E-02
119	26.57	7	ML	2219	22	27	15	0.42	8.0E-03	MH	2129	72	18	10	0.53	8.0E-03
120	26.57	7	ML	2219	22	27	15	0.42	8.0E-03	SC	2150	11	31	20	0.15	1.0E-03
121	26.57	12	CH	1889	11	19	7	0.39	4.2E-04	CH	2089	103	19	32	0.39	4.2E-04
122	26.57	12	CH	1889	11	19	7	0.39	4.2E-04	GM	2420	5	40	35	0.17	4.0E-02
123	26.57	12	CH	1889	11	19	7	0.39	4.2E-04	MH	2129	72	18	10	0.53	8.0E-03
124	26.57	12	CH	1889	11	19	7	0.39	4.2E-04	SC	2150	11	31	20	0.15	1.0E-03
125	26.57	12	GM	2320	0	34	20	0.17	4.0E-02	CH	2089	103	19	32	0.39	4.2E-04
126	26.57	12	GM	2320	0	34	20	0.17	4.0E-02	GM	2420	5	40	35	0.17	4.0E-02
127	26.57	12	GM	2320	0	34	20	0.17	4.0E-02	MH	2129	72	18	10	0.53	8.0E-03
128	26.57	12	GM	2320	0	34	20	0.17	4.0E-02	SC	2150	11	31	20	0.15	1.0E-03
129	26.57	12	MH	1929	50	18	2	0.53	8.0E-03	CH	2089	103	19	32	0.39	4.2E-04
130	26.57	12	MH	1929	50	18	2	0.53	8.0E-03	GM	2420	5	40	35	0.17	4.0E-02
131	26.57	12	MH	1929	50	18	2	0.53	8.0E-03	MH	2129	72	18	10	0.53	8.0E-03
132	26.57	12	MH	1929	50	18	2	0.53	8.0E-03	SC	2150	11	31	20	0.15	1.0E-03
133	26.57	12	GW	2369	0	40	30	0.27	5.0E-02	CH	2089	103	19	32	0.39	4.2E-04
134	26.57	12	GW	2369	0	40	30	0.27	5.0E-02	GM	2420	5	40	35	0.17	4.0E-02
135	26.57	12	GW	2369	0	40	30	0.27	5.0E-02	MH	2129	72	18	10	0.53	8.0E-03
136	26.57	12	GW	2369	0	40	30	0.27	5.0E-02	SC	2150	11	31	20	0.15	1.0E-03
137	26.57	12	ML	2219	22	27	15	0.42	8.0E-03	CH	2089	103	19	32	0.39	4.2E-04
138	26.57	12	ML	2219	22	27	15	0.42	8.0E-03	GM	2420	5	40	35	0.17	4.0E-02
139	26.57	12	ML	2219	22	27	15	0.42	8.0E-03	MH	2129	72	18	10	0.53	8.0E-03
140	26.57	12	ML	2219	22	27	15	0.42	8.0E-03	SC	2150	11	31	20	0.15	1.0E-03
141	26.57	15	CH	1889	11	19	7	0.39	4.2E-04	CH	2089	103	19	32	0.39	4.2E-04
142	26.57	15	CH	1889	11	19	7	0.39	4.2E-04	GM	2420	5	40	35	0.17	4.0E-02
143	26.57	15	CH	1889	11	19	7	0.39	4.2E-04	MH	2129	72	18	10	0.53	8.0E-03

144	26.57	15	CH	1889	11	19	7	0.39	4.2E-04	SC	2150	11	31	20	0.15	1.0E-03
145	26.57	15	GM	2320	0	34	20	0.17	4.0E-02	CH	2089	103	19	32	0.39	4.2E-04
146	26.57	15	GM	2320	0	34	20	0.17	4.0E-02	GM	2420	5	40	35	0.17	4.0E-02
147	26.57	15	GM	2320	0	34	20	0.17	4.0E-02	MH	2129	72	18	10	0.53	8.0E-03
148	26.57	15	GM	2320	0	34	20	0.17	4.0E-02	SC	2150	11	31	20	0.15	1.0E-03
149	26.57	15	MH	1929	50	18	2	0.53	8.0E-03	CH	2089	103	19	32	0.39	4.2E-04
150	26.57	15	MH	1929	50	18	2	0.53	8.0E-03	GM	2420	5	40	35	0.17	4.0E-02
151	26.57	15	MH	1929	50	18	2	0.53	8.0E-03	MH	2129	72	18	10	0.53	8.0E-03
152	26.57	15	MH	1929	50	18	2	0.53	8.0E-03	SC	2150	11	31	20	0.15	1.0E-03
153	26.57	15	GW	2369	0	40	30	0.27	5.0E-02	CH	2089	103	19	32	0.39	4.2E-04
154	26.57	15	GW	2369	0	40	30	0.27	5.0E-02	GM	2420	5	40	35	0.17	4.0E-02
155	26.57	15	GW	2369	0	40	30	0.27	5.0E-02	MH	2129	72	18	10	0.53	8.0E-03
156	26.57	15	GW	2369	0	40	30	0.27	5.0E-02	SC	2150	11	31	20	0.15	1.0E-03
157	26.57	15	ML	2219	22	27	15	0.42	8.0E-03	CH	2089	103	19	32	0.39	4.2E-04
158	26.57	15	ML	2219	22	27	15	0.42	8.0E-03	GM	2420	5	40	35	0.17	4.0E-02
159	26.57	15	ML	2219	22	27	15	0.42	8.0E-03	MH	2129	72	18	10	0.53	8.0E-03
160	26.57	15	ML	2219	22	27	15	0.42	8.0E-03	SC	2150	11	31	20	0.15	1.0E-03
161	39.81	3	CH	1889	11	19	7	0.39	4.2E-04	CH	2089	103	19	32	0.39	4.2E-04
162	39.81	3	CH	1889	11	19	7	0.39	4.2E-04	GM	2420	5	40	35	0.17	4.0E-02
163	39.81	3	CH	1889	11	19	7	0.39	4.2E-04	MH	2129	72	18	10	0.53	8.0E-03
164	39.81	3	CH	1889	11	19	7	0.39	4.2E-04	SC	2150	11	31	20	0.15	1.0E-03
165	39.81	3	GM	2320	0	34	20	0.17	4.0E-02	CH	2089	103	19	32	0.39	4.2E-04
166	39.81	3	GM	2320	0	34	20	0.17	4.0E-02	GM	2420	5	40	35	0.17	4.0E-02
167	39.81	3	GM	2320	0	34	20	0.17	4.0E-02	MH	2129	72	18	10	0.53	8.0E-03
168	39.81	3	GM	2320	0	34	20	0.17	4.0E-02	SC	2150	11	31	20	0.15	1.0E-03
169	39.81	3	MH	1929	50	18	2	0.53	8.0E-03	CH	2089	103	19	32	0.39	4.2E-04
170	39.81	3	MH	1929	50	18	2	0.53	8.0E-03	GM	2420	5	40	35	0.17	4.0E-02
171	39.81	3	MH	1929	50	18	2	0.53	8.0E-03	MH	2129	72	18	10	0.53	8.0E-03
172	39.81	3	MH	1929	50	18	2	0.53	8.0E-03	SC	2150	11	31	20	0.15	1.0E-03
173	39.81	3	GW	2369	0	40	30	0.27	5.0E-02	CH	2089	103	19	32	0.39	4.2E-04
174	39.81	3	GW	2369	0	40	30	0.27	5.0E-02	GM	2420	5	40	35	0.17	4.0E-02
175	39.81	3	GW	2369	0	40	30	0.27	5.0E-02	MH	2129	72	18	10	0.53	8.0E-03
176	39.81	3	GW	2369	0	40	30	0.27	5.0E-02	SC	2150	11	31	20	0.15	1.0E-03
177	39.81	3	ML	2219	22	27	15	0.42	8.0E-03	CH	2089	103	19	32	0.39	4.2E-04
178	39.81	3	ML	2219	22	27	15	0.42	8.0E-03	GM	2420	5	40	35	0.17	4.0E-02
179	39.81	3	ML	2219	22	27	15	0.42	8.0E-03	MH	2129	72	18	10	0.53	8.0E-03
180	39.81	3	ML	2219	22	27	15	0.42	8.0E-03	SC	2150	11	31	20	0.15	1.0E-03

181	39.81	7	CH	1889	11	19	7	0.39	4.2E-04	CH	2089	103	19	32	0.39	4.2E-04
182	39.81	7	CH	1889	11	19	7	0.39	4.2E-04	GM	2420	5	40	35	0.17	4.0E-02
183	39.81	7	CH	1889	11	19	7	0.39	4.2E-04	MH	2129	72	18	10	0.53	8.0E-03
184	39.81	7	CH	1889	11	19	7	0.39	4.2E-04	SC	2150	11	31	20	0.15	1.0E-03
185	39.81	7	GM	2320	0	34	20	0.17	4.0E-02	CH	2089	103	19	32	0.39	4.2E-04
186	39.81	7	GM	2320	0	34	20	0.17	4.0E-02	GM	2420	5	40	35	0.17	4.0E-02
187	39.81	7	GM	2320	0	34	20	0.17	4.0E-02	MH	2129	72	18	10	0.53	8.0E-03
188	39.81	7	GM	2320	0	34	20	0.17	4.0E-02	SC	2150	11	31	20	0.15	1.0E-03
189	39.81	7	MH	1929	50	18	2	0.53	8.0E-03	CH	2089	103	19	32	0.39	4.2E-04
190	39.81	7	MH	1929	50	18	2	0.53	8.0E-03	GM	2420	5	40	35	0.17	4.0E-02
191	39.81	7	MH	1929	50	18	2	0.53	8.0E-03	MH	2129	72	18	10	0.53	8.0E-03
192	39.81	7	MH	1929	50	18	2	0.53	8.0E-03	SC	2150	11	31	20	0.15	1.0E-03
193	39.81	7	GW	2369	0	40	30	0.27	5.0E-02	CH	2089	103	19	32	0.39	4.2E-04
194	39.81	7	GW	2369	0	40	30	0.27	5.0E-02	GM	2420	5	40	35	0.17	4.0E-02
195	39.81	7	GW	2369	0	40	30	0.27	5.0E-02	MH	2129	72	18	10	0.53	8.0E-03
196	39.81	7	GW	2369	0	40	30	0.27	5.0E-02	SC	2150	11	31	20	0.15	1.0E-03
197	39.81	7	ML	2219	22	27	15	0.42	8.0E-03	CH	2089	103	19	32	0.39	4.2E-04
198	39.81	7	ML	2219	22	27	15	0.42	8.0E-03	GM	2420	5	40	35	0.17	4.0E-02
199	39.81	7	ML	2219	22	27	15	0.42	8.0E-03	MH	2129	72	18	10	0.53	8.0E-03
200	39.81	7	ML	2219	22	27	15	0.42	8.0E-03	SC	2150	11	31	20	0.15	1.0E-03
201	39.81	12	CH	1889	11	19	7	0.39	4.2E-04	CH	2089	103	19	32	0.39	4.2E-04
202	39.81	12	CH	1889	11	19	7	0.39	4.2E-04	GM	2420	5	40	35	0.17	4.0E-02
203	39.81	12	CH	1889	11	19	7	0.39	4.2E-04	MH	2129	72	18	10	0.53	8.0E-03
204	39.81	12	CH	1889	11	19	7	0.39	4.2E-04	SC	2150	11	31	20	0.15	1.0E-03
205	39.81	12	GM	2320	0	34	20	0.17	4.0E-02	CH	2089	103	19	32	0.39	4.2E-04
206	39.81	12	GM	2320	0	34	20	0.17	4.0E-02	GM	2420	5	40	35	0.17	4.0E-02
207	39.81	12	GM	2320	0	34	20	0.17	4.0E-02	MH	2129	72	18	10	0.53	8.0E-03
208	39.81	12	GM	2320	0	34	20	0.17	4.0E-02	SC	2150	11	31	20	0.15	1.0E-03
209	39.81	12	MH	1929	50	18	2	0.53	8.0E-03	CH	2089	103	19	32	0.39	4.2E-04
210	39.81	12	MH	1929	50	18	2	0.53	8.0E-03	GM	2420	5	40	35	0.17	4.0E-02
211	39.81	12	MH	1929	50	18	2	0.53	8.0E-03	MH	2129	72	18	10	0.53	8.0E-03
212	39.81	12	MH	1929	50	18	2	0.53	8.0E-03	SC	2150	11	31	20	0.15	1.0E-03
213	39.81	12	GW	2369	0	40	30	0.27	5.0E-02	CH	2089	103	19	32	0.39	4.2E-04
214	39.81	12	GW	2369	0	40	30	0.27	5.0E-02	GM	2420	5	40	35	0.17	4.0E-02
215	39.81	12	GW	2369	0	40	30	0.27	5.0E-02	MH	2129	72	18	10	0.53	8.0E-03
216	39.81	12	GW	2369	0	40	30	0.27	5.0E-02	SC	2150	11	31	20	0.15	1.0E-03
217	39.81	12	ML	2219	22	27	15	0.42	8.0E-03	CH	2089	103	19	32	0.39	4.2E-04

218	39.81	12	ML	2219	22	27	15	0.42	8.0E-03	GM	2420	5	40	35	0.17	4.0E-02
219	39.81	12	ML	2219	22	27	15	0.42	8.0E-03	MH	2129	72	18	10	0.53	8.0E-03
220	39.81	12	ML	2219	22	27	15	0.42	8.0E-03	SC	2150	11	31	20	0.15	1.0E-03
221	39.81	15	CH	1889	11	19	7	0.39	4.2E-04	CH	2089	103	19	32	0.39	4.2E-04
222	39.81	15	CH	1889	11	19	7	0.39	4.2E-04	GM	2420	5	40	35	0.17	4.0E-02
223	39.81	15	CH	1889	11	19	7	0.39	4.2E-04	MH	2129	72	18	10	0.53	8.0E-03
224	39.81	15	CH	1889	11	19	7	0.39	4.2E-04	SC	2150	11	31	20	0.15	1.0E-03
225	39.81	15	GM	2320	0	34	20	0.17	4.0E-02	CH	2089	103	19	32	0.39	4.2E-04
226	39.81	15	GM	2320	0	34	20	0.17	4.0E-02	GM	2420	5	40	35	0.17	4.0E-02
227	39.81	15	GM	2320	0	34	20	0.17	4.0E-02	MH	2129	72	18	10	0.53	8.0E-03
228	39.81	15	GM	2320	0	34	20	0.17	4.0E-02	SC	2150	11	31	20	0.15	1.0E-03
229	39.81	15	MH	1929	50	18	2	0.53	8.0E-03	CH	2089	103	19	32	0.39	4.2E-04
230	39.81	15	MH	1929	50	18	2	0.53	8.0E-03	GM	2420	5	40	35	0.17	4.0E-02
231	39.81	15	MH	1929	50	18	2	0.53	8.0E-03	MH	2129	72	18	10	0.53	8.0E-03
232	39.81	15	MH	1929	50	18	2	0.53	8.0E-03	SC	2150	11	31	20	0.15	1.0E-03
233	39.81	15	GW	2369	0	40	30	0.27	5.0E-02	CH	2089	103	19	32	0.39	4.2E-04
234	39.81	15	GW	2369	0	40	30	0.27	5.0E-02	GM	2420	5	40	35	0.17	4.0E-02
235	39.81	15	GW	2369	0	40	30	0.27	5.0E-02	MH	2129	72	18	10	0.53	8.0E-03
236	39.81	15	GW	2369	0	40	30	0.27	5.0E-02	SC	2150	11	31	20	0.15	1.0E-03
237	39.81	15	ML	2219	22	27	15	0.42	8.0E-03	CH	2089	103	19	32	0.39	4.2E-04
238	39.81	15	ML	2219	22	27	15	0.42	8.0E-03	GM	2420	5	40	35	0.17	4.0E-02
239	39.81	15	ML	2219	22	27	15	0.42	8.0E-03	MH	2129	72	18	10	0.53	8.0E-03
240	39.81	15	ML	2219	22	27	15	0.42	8.0E-03	SC	2150	11	31	20	0.15	1.0E-03

APPENDIX D

- Dam failure: Failure parameters for all the simulations

					Failure modes						
					Embankment			Foundation			
#	PD	BP	BIT	FE	GEF	EIF	EEF	GFF	FEF	FPF	FBF
1	1.108	0	0	0	0.0	0	0	0.0	0	0	0
2	1.529	54	75	0	1.0	0	1	0.0	0	0	0
3	1.209	0	0	0	0.0	0	0	0.0	0	0	0
4	1.193	0	0	0	0.6	0	0.6	0.0	0	0	0
5	1.074	0	0	0.9	0.0	0	0	1.0	1	0	0
6	1.841	17.3	16	0	1.0	1	0	1.0	0	0	1
7	1.122	0	0	1	0.0	0	0	1.0	1	0	0
8	1.106	0	0	1.2	0.0	0	0	1.0	1	0	0
9	1.086	0	0	0	0.0	0	0	0.0	0	0	0
10	1.429	100	52	0	1.0	1	0	0.0	0	0	0
11	1.049	0	0	0	0.2	0.2	0	0.0	0	0	0
12	1.077	0	0	0	0.5	0	0.5	0.0	0	0	0
13	1.226	0	0	2.5	0.0	0	0	1.0	0	1	0
14	1.036	100	50	2.5	1.0	1	0	1.0	0	1	0
15	1.310	40	250	2.5	0.0	0	0	1.0	0	1	0
16	4.179	100	30	2.5	1.0	1	0	1.0	0	1	0
17	1.105	0	0	0.3	0.2	0	0.2	0.2	0.2	0	0
18	1.421	18	32.5	0	1.0	1	0	0.0	0	0	0
19	1.028	0	0	0.2	0.0	0	0	0.3	0.3	0	0
20	1.057	0	0	0	0.5	0	0.5	0.0	0	0	0
21	1.136	0	0	0	0.0	0	0	0.0	0	0	0
22	1.75	29	70.5	0	1.0	1	0	0.0	0	0	0
23	1.276	0	0	0	0.0	0	0	0.0	0	0	0
24	1.331	0	0	0	0.5	0	0.5	0.0	0	0	0
25	1.24	0	0	0.4	0.0	0	0	1.0	1	0	0
26	1.076	0	0	0	1.0	1	0	0.0	0	0	0
27	1.116	0	0	0.2	0.0	0	0	1.0	1	0	0
28	1.254	0	0	0.4	0.0	0	0	1.0	1	0	0
29	1.254	0	0	0	0.0	0	0	0.0	0	0	0
30	2.056	48	10	0	1.0	1	0	0.0	0	0	0
31	1.081	0	0	0	0.0	0	0	0.0	0	0	0

32	1.202	0	0	0	0.5	0	0.5	0.0	0	0	0
33	1.169	0	0	2.5	0.0	0	0	1.0	0	1	0
34	2.053	100	7	2.5	1.0	1	0	1.0	0	1	0
35	1.24	0	0	2.5	0.0	0	0	1.0	0	1	0
36	1.113	0	0	2.5	0.0	0	0	1.0	0	1	0
37	1.224	0	0	0	0.0	0	0	0.3	0.3	0	0
38	1.209	0	0	0	0.7	0.5	0.7	0.0	0	0	0
39	1.173	0	0	0	0.0	0	0	0.2	0.2	0	0
40	1.24	0	0	0	0.2	0	0.2	0.0	0	0	0
41	1.16	0	0	0	0.2	0.2	0	0.2	0	0	0.2
42	3.598	42	5	0	1.0	1	0	0.0	0	0	0
43	1.416	0	0	0	0.2	0.2	0	0.5	0	0	0.5
44	1.404	0	0	0	0.5	0	0.5	0.2	0	0	0.2
45	1.01	0	0	0.4	0.0	0	0	0.5	0.5	0	0
46	1.491	5	15	0	1.0	1	0	0.0	0	0	0
47	1.179	0	0	0.5	0.0	0	0	1.0	1	0	0.3
48	1.41	0	0	0.55	0.0	0	0	1.0	1	0	0
49	1.251	0	0	0	0.0	0	0	0.2	0	0	0.2
50	3.056	36	5	0	1.0	1	0	0.0	0	0	0
51	1.437	0	0	0	0.3	0.3	0	0.5	0	0	0.5
52	1.238	0	0	0	0.5	0.5	0.3	0.0	0	0	0
53	1.432	0	0	1.8	0.0	0	0	1.0	0	1	0
54	1.766	13	5	3	1.0	1	0	1.0	0	0	1
55	1.538	0	0	2	0.0	0	0	1.0	0	1	0
56	1.752	0	0	3	0.0	0	0	1.0	0	1	0
57	1.227	0	0	0	0.0	0	0	0.0	0	0	0
58	2.428	31	81.5	0	1.0	1	0	0.0	0	0	0
59	1.216	0	0	0	0.1	0.1	0	0.1	0	0	0.1
60	1.237	0	0	0	0.3	0	0.3	0.0	0	0	0
61	1.105	0	0	0	0.2	0.2	0	0.0	0	0	0
62	1.66	4	20	0	1.0	1	0	0.0	0	0	0
63	1.65	0	0	0	0.3	0.3	0	0.4	0	0	0.4
64	1.299	0	0	0	0.3	0	0.3	0.2	0	0	0.2
65	1.014	0	0	0	0.0	0	0	0.1	0	0	0.1
66	2.143	5	10	0	1.0	1	0.8	0.0	0	0	0
67	1.446	0	0	0	0.2	0.1	0.1	0.3	0	0	0.3
68	1.13	0	0	0	0.1	0	0.1	0.0	0	0	0

69	1.134	0	0	0	0.1	0.1	0	0.2	0	0	0.2
70	3.963	26	5	0	1.0	1	0	0.0	0	0	0
71	1.668	0	0	0	0.1	0.1	0	0.3	0	0	0.3
72	1.204	0	0	0	0.4	0.4	0.2	0.0	0	0	0
73	1.089	0	0	3	0.0	0	0	1.0	0	1	0
74	2.041	0	0	1	0.2	0.2	0.7	1.0	0	1	0
75	1.485	0	0	1	0.7	0	0.7	1.0	0	1	0
76	0.939	0	0	0.5	0.0	0	0	0.8	0	0.8	0
77	1.013	0	0	0	0.2	0.2	0	0.1	0	0	0.1
78	2.119	2	5	0	1	1	0	0	0	0	0
79	1.402	0	0	0	0.1	0.1	0	0.1	0	0	0.1
80	0.928	0	0	0	0.1	0	0.1	0.0	0	0	0
81	1.112	0	0	0	0.0	0	0	0.0	0	0	0
82	1.503	61	42	0	1.0	1	0	0.0	0	0	0
83	1.147	0	0	0	0.0	0	0	0.0	0	0	0
84	1.145	2	138.5	0	1.0	0.2	1	0.0	0	0	0
85	1.245	0	0	1	0.0	0	0	1.0	1	0	0
86	1.345	12	12	0	1.0	1	0	0.0	0	0	0
87	1.17	0	0	0	0.0	0	0	0.4	0	0	0.4
88	1.086	0	0	0	0.5	0	0.5	0.5	0.2	0	0.5
89	1.067	0	0	0	0.0	0	0	0.0	0	0	0
90	1.272	40	103.5	0	1.0	1	0	0.0	0	0	0
91	1.015	0	0	0	0.0	0	0	0.0	0	0	0
92	1.106	0	0	0	0.6	0.6	0.6	0.0	0	0	0
93	1.298	0	0	3	0.0	0	0	1.0	0	1	0
94	1.323	100	10	3	1.0	1	0	1.0	0	1	0
95	1.05	100	60	3	1.0	1	0	1.0	0	1	0
96	3.377	100	120	3	1.0	1	0	1.0	0	1	0
97	1.058	0	0	0	0.0	0	0	0.1	0.1	0	0
98	1.193	19	50	0	1.0	1	1	0.0	0	0	0
99	1.111	0	0	0	0.0	0	0	0.1	0.1	0	0
100	1.094	0	0	0	0.6	0	0.6	0.0	0	0	0
101	0.975	0	0	0	0	0	0	0	0	0	0
102	3.135	55	7	0	1.0	1	0	0.0	0	0	0
103	1.215	0	0	0	0.2	0.2	0	0.6	0	0	0.6
104	1.281	0	0	0	0.7	0.5	0.7	0.0	0	0	0
105	1.213	0	0	0	0.0	0	0	0.3	0	0	0.3

106	1.981	13	13.5	0	1.0	1	0	0.0	0	0	0
107	1.192	0	0	0	0.0	0	0	0.2	0	0	0.2
108	1.552	0	0	0	0.0	0	0	0.0	0	0	0
109	1.202	0	0	0	0.0	0	0	0.0	0	0	0
110	2.438	36	6	0	1.0	1	0	0.0	0	0	0
111	1.208	0	0	0	0.1	0.1	0	0.1	0	0	0.1
112	1.214	0	0	0	0.6	0.4	0.6	0.0	0	0	0
113	1.48	0	0	3	0.0	0	0	1.0	0	1	0
114	2.329	27	5	3	1.0	1	0	1.0	0	1	0
115	1.379	0	0	3	0.0	0	0	1.0	0	1	0
116	4.481	0	0	0	0.7	0.7	0	1.0	0	1	0
117	1.234	0	0	0	0.0	0	0	0.3	0.3	0	0
118	1.302	7	5	0	1.0	1	0	0.0	0	0	0
119	1.172	0	0	0	0.0	0	0	0.1	0.1	0	0.1
120	1.032	0	0	0	0.5	0	0.5	0.0	0	0	0
121	1.414	0	0	0	0.0	0	0	0.5	0	0	0.5
122	7.01	49	5	0	1.0	1	0	0.0	0	0	0
123	1.594	0	0	0	0.5	0.5	0	0.6	0	0	0.6
124	1.772	2	195	0	1.0	1	0.3	1.0	0	0	1
125	1.065	0	0	0	0.0	0	0.1	0.3	0	0	0.3
126	1.697	10	10	0	1.0	1	0	0.0	0	0	0
127	1.422	0	0	0	0.0	0	0	0.1	0	0	0.1
128	1.382	0	0	0	0.3	0.1	0.3	0.0	0	0	0.5
129	1.251	0	0	0	0.0	0	0	0.3	0	0	0.3
130	7.487	39	5	0	1.0	1	0	0.0	0	0	0
131	1.689	0	0	0	0.2	0.2	0	0.5	0	0	0.5
132	1.311	0	0	0	0.5	0.5	0.5	0.0	0	0	0
133	1.454	0	0	3	0.0	0	0	1.0	0	1	0
134	3.726	23	5	0	1.0	1	0	1.0	0	1	0
135	1.8	0	0	0.5	0.5	0	0.5	1.0	0	1	0
136	2.833	0	0	0	0.6	0.6	0	1.0	0	1	0
137	1.345	0	0	0	0.0	0	0	0.1	0	0	0.1
138	2.059	15	5	0	1.0	1	0	0.0	0	0	0
139	1.411	0	0	0	0.1	0.1	0	0.1	0	0	0.1
140	1.431	0	0	0	0.5	0.2	0.5	0.0	0	0	0
141	1.457	0	0	0	0.0	0	0	0.5	0	0	0.5
142	14.146	40	5	0	1.0	1	0	1.0	0	0	1

143	2.353	7	5	0	0.7	0.7	0	1.0	0	0	1
144	1.953	10	81	0	1.0	1	0	1.0	0	0	1
145	1.297	0	0	0	0.4	0.4	0	0.2	0	0	0.2
146	2.461	13	5	0	1.0	1	0	0.0	0	0	0
147	1.71	0	0	0	0.3	0.3	0	0.3	0	0	0.3
148	1.254	0	0	0	0.2	0.2	0.2	0.0	0	0	0
149	1.282	0	0	0	0.1	0.1	0	0.3	0	0	0.3
150	11.147	40	5	0	1.0	1	0	0.0	0	0	0
151	2.078	0	0	0	0.2	0.2	0	0.3	0	0	0.3
152	1.28	0	0	0	0.8	0.7	0.8	0.2	0	0	0.2
153	1.397	0	0	1.5	0.0	0	0	1.0	0	1	0
154	3.049	13	5	0	1.0	1	0	1.0	0	1	0
155	1.814	0	0	0	0.0	0	0	1.0	0	1	0
156	1.136	0	0	0	0.3	0	0.3	0.5	0	0.5	0
157	1.205	0	0	0	0.0	0	0	0.2	0	0	0.2
158	3.636	21	5	0	1.0	1	0	0.0	0	0	0
159	1.755	0	0	0	0.2	0.2	0	0.3	0	0	0.3
160	1.261	0	0	0	0.3	0.2	0.3	0.1	0	0	0.1
161	1.097	0	0	0	0.1	0.1	0	0.4	0	0	0.4
162	1.555	79	2	0	1.0	1	0	0.0	0	0	0
163	1.144	0	0	0	0.0	0	0	0.2	0	0	0.2
164	1.268	14	32.5	0	1.0	1	1	0.0	0	0	0
165	1.235	0	0	0.7	0.0	0	0	0.5	0.5	0	0.5
166	1.401	61	10	0	1.0	1	0	1.0	0	0	1
167	1.128	0	0	0	0.0	0	0	0.3	0	0	0.3
168	1.217	0	0	0.3	1.0	1	1	0.0	0	0	0
169	1.07	0	0	0	0.1	0.1	0	0.1	0	0	0.1
170	1.281	67	10	0	1.0	1	0	0.0	0	0	0
171	1.055	0	0	0	0.0	0	0	0.0	0	0	0.1
172	1.113	9	41	0	1.0	1	0.8	0.0	0	0	0
173	3.574	100	10	3	0.0	0	0	1.0	0	1	0
174	1.441	100	5	3	1.0	1	0	1.0	0	1	0
175	1.083	100	10	3	0.0	0	0	1.0	0	1	0
176	4.649	100	7	3	0.5	0.5	0	1.0	0	1	0
177	1.158	0	0	0	0.0	0	0	0.2	0.2	0	0
178	1.362	56	5	0	1.0	1	0	0.0	0	0	0
179	1.072	0	0	0	0.0	0	0	0.2	0.2	0	0

180	1.098	0	0	0	0.7	0	0.7	0.0	0	0	0
181	1.354	0	0	0	0.0	0	0	1.0	0	0	1
182	6.575	77	3	0	1.0	1	0	0.0	0	0	0
183	1.25	0	0	0	0.2	0.2	0	0.8	0	0	0.8
184	1.543	18	5	0	1.0	1	0.3	0.5	0	0	0.5
185	1.179	0	0	0	0.0	0	0	0.3	0	0	0.3
186	1.233	0	0	0	1.0	1	0	0.5	0	0	0.5
187	1.155	0	0	0	0.0	0	0	0.3	0	0	0.3
188	1.254	5	60	0	1.0	1	0.7	0.0	0	0	0.3
189	1.187	0	0	0	0.0	0	0	0.2	0	0	0.2
190	6.51	68	3	0	1.0	1	0	0.0	0	0	0
191	1.367	0	0	0	0.0	0	0	0.1	0	0	0.1
192	1.403	15	33	0	1.0	1	0	0.0	0	0	0
193	1.672	100	10	3	0.0	0	0	1.0	0	1	0
194	4.378	100	5	3	1.0	1	0	1.0	0	1	1
195	1.549	100	0	3	0.0	0	0	1.0	0	1	0
196	4.429	100	20	3	1.0	1	0	1.0	0	1	1
197	1.143	0	0	0	0.1	0	0.1	0.2	0.1	0	0.2
198	4.082	57	5	0	1.0	1	0	0.0	0	0	0
199	1.179	0	0	0	0.0	0	0	0.2	0	0	0.2
200	1.207	5	80	0	1.0	1	0.7	0.0	0	0	0
201	1.911	3	120	0	0.0	0	0	1.0	0	0	1
202	16.179	71	3	0	1.0	1	0	0.0	0	0	0
203	2.292	9	3	0	1.0	1	0	1.0	0	0	1
204	2.817	26	10	0	1.0	1	0	1.0	0	0	1
205	1.315	0	0	0	0.1	0.1	0	0.5	0	0	0.5
206	11.431	57	3	1	1.0	1	0	1.0	0	0	1
207	1.788	0	0	0	0.2	0.2	0	0.4	0	0	0.4
208	2.275	11	40	1.3	1.0	1	0.1	1.0	0	0	1
209	1.27	0	0	0	0.4	0.4	0	0.6	0	0	0.6
210	16.317	64	3	0	1.0	1	0	0.0	0	0	0
211	2.139	0	0	0	0.5	0.5	0	0.5	0	0	0.5
212	2.155	28	5	0	1.0	1	0	0.0	0	0	0
213	1.523	0	0	3	0.0	0	0	1.0	0	1	0
214	12.652	55	3	1	1.0	1	0	1.0	0	1	0
215	1.978	0	0	3	0.0	0	0	1.0	0	1	0
216	1.937	9	10	1	1.0	1	0	1.0	0	1	0

217	1.251	0	0	0	0.1	0.1	0.1	0.3	0	0	0.3
218	11.676	58	3	0	1.0	1	0	0.0	0	0	0
219	1.797	0	0	0	0.2	0.2	0	0.4	0	0	0.4
220	1.734	14	47.5	0	1.0	1	0	0.0	0	0	0
221	1.651	0	0	3	0.7	0.7	0	1.0	0	0	1
222	21.976	68	5	0	1.0	1	0	0.0	0	0	0
223	2.736	18	5	3	1.0	1	0	0.0	0	0	1
224	2.85	27	5	3	1.0	1	0	1.0	0	0	1
225	1.206	0	0	0	0.0	0	0	0.6	0	0	0.6
226	16.575	55	5	0	1.0	1	0	1.0	0	0	1
227	2.196	0	0	0	0.6	0.6	0	0.7	0	0	0.7
228	3.12	27	40.5	0	1.0	1	0	1.0	0	0	1
229	1.246	0	0	0	0.0	0	0	0.5	0	0	0.5
230	21.392	62	5	0	1.0	1	0	0.0	0	0	0
231	2.612	0	0	0	0.8	0.8	0	0.5	0	0	0.5
232	3.576	32	5	0	1.0	1	0	0.0	0	0	0
233	1.242	0	0	0	0.0	0	0	1.0	0	0.7	0
234	17.21	51	5	0	1.0	1	0	0.3	0	0	0.3
235	16.5	0	0	0	0.2	0.2	0	0.8	0	0.8	0
236	2.556	24	80	1	1.0	1	0	1.0	0	0	1
237	1.151	0	0	0	0.3	0.3	0	0.5	0	0	0.5
238	16.937	57	5	0	1.0	1	0	0.0	0	0	0
239	2.259	0	0	0	0.5	0.5	0	0.6	0	0	0.6
240	2.336	23	25	0	1.0	1	0	0.0	0	0	0

APPENDIX E

- Correlation matrices between the inputs and the outputs
  - Correlation matrix between the inputs

	Geom.		Foundation soil properties						Embankment soil properties					
	α	**H**	**ρ**	**C**	**Φ**	**E**	**n**	**d15**	**ρ**	**C**	**Φ**	**E**	**n**	**d15**
α	1.00													
H	0.00	1.00												
ρ	0.00	0.00	1.00											
C	0.00	0.00	-0.65	1.00										
Φ	0.00	0.00	0.96	-0.74	1.00									
E	0.00	0.00	0.93	-0.79	0.99	1.00								
n	0.00	0.00	-0.75	0.91	-0.80	-0.78	1.00							
d15	0.00	0.00	0.86	-0.64	0.94	0.89	-0.80	1.00						
ρ	0.00	0.00	0.00	0.00	0.00	0.00	0.00	0.00	1.00					
C	0.00	0.00	0.00	0.00	0.00	0.00	0.00	0.00	-0.71	1.00				
Φ	0.00	0.00	0.00	0.00	0.00	0.00	0.00	0.00	0.88	-0.91	1.00			
E	0.00	0.00	0.00	0.00	0.00	0.00	0.00	0.00	0.53	-0.13	0.52	1.00		
n	0.00	0.00	0.00	0.00	0.00	0.00	0.00	0.00	-0.57	0.83	-0.88	-0.53	1.00	
d15	0.00	0.00	0.00	0.00	0.00	0.00	0.00	0.00	0.98	-0.57	0.76	0.49	-0.39	1.00

- Correlation matrix between the inputs and outputs

	Q_{max}	BP	BIT	FE	GEF	EIF	EEF	GFF	FEF	FPF	FBF
α	0.33	0.30	0.34	0.03	0.22	0.28	-0.08	0.10	-0.20	-0.02	0.35
H	0.26	-0.18	0.10	-0.14	0.05	0.10	-0.15	0.08	-0.18	-0.05	0.27
ρ	-0.06	0.05	-0.11	0.43	-0.12	-0.10	-0.09	0.47	0.20	0.54	-0.12
C	0.02	-0.07	0.01	-0.40	0.04	0.04	0.06	-0.54	-0.18	-0.43	-0.14
Φ	-0.03	0.13	-0.07	0.57	-0.10	-0.07	-0.11	0.61	0.16	0.70	-0.09
E	-0.02	0.15	-0.05	0.60	-0.09	-0.07	-0.10	0.63	0.11	0.74	-0.09
n	0.04	-0.02	0.06	-0.32	0.07	0.05	0.08	-0.50	-0.30	-0.33	-0.13
d_{15}	-0.02	0.14	-0.06	0.57	-0.09	-0.04	-0.13	0.64	0.17	0.69	-0.06
ρ	0.42	0.52	0.64	-0.06	0.73	0.73	-0.01	-0.17	-0.16	-0.03	-0.10
C	-0.28	-0.39	-0.44	0.07	-0.78	-0.69	-0.33	0.17	0.13	0.03	0.08
Φ	0.36	0.48	0.56	-0.06	0.81	0.75	0.22	-0.19	-0.15	-0.03	-0.11
E	0.22	0.29	0.36	0.00	0.31	0.34	-0.08	-0.10	-0.06	-0.02	-0.10
n	-0.22	-0.33	-0.37	0.05	-0.68	-0.59	-0.35	0.16	0.10	0.03	0.11
d_{15}	0.42	0.49	0.62	-0.06	0.64	0.67	-0.11	-0.15	-0.15	-0.02	-0.08

- Correlation matrix between the outputs

	Q_{max}	BP	BIT	FE	GEF	EIF	EEF	GFF	FEF	FPF	FBF
Q_{max}	1.00										
BP	0.44	1.00									
BIT	0.59	0.61	1.00								
FE	-0.05	0.37	0.06	1.00							
GEF	0.37	0.51	0.60	-0.04	1.00						
EIF	0.39	0.54	0.64	0.00	0.94	1.00					
EEF	-0.15	-0.16	-0.19	-0.16	0.22	0.00	1.00				
GFF	0.01	0.14	-0.01	0.64	-0.11	-0.05	-0.25	1.00			
FEF	-0.09	-0.14	-0.13	0.02	-0.26	-0.24	-0.10	0.26	1.00		
FPF	0.00	0.30	0.02	0.76	-0.06	-0.04	-0.11	0.67	-0.12	1.00	
FBF	0.07	-0.01	0.08	0.02	0.14	0.18	-0.16	0.39	-0.11	-0.21	1.00

VITA

Khalil M. Qatu was born October 18, 1988 in Tulkarm, Palestine. Khalil received his Bachelor of Science in Civil Engineering in 2010. After obtaining his Bachelor's degree at Jordan University of Science and Technology (JUST), he shortly began his job as a field engineer at Al-Qatu for construction before pursuing his masters in Industrial Management in 2013. Khalil received his master's degree in 2015 from Central Michigan University. Afterwards, he started his Ph.D. study at the University of Mississippi in 2015.